Real-time Structural Health Monitoring of Nonlinear Hysteretic Structures

Mostafa Nayyerloo
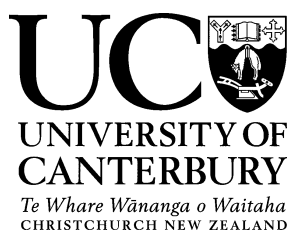
A thesis presented for partial fulfilment of the requirements for the degree of

Doctor of Philosophy

in

Mechanical Engineering

at the

UC

UNIVERSITY OF CANTERBURY
Te Whare Wānanga o Waitaha
CHRISTCHURCH NEW ZEALAND

University of Canterbury

Christchurch, New Zealand

September 2011

This thesis is dedicated in memory of

those who lost their lives in the February 2011 earthquake in

Christchurch, New Zealand.

ABSTRACT

The great social and economic impact of earthquakes has made necessary the development of novel solutions for increasing the level of structural safety and assessment. Outdated design codes used to design many existing structures built years ago, increased demand loads, nonlinearities usually neglected or simplified in current design procedures, aging, low-cycle fatigue loads from smaller earthquakes, poor maintenance, and several other factors have also increased the risk for a large portion of existing structures. These issues make existing structures unreliable and their outcome unpredictable without regular monitoring of the structure's integrity.

Structural Health Monitoring (SHM) is defined as the process of comparing the current state of a structure's condition relative to a healthy baseline state to detect the existence, location, and degree of likely damage during or after a damaging input, such as an earthquake. Many SHM algorithms have been proposed in the literature. However, a large majority of these algorithms cannot be implemented in real time. Therefore, their results would not be available during or immediately after a major event for urgent post-event response and decision making. Further, these off-line techniques are not capable of providing the input information required for structural control systems for damage mitigation. The small number of on-line or real-time SHM (RT-SHM) methods proposed in the past, resolve these issues. However, these approaches have significant computational complexity and typically do not manage nonlinear cases directly associated with relevant damage metrics.

In particular, many existing SHM techniques, either on-line or off-line, use linear baseline models that do not provide enough information on structure's dynamics.

Therefore, more comprehensive nonlinear baseline models that offer further structural parameters to be monitored and consequently provide more useful information on safety and serviceability of structures during or after an event should be implemented in RT-SHM algorithms. Finally, many available SHM methods require full structural response measurement, including velocities and displacements, which are typically difficult to measure. All these issues make implementation of many existing SHM algorithms very difficult if not impossible.

This thesis proposes simpler, more suitable algorithms utilising a nonlinear Bouc-Wen hysteretic baseline model for RT-SHM of a large class of nonlinear hysteretic structures. The RT-SHM algorithms are devised so that they can accommodate different levels of the availability of design data or measured structural responses. The second focus of the thesis is on developing a high-speed, high-resolution seismic structural displacement measurement sensor to enable these methods by using line-scan cameras as a low-cost and powerful means of measuring structural displacements at high sampling rates and high resolution. Analytical studies and computer simulations are undertaken to develop novel RT-SHM algorithms, evaluate their robustness under different ground motions, and to investigate their sensitivity to small yet important amounts of damage.

Overall, the RT-SHM algorithms developed are computationally-efficient, less dependent on the availability of design data or difficult to measure displacement responses, and use nonlinear baseline models that can provide more health monitoring information of the structure. These advantages over other existing RT-SHM methods enable more accurate SHM information and make the algorithms developed more amenable to RT-SHM of both existing and new nonlinear hysteretic structures and systems by the profession. The results are thus novel, crucial and significant steps

towards developing smart, damage-free structures and providing more reliable information for post-event decision making.

PUBLICATIONS

During the course of this research, a number of public presentations have been made, which are based on the work presented in this thesis. They are listed here for reference:

Peer-reviewed Journal Papers:

- **Nayyerloo, M,** Chase, JG, MacRae, GA, and Chen, XQ (2011). "LMS-based approach to structural health monitoring of nonlinear hysteretic structures," *Structural Health Monitoring, an International Journal*, Vol. 10(4), pp. 429-444, ISSN: 1475-9217.

- **Nayyerloo, M**, Chase, JG, MacRae, GA, Chen, XQ and Hann, CE (2010). "Structural Health Monitoring using Adaptive LMS Filters," *International Journal of Computer Applications in Technology (IJCAT),* Vol. 39(1/2/3), pp. 130-136, ISSN: 0952-8091 *(invited)*.

- **Nayyerloo, M,** Chase JG, Millane, A, Muller, C, Malherbe, A, Chen, XQ and MacRae, GA (2011). "Seismic structural displacement measurement using a line-scan camera: Camera calibration and experimental validation," *Journal of Civil Structural Health Monitoring (JCSHM)*, ISSN: 2190-5452 *(in print)*.

+1 under review:

- **Nayyerloo, M**, Chase, JG, Chen, XQ, Acho, L and Rodellar, J (2011). "A simple approach to on-line identification and health monitoring of nonlinear hysteretic structures using a fast and slow dynamics separation technique," *Smart Structures and Systems, an International Journal,* ISSN: 1738-1584.

Conference Papers:

- **Nayyerloo, M**, Acho, L, Rodellar, J, Chase, JG and Chen, XQ (2011). "A simple approach to real-time fault detection and diagnosis in base-isolation systems," *The 2011 Pacific Conference on Earthquake Engineering (PCEE 2011)*, Auckland, New Zealand, April 14-16, 8 pages, ISBN: 978-0-908960-58-3 *(paper and poster presentation).*

- **Nayyerloo, M**, Chase, JG, Chen, XQ, Acho, L, and Rodellar, J (2011). "A simple approach to on-line identification and health monitoring of nonlinear hysteretic structures using a fast and slow dynamics separation technique," *The 2011 CoDAlab-Mice Workshop on Control, Dynamics, Monitoring and Applications,* Barcelona, Spain, Feb 7-9, ISBN: 978-84-7653-539-4.

- **Nayyerloo, M**, Malherbe, A, Chen, XQ, Chase, JG and MacRae, GA (2010). "Cost-effective image-based seismic structural displacement measurement using a high-speed line-scan camera: experimental validation," *The New Zealand Society of Earthquake Engineering 2010 Conference (NZSEE 2010)*, Wellington, NZ, March 26-28, 8-pages, ISBN: 978-1-877561-60-3.

- **Nayyerloo, M**, Chase, JG, MacRae, GA and Chen, XQ (2009). "Cost-effective computer vision based structural health monitoring using adaptive LMS filters," *The 7th International Workshop on Structural Health Monitoring (IWSHM),* Stanford, CA, September 9-11, pp. 705-712, ISBN: 978-1-60595-007-5.

- **Nayyerloo, M**, Chase, JG, MacRae, GA, Moghaddasi, M, and Chen, XQ (2009). "Permanent deflection identification of nonlinear structures undergoing seismic excitation using adaptive LMS filters," *The New Zealand Society of Earthquake Engineering 2009 Conference (NZSEE 2009),* Christchurch, NZ, April 3-5, 8-pages, ISBN: 978-0-908960-52-1.

- **Nayyerloo, M**, Chase, JG, MacRae, GA and Chen, XQ (2008). "Structural health monitoring using adaptive LMS filters," *The 15th International Conference on Mechatronics and Machine Vision in Practice (M2VIP)*, Auckland, New Zealand, Dec 2-4, pp. 420-425, ISBN: 978-0-473-13532-4.

ACKNOWLEDGEMENTS

the respective chapters.

Finally, I am profoundly grateful to my parents, who always gave me endless love and support during difficult times. Without your ongoing support and dedication, I would not be where I am today.

TABLE OF CONTENTS

LIST OF FIGURES

LIST OF TABLES

NOMENCLATURE

ML	Local Magnitude or the Richter Scale
USGS	United States Geological Survey
ASCE	American Society of Civil Engineers
SHM	Structural Health Monitoring
ANN	Artificial Neural Networks
LMS	Least Mean Squares
ERA	Eigensystem Realization Algorithm
IASC	International Association for Structural Control
DDLV	Dynamic Damage Locating Vector
LSE	Least Squares Estimation
RLS	Recursive Least Squares
GPS	Global Positioning System
MLP	Multi-Layer Perceptron
ICA	Independent Component Analysis
WPT	Wavelet Packet Transform
WPS	Wavelet Packet Signature
EMD	Empirical Mode Decomposition
FOV	Field of View
RT-SHM	Real-time Structural Health Monitoring
DOF	Degree of Freedom
MDOF	Multiple-Degree-of-Freedom
SDOF	Single-Degree-of-Freedom
MSE	Mean Square Error
FEA	Finite Element Analysis
PGA	Peak Ground Acceleration
MR	Magneto-Rheological
SA	Sensitivity Analysis
LSA	Local Sensitivity Analysis
GSA	Global Sensitivity Analysis
RMS	Root Mean Square
FAST	Fourier Amplitude Sensitivity Test
PLLSQ	Piecewise Linear Least Squares
LVDT	Linear Variable Differential Transducer

PZT   Piezoelectric
LDV   Laser Doppler Vibrometer
3D   Three-Dimensional
CCD   Charge-Coupled Device
RTOS   Real-Time Operating System
HDD   Hard Disk Drive
FFT   Fast Fourier Transform
DPI   Dots per Inch
MCS   Monte Carlo Simulation
IQR   Inter-Quartile Range

CHAPTER 1

Introduction

Every year hundreds of people across the world lose their lives due to catastrophic earthquakes. The deadliest earthquake of the last two decades with a magnitude of 9.1 ML happened in the Northern Sumatra region of Indonesia in 2004 and claimed 227,898 lives, from the earthquake and resulting tsunami. A year after, another massive earthquake of 7.6 ML hit Kashmir in Pakistan and 80,361 people lost their lives. In 2008, another large, deadly earthquake of 7.9 ML occurred in Eastern Sichuan in China, and 87,587 people died. Finally in 2010, the 7.0 ML Haiti earthquake claimed 222,570 lives (USGS 2011).

Apart from loss of life, earthquakes damage residential, commercial and

industrial buildings, and equally importantly, infrastructure such as power plants, roads, and pipelines. The resulting damage can cost billions of dollars depending on the severity of the earthquake, and significantly delay economical and social return to normal activity.

The 1989 Loma Prieta earthquake in California struck Monterey to San Francisco with a magnitude of 6.9 ML and caused US$6 to US$10 of billion property loss (Page et al. 1999). In 1995, a magnitude 6.9 quake killed more than 6,000 people and caused US$100 billion in damage in Kobe-Japan (Michael et al. 1999). Recently, in February 2011, a large earthquake of magnitude 6.3 ML struck Christchurch area in New Zealand and claimed 181 lives (NZ Police 2011) and up to NZ$15 billion (approximately US$11.9 billion) damage (Villamor and the Science Response teams 2010; GNS 2011; NZ Government 2011; NZ Parliament 2011). Figure 1.1 shows some examples of the widespread damage to buildings and infrastructure in Christchurch. In this latter case, the figure was worsened by another massive 6.3 ML aftershock in June 2011. Finally, the down-time cost of infrastructure and main business activity sometimes exceeds the direct cost of damage to the property or the infrastructure itself.

Earthquakes may also trigger extremely destructive tsunami waves that significantly increase the negative impact of the quakes. An example of such catastrophic events recently occurred in Tohoku-Japan in March 2011. The immediate economic effects and casualties for this event are still unclear. However, the costs are estimated to be as high as US$200 billion (2.5% of the country's GDP) and over 10,000 people may have lost their lives (The World Bank 2011).

Such huge earthquakes can occur in many regions around the world, and may even cause more damage, as the existing structures become older. Research conducted by the US Geological Survey (USGS) and other researchers shows there is a 70%

2

probability of at least one magnitude 6.7 or greater earthquake striking the rapidly growing San Francisco Bay region before 2030 (Michael et al. 1999). Such an earthquake would cause widespread damage and consequently have a huge impact on the US economy.

Figure 1.1: Severe damage to Christchurch CBD from the February 2011 earthquake of magnitude 6.3 ML: top-left) collapse of residential buildings, top-right) extensive damage to roads, bottom-left & -right) widespread liquefaction around the city (Photos courtesy of Mohammad S. Ashtiani)

The great social and economical impact of earthquakes has attracted many researchers from different disciplines, such as geotechnical, structural and control engineering to the broad field of earthquake engineering to develop novel solutions for mitigating the catastrophic effect of earthquakes. Advancements in geotechnical and structural engineering help to have better understanding of ground motions and how structures behave against such motions, and thus enable more resilient structures in areas with high seismic risks, resulting in a safer and more resilient society.

The problem of increasing the level of safety of structures becomes complicated

when it comes to existing structures built years ago according to outdated design codes that did not have the knowledge or understanding that we have now. On the other hand, demand loads on some infrastructure, such as bridges and roads have also increased. The combination of increasing demand, outdated design, and, in some cases, poor maintenance has increased the risk for a large portion of our infrastructure, which may have an inadequate level of safety compared to current design codes.

Other complexities come into the problem when existing structures experience several minor or moderate earthquakes during their life time or become aged. Aging and being subject to relatively low-cycle fatigue loads, resulting from smaller earthquakes, ensure the structure performs differently from what it was originally designed to do. Such fatigue loads may be lower than design levels and cause no visible damage in the structure, but significantly shorten the remaining life of the structure (Vayas et al. 2003; Erberik and Sucuoglu 2004; Sucuoglu and Erberik 2004; Teran-Gilmore and Jirsa 2007; Nastar et al. 2010). Moreover, nonlinearities, usually neglected or simplified in the design procedures, affect the structure's performance against earthquake loads during its service life. Overall, these issues make existing structures unreliable and their outcome unpredictable without regular monitoring of the structure's integrity. It is particularly important for critical infrastructure, such as hospitals and major lifelines, which are most needed after catastrophic events.

Replacement of old existing structures may seem the simplest option to increase the safety level of such structures and to remove the need for continuous monitoring. However, this option is expensive and thus rarely possible. For instance, the total investment needed to bring bridge infrastructure in the US up to code, over a five-year period, is estimated by The American Society of Civil Engineers (ASCE) to be US$930 billion. However, only US$549.5 billion is planned to be spent over this period

(Ahlborn et al. 2010). Monitoring of existing structures can be used to improve such funding allocations by improving the information that these decisions are based on.

Structural Health Monitoring (SHM) is defined as the process of comparing the current state of a structure's condition relative to a healthy baseline state to detect the existence, location, and degree of likely damage after a damaging input, such as an earthquake. SHM can simplify and improve typical visual or localized experimental approaches, as it does not require subjective visual inspection of the structure (Doherty 1993). It can thus provide valuable data for post-event safety assessments to help optimize recovery planning.

Sohn et al. (2004) describe SHM as a four-part process:

1. Operational Evaluation

2. Data Acquisition, Fusion, and Cleansing

3. Feature Extraction and Information Condensation, and

4. Statistical Model Development for Feature Discrimination.

Operational evaluation determines economic and/or life safety motivations, damage definitions, conditions both operational and environmental under which the system functions, and, finally, limitations on data acquisition in the operational environment. Data acquisition covers topics such as determination of the quantities to be measured, the sensors type, location, number, resolution, and bandwidth, the data acquisition/storage/transmittal hardware, and how often the data should be collected. The third step in the process is feature extraction, which is the process of identifying damage-sensitive properties from measured vibration responses to determine existence, location, type, and the extent of damage. Finally, statistical models are used to determine whether the changes observed in the selected features used to identify damage are statistically significant (diagnosis). Similar models are also used to estimate

the remaining useful life of the structure (prognosis).

The main focus of this thesis is on the third part of the SHM process, developing novel feature extraction techniques, with the aim of resolving problems of existing feature extraction algorithms to provide better resolution, accuracy and relevance. A major drawback of many existing approaches, which will be reviewed in this chapter, is their inability to be implemented in real-time, on a sample-to-sample basis as the event occurs. Hence, these methods are not suitable for real-time structural control for damage mitigation purposes, and their results would not be immediately available after an event.

Among many proposed SHM techniques in the literature, only a very few, such as adaptive fading Kalman filters (Sato and Takei 1997; Loh et al. 2000), adaptive H_∞ filter techniques (Sato and Qi 1998), bootstrap filtering approaches (Li et al. 2004a), Artificial Neural Networks (ANNs) based methods (Masri et al. 2000; Zapico and et al. 2001; Zang et al. 2004), or wavelet approaches (Kim and Melhem 2004) can achieve real-time or near real-time results. However, they have either significant computational cost and complexity, or are incapable of locating and quantifying the damage detected. Therefore, developing on-line SHM techniques with simpler and more suitable algorithms is still a challenging field.

This thesis proposes real-time SHM (RT-SHM) algorithms for nonlinear hysteretic structures using simpler and more suitable techniques for on-line SHM of such structures than the existing methods in the literature. It uses a simple adaptive Least Mean Squares (LMS) filtering technique, a fast and slow dynamics separation method, and a simple comparison between the internal dynamics of healthy and faulty structures to develop three SHM algorithms suitable for health monitoring of a large class of nonlinear hysteretic structures with different levels of availability of design data. Thus, the methods proposed are suitable for on-line monitoring of both existing

and new hysteretic structures and systems.

In structural systems, hysteresis appears as a natural mechanism in the materials used and produces restoring forces that dissipate energy. Hysteresis, as used here, refers to the memory nature of inelastic structural behaviour where the restoring forces depend not only on the instantaneous deformations, but also on the history of the deformations. The detailed analytical modelling of this behaviour results in very complicated, nonlinear models that are not suitable for on-line identification and health monitoring applications using existing methods. Therefore, semi-physical modelling, which is a combination of simplified physical analysis and black-box modelling, is usually used to represent hysteretic behaviour in structures.

One of the most common such semi-physical models proposed is a first-order nonlinear differential equation known as the Bouc-Wen model. It was originally proposed by Bouc (1967) and later was further generalized by Wen (1976). Choosing a set of suitable parameters in the model relates input displacements to output restoring forces in a broad range of hysteretic structures. The Bouc-Wen model is able to capture a range of hysteresis loop shapes that match the behaviour of a wide class of hysteretic systems including buildings, soil, base-isolation systems, and magneto-rheological (MR) dampers among others (Ismail et al. 2009). This thesis uses the Bouc-Wen model of hysteresis to simulate nonlinear hysteretic behaviour in structures and systems, and develops SHM methods to directly identify changes in both the key structural and Bouc-Wen model parameters in real-time.

The methods developed require full-state structural responses: accelerations, velocities, and displacements. However, due to a variety of practical constraints and the high cost of implementation, direct high-speed measurement of structural displacement and velocity is typically difficult. Estimation of velocity and displacement by

integration of measured acceleration is also subject to drift and error, which needs to be corrected using independent displacement data, particularly, where permanent displacements exist (Yang et al. 2006; Stiros 2008). Hence, the second focus of the thesis is on developing a high-speed, high-resolution structural displacement measurement sensor for the SHM methods developed. This latter concept contributes to the second step of the SHM process, data acquisition, by introducing line-scan cameras as a low-cost and powerful means of measuring seismic structural displacements at high sampling rates and high resolutions.

The following sections present a brief review of the existing literature on the third step of the SHM process, covering a range of SHM algorithms. The existing literature on structural displacement measurement techniques is reviewed later in the relevant chapters.

1.1. Literature review on SHM algorithms

Existing SHM algorithms in the literature can be categorized into two main groups: parametric and non-parametric methods. In parametric SHM, the mathematical model governing the structural behaviour is known and the aim is to identify likely changes in the structural parameters with respect to a baseline model to detect and locate damage. In contrast, non-parametric methods map the inputs to the structure to its outputs without any knowledge about the internal structural model. Damage is then detected by identifying changes in the parameters of the generic or non-physical model created. Nevertheless, non-parametric models cannot locate the damage detected unless *a priori* knowledge from all possible damage cases and the corresponding structural responses is available. However, a significant advantage of non-parametric SHM methods over the parametric approaches is their capability to capture the full dynamics

of the structure including un-modelled or simplified dynamics.

1.1.1. Parametric Methods

Many current vibration-based SHM methods are based on the idea that changes in modal parameters: frequencies, mode shapes, and modal damping, are a result of damage or decay (Doebling et al. 1996). The idea was first proposed by Chen et al. (1977) who found longer time period, higher damping, and some mode shape discontinuity for the damaged structure in a forced vibration test on a full-scale four-storey concrete model building. However, modal properties are not robust in the presence of noise and are not sensitive to small amounts of damage (Farrar et al. 1994). Moreover, sometimes damage at two different locations result in exactly the same shifts in the natural frequencies, and the damage cannot be uniquely localized. Further, modal-based methods are typically more applicable to steel-frame and bridge structures where vibration response is highly linear (Doebling et al. 1996; Chase et al. 2005b).

The most common method for identification of modal parameters in civil structures is the Eigensystem Realization Algorithm (ERA), using time domain free vibration response data (Juang 1985). In ERA, a discrete Hankel matrix is formed, the state and output matrices determined, and a continuous time system model created. The natural frequencies and mode shapes are then found by determining the eigenvalues of this continuous time system. Dyke et al. (2000) use cross-correlation functions in conjunction with the ERA method for identification of the modal parameters, which are used to identify frequency and damping parameters. Caicedo et al. (2000) introduce SHM methods based on changes in the component transfer functions of the structure, or transfer functions between the floors of a structure, and use the ERA to identify the natural frequencies of each component transfer function. They also presented ERA-based methods to identify modal parameters before using least squares optimization to

locate and identify damage (Caicedo et al. 2004).

Lus et al. (2004) presented ERA methods using a Kalman filter estimator to identify a baseline model and the ERA method for modal parameters before using least squares optimization to locate and identify damage. Lus and Betti (2000) also proposed a damage identification method based on ERA with a Data Correlation and Kalman Observer. Bernal and Gunes (2000) also used ERA with a Kalman Observer for identifying modal characteristics when the input is known, and used a subspace identification algorithm when the input cannot be measured. A novel modal identification based approach was also presented by Barroso and Rodriguez (2004) who employed a damage index method to identify changes in stiffness mass ratios for the IASC-ASCE (International Association for Structural Control-American Society of Civil Engineers) benchmark structure.

Flexibility-based methods are generally more sensitive to changes in the first few natural modes, which also dominate the response of many typical civil structures, than the modal-based techniques. Lin (1990) uses the cross-unity check between the flexibility matrix obtained from measured data and the analytical stiffness matrix to locate damage. Bernal and Gunes (2004) presented a flexibility-based method that involved sub-matrix inverses and the full data record to perform modeless identification. Bernal (2007) also introduces Dynamic Damage Locating Vectors (DDLVs) approach for structural damage detection and localization. DDLVs lie in the null space of the change in the transfer matrix and provide Laplace transform of dynamic loads, and thus, result in zero stress fields over the damaged region.

The problem of damage detection can also be seen as an inverse problem. Using measured input-output vibration data, analytical model of the structure can be updated to reproduce the measured data. Minimizing the error between the reproduced and

measured responses by iteratively refining the stiffness and mass matrices yields the damaged structure's parameters (Lus et al. 2003a; Lus et al. 2003b). Some recently published methods also include Bayesian statistical approaches using one or two stages to identify modal parameters and then damage (Lam et al. 2004; Yuen et al. 2004).

The parametric SHM methods reviewed are used mainly as off-line techniques because post processing of measured time history data is required to extract the necessary diagnostic information. However, the inability of off-line SHM techniques to be implemented in real-time, on a sample-to-sample basis as the event occurs, makes them unsuitable for real-time structural control for damage reduction purposes upon detecting damage. Equally, their outcomes may not be available immediately after an event, perhaps reducing their potential, positive impact on immediate earthquake response. In contrast, on-line/real-time methods provide all the necessary information to plan damage mitigation measures in advance, and thus, avoid catastrophic failures, as well as aiding immediate post-event response.

Adaptive fading Kalman filters (Sato and Takei 1997; Loh et al. 2000), adaptive H_∞ filter techniques (Sato and Qi 1998), and bootstrap filtering approaches (Li et al. 2004a) can achieve real-time or near real-time results and provide structural parameter identification. However, they have significant computational cost and complexity that makes the implementation of such methods for on-line SHM difficult.

Simpler algorithms for on-line SHM make use of adaptive Least Squares Estimation (LSE). Chassiakos et al. (1998) uses adaptive least squares approach for on-line identification of hysteretic systems through reliable estimates of the hysteretic restoring force parameters using acceleration data. This work was extended by Smyth et al. (1999) to handle the general case when no information is available on the system parameters.

Lin et al. (2001) presented a Recursive Least Squares (RLS) based algorithm that upgrades the diagonal elements of the adaptation gain matrix sample-to-sample by comparing the values of estimated parameters between two consecutive time steps. The method requires full-state structural response measurement. Yang et al. (2004) also proposed an on-line adaptive least-square tracking technique that uses only acceleration data to identify abrupt changes in the parameters of hysteretic structures, from which structural damage can be determined.

MX Least Mean Squares (MX-LMS) filters, named after their modular cross-coupled structure, were also used by Kaiser et al. (1999) to identify modal parameters in the health monitoring of adaptive aerospace structures. The changes of these parameters are then related to the location and extent of damage.

Model-based methods combined with adaptive LMS filtering theory were also used to identify structural stiffness changes in real-time in a computationally efficient and robust fashion. Adaptive LMS filters approximate gradient optimization and convergence in real-time from sample-to-sample. In contrast, least squares structural optimization methods use the full data record and multiple computational analyses to converge to a solution.

LMS-based SHM has been used for a benchmark problem (Chase et al. 2005b), and also for a highly nonlinear rocking structure (Chase et al. 2005c), to directly identify changes in structural stiffness only. Similar RLS methods have also been applied to the same problem (Chase et al. 2005a). All these methods directly identify changes in structural stiffness over time by comparing the stiffness matrix of a structure with the undamaged model matrix. These model-based adaptive filtering methods are robust with fast convergence and low computational cost. However, they do not identify plastic and permanent deflections, and require full-state structural response

measurement.

Hann et al. (2009) proposed a SHM method for nonlinear hysteretic dynamics identification using convex integral-based fitting methods and Piecewise Linear Least Squares (PLLSQ) fitting. The method uses only acceleration measurements and infrequently measured displacements motivated by global positioning system (GPS), and is also capable of identifying plastic and permanent deflections in real-time. The identified permanent displacement is a particularly useful damage measure for the construction of probabilistic fragility functions.

1.1.2. Non-parametric Methods

Artificial Neural Networks (ANNs) are one of the common non-parametric SHM methods. A neural network is composed of many layers with weight factors and a bias value. Outputs of one layer are multiplied by its weights and shifted by the layer's bias value and then used as inputs to the next layer. The weights and biases are adjusted during the training phase of the ANN to minimize error between measured and predicted outputs of the structure. When damage occurs, the weights change to compensate changes in the outputs of the structure due to the damage. However, the non-uniqueness of the set of the network weights calculated for a particular type or form of damage makes it difficult to relate changes in the weights to the location and severity of the damage occurred. Equally, training sets may not generalise well to actual damage, or remain relevant over time.

Masri et al. (1992; 2000) proposed an ANN-based method that can detect changes in an unknown system's nonlinear dynamic behaviour based on the level of output prediction error when measured responses of a damaged system are passed through the network trained to predict the undamaged state responses. However, it is difficult to relate this information to locate or quantify the damage detected.

In another study, Zapico et al. (2001) proposed a procedure based on a Multi-Layer Perceptron (MLP) for damage assessment in a two-storey steel frame with steel-concrete composite floors. The MLPs were trained using a simplified finite element model through the error back-propagation algorithm. The two longitudinal bending natural frequencies were used as inputs to the MLPs to determine damage at floor levels. Nevertheless, more knowledge of the damage level at each floor, for example through analysing the experimental frequency response functions of the damaged structure, is needed to validate the results.

Zang et al. (2004) also presented an approach to detect structural damage based on a combination of Independent Component Analysis (ICA) extraction of time domain data and ANN to detect damage in a truss structure also in a three-storey bookshelf-type model building. The ICA technique used captures the essential structure of a large volume of the measured vibration data to be used in the ANN training phase.

Discrete and continuous wavelet analyses have also been used in SHM. A good review of the research on damage detection using wavelet analysis can be found in (Kim and Melhem 2004). One example of wavelet-based approaches is a statistical pattern classification method, developed by Sun and Chang (2004), based on Wavelet Packet Transform (WPT). This method uses acceleration responses of the free end of a steel cantilever I-beam excited by a pulse load to detect induced damage in the beam in the form of line cuts of different severities in the flange. The responses are decomposed into wavelet packet components, and dominant signal energies of the wavelet packet components are then used as the Wavelet Packet Signature (WPS) for damage detection. Two damage indicators were formulated by Sun and Chang to lump the discriminate information from the extracted WPS with thresholds set based on the statistical properties and successive measurements.

14

Wavelet-based methods determine the time at which damage occurred (Hou et al. 2000; Hera and Hou 2004). Damage, and the moment when the damage occurs, can be detected by a spike or an impulse in the plots of higher resolution details from wavelet decomposition of the acceleration response data. Hera and Hou (2004), also used the spatial distribution pattern of the observed spikes to determine the region in which the damage occurred.

Empirical Mode Decomposition (EMD) has also been used for damage detection. Yang et al. (2004) used EMD to extract sudden stiffness damage time instants and locations over the full measured record. They also used EMD and Hilbert–Huang linear transforms to identify damage time instants, as well as natural frequencies and damping ratios of the structure before and after damage using measured data. However, these methods are complex, and require the full record and sometimes operator input to arrive at a final diagnosis, therefore they are neither on-line nor automated.

1.2.   Final Statements on the literature

The SHM field is too large to present a complete literature review. Similar approaches can be found in excellent reviews by Doebling et al. (1998), Sohn et al. (2004), Carden and Fenning (2004), Montalvao et al. (2006), and Dharap (2006). Overall, despite the extensive efforts made by the SHM community, it can be seen that there is still a great need for further developments in the following areas:

- Many existing SHM algorithms cannot be implemented in real time. Therefore, their results would not be available during or immediately after an event for urgent post-event response. Further, these off-line techniques are not capable of providing the input information required for structural control systems for damage mitigation. On-line SHM methods resolve

these issues. However, existing on-line SHM approaches have significant computational complexity. Therefore, developing computationally-efficient and more suitable algorithms for RT-SHM is crucial in developing damage-free structures, providing more reliable information for post-event decision making and consequently more resilient communities to devastating earthquakes.

- Many existing off-line or on-line SHM methods require full structural response measurement, including velocities and displacements that are typically difficult to measure. Novel displacement and velocity sensors would provide the inputs required for many SHM algorithms and make their implementation by the profession possible.

- Parametric SHM methods are generally more suitable for SHM because of their ability to determine type and location of damage over the non-parametric approaches. However, many parametric SHM techniques use linear baseline models that do not provide enough information about the structure. More comprehensive nonlinear baseline models offer further structural parameters to be monitored and consequently more useful information on safety and serviceability of structures after an event.

1.3.   Objectives and scope

The main objective of this study is to develop simple RT-SHM algorithms, capable of on-line tracking of the key structural parameters including stiffness, damping, and the governing nonlinear baseline model parameters, for a large class of Bouc-Wen-type hysteretic structures. The RT-SHM information made available by the algorithms developed will then provide the necessary input data required by many structural control methods for damage mitigation or avoidance purposes. Further, the identified nonlinear baseline model with measured displacement data provides a very useful measure for safety and serviceability of structures, plastic and permanent deformations.

Analytical studies and computer simulations are undertaken to develop the algorithms, evaluate their robustness under different ground motions, and to investigate their sensitivity to small yet important amounts of damage. Availability of the required input data by the algorithms is investigated as one of the main implementation issues. The study focuses on several main areas:

- Development and proof-of-concept computer simulations of RT-SHM algorithms for new structures or where limited *a priori* knowledge of the structure is typically available.

- Development and *in silico* validation of RT-SHM algorithms for old structures or where usually no design data is available.

- Robustness evaluation of the developed algorithms under different ground excitations and assessment of their sensitivity to small amounts of damage that may lead to larger damage and eventually failure of the structure.

- Investigation of emerging line-scan cameras as a new means of

measuring structural displacements at high sampling rates and high resolution to provide the displacement inputs required for on-line SHM methods. This investigation is conducted through several random and sinusoidal experimental tests simulating the range of possible, actual structural displacement data.

- Study of the implementation issues of the proposed line-scan based displacement measurement method, such as camera-pattern calibration, high resolution measurement of seismic motions with different scales over a fixed field of view (FOV), and others is also presented to define the range and capability of the approach.

1.4.   Preface

Chapter 2 presents the development and simulation results of a modified adaptive LMS-based SHM method using the nonlinear Bouc-Wen structural baseline model to directly identify both changes in stiffness and plastic deflections in real-time. A novel computationally-efficient structural identification method with two steps is presented that assumes limited *a priori* knowledge of the structure's potential nonlinear behaviour based on readily available design information. The effect of the specific external load on performance of the proposed SHM method is also evaluated using a suite of 20 different ground motions to test robustness of the results.

Chapter 3 presents a novel real-time health monitoring technique based on a comparison between known internal dynamics of the healthy structure with measured dynamics of the faulty system. The method is developed in the context of fault detection and diagnosis in seismic base-isolation systems as it is an increasingly applied structural

design technique in highly seismic areas (Martelli 2009). The governing nonlinear hysteretic model of the base-isolation system is assumed to be known prior to the damage detection based on available design data.

Chapter 4 presents a sensitivity analysis on the Bouc-Wen model parameters to investigate how changes in the hysteretic baseline model parameters affect the hysteresis loops shape, representing the nonlinear behaviour of the structure, and the overall structural responses. Outcomes of the analysis provide ground for making decisions on the possibility of reducing the number of baseline model parameters to broaden the application of the proposed SHM methods to cases where limited knowledge of the structure is available for identification of all of the nonlinear baseline model parameters.

Chapter 5 introduces a new real-time algorithm for structural identification and health monitoring of nonlinear Bouc-Wen type hysteretic structures without *a priori* knowledge of the structure. The method proposed uses a fast and slow dynamics separation technique to identify and track the structural parameters over time. Robustness of the method under different ground motions and different possible damage scenarios is assessed.

Chapter 6 explores the idea of using high-speed line-scan cameras as a powerful means of measuring seismic structural displacements at high sampling rates and high resolutions. The original method proposed by Lim et al. (2008) for foundation pile movements measurement is modified and evaluated for seismic displacement measurement through different tests with harmonic and random target displacements. A new edge tracking algorithm is proposed for the method that makes it amenable to systems where displacements occur across a range of scales, while maintaining or improving resolution. Moreover, a simple camera-pattern calibration procedure is

developed that guarantees fulfilment of all the basic assumptions made in the original work and thus significantly increases the measurement results accuracy.

Chapter 7 uses a Monte Carlo simulation of 100k randomly selected possible displacement measurement cases uniformly distributed over the specified ranges of different parameters involved in the proposed displacement measurement method to evaluate the effect of incorrectness in the dimensions of the printed pattern used on the accuracy of the output displacement results. It thus quantifies the potential sources of error in terms of quantifiable errors in the pattern used.

Chapters 8 and 9 present the overall conclusions to the research and discuss possible extensions and future work.

1.5.   Summary

This chapter presented the motivations for this thesis followed by an overview from the health monitoring algorithms and required sensors and measurement techniques developed within this thesis. Overall, the development of RT-SHM methods and the required instruments provides the necessary input data to structural control methods with damage mitigation purposes, and thus is crucial in developing damage-free structures and consequently more resilient communities to devastating earthquakes. Equally, they provide diagnostic data to inform decision making both before and after an event.

The key issue with the existing health monitoring methods is their extensive complexity to be implemented in real-time. Further, providing the displacement data required by these algorithms is a challenging task. The development of more computationally-efficient algorithms and novel displacement sensors would enable

implementation of real-time health monitoring algorithms by the profession, and constitute a significant step forward toward damage-free structures becoming a realistic design alternative, as well as providing better information to decision makers at all levels of disaster planning and management.

Simplicity is the ultimate sophistication.

Leonardo da Vinci
Italian Polymath, 1452-1519

CHAPTER 2

LMS-based approach to RT-SHM

2.1. Introduction

A major drawback of many SHM approaches reviewed in the previous chapter is their inability to be implemented in real time, on a sample-to-sample basis, as the event occurs. Therefore, these methods are not suitable for real-time structural control for damage reduction purposes. Further, their results would not be available during or immediately after an event for immediate post-event response.

Adaptive fading Kalman filters (Sato and Takei 1997; Loh et al. 2000), adaptive

H$_\infty$ filter techniques (Sato and Qi 1998), Monte Carlo filter based methods (Yoshida 2001), and bootstrap filtering approaches (Li et al. 2004a) can achieve real-time or near real-time results. However, they have significant computational cost and complexity. Simpler and more suitable algorithms for RT-SHM make use of LSE with different stochastic gradient estimation approaches (Chassiakos et al. 1998; Smyth et al. 1999; Lin et al. 2001; Yang and Lin 2004; Chase et al. 2005a; Chase et al. 2005b; Chase et al. 2005c).

The last two LSE-based algorithms referenced use model-based methods combined with adaptive LMS filtering theory and offer even a more computationally-efficient and robust method for RT-SHM. LMS-based SHM has been used for a benchmark problem (Chase et al. 2005b), and also for a highly nonlinear rocking structure (Chase et al. 2005c), to directly identify changes in structural stiffness only. The model-based adaptive filtering approach is robust with fast convergence and low computational cost. However, the baseline model used is linear, and therefore, cannot fully represent nonlinear structural dynamics. Further, the method requires full-state structural response measurement, which, as discussed in the previous chapter, is typically very difficult. The former issue is addressed in this chapter and the latter in Chapters 6 and 7.

This chapter develops a modified adaptive LMS-based SHM method using the nonlinear Bouc-Wen structural baseline model to directly identify both changes in stiffness and the nonlinear baseline model parameters in real time. A novel computationally-efficient structural identification method with two steps is presented that assumes limited *a priori* knowledge of the structure's potential nonlinear behaviour based on readily available design information. Further, the effect of specific external loads on performance of the proposed SHM method is evaluated using a suite of 20

different actual ground motion acceleration records to test robustness of the results.

Overall, the method thus provides more health monitoring information of the structure. In particular, the algorithm offers very useful measures for determining the safety and serviceability of structures after a major seismic event, plastic and permanent displacements. It thus provides unique nonlinear information that has direct relevance to structural damage and serviceability.

2.2.   Definition of the SHM problem

A seismically excited nonlinear structure can be modelled at each time step using incremental equations of motion:

$$\mathbf{M}\cdot\{\Delta\ddot{v}\}+\mathbf{C}\cdot\{\Delta\dot{v}\}+\mathbf{K_T(t)}\cdot\{\Delta v\}=-\underline{\mathbf{M}}\cdot\Delta\ddot{x}_g \qquad (2.1)$$

where $\mathbf{M}$, $\mathbf{C}$, and $\mathbf{K_T}$ are the mass, damping, and tangent stiffness matrices of the model, respectively, $\{\Delta v\}$, $\{\Delta\dot{v}\}$, and $\{\Delta\ddot{v}\}$ are the changes in displacement, velocity, and acceleration vectors, respectively, and $\ddot{x}_g$ is the change in the ground motion acceleration over the time step.

The tangent stiffness matrix of a hysteretic structure can be represented using the Bouc-Wen model (Bouc 1967; Wen 1976). For instance, the tangent stiffness matrix of a four-degree-of-freedom (4-DOF) four-storey shear-type structure, as an example for the tangent stiffness matrix of a hysteretic structure in multi-degree-of-freedom (MDOF) case, can be written:

$$(\mathbf{K_T})_{11} = [\alpha_1 + (1-\alpha_1)Y_1 \frac{\Delta z_1}{\Delta v_1}](k_0)_1 + \alpha_2(k_0)_2$$

$$(\mathbf{K_T})_{12} = -[\alpha_2 + (1-\alpha_2)Y_2 \frac{\Delta z_2}{\Delta v_2}](k_0)_2$$

$$(\mathbf{K_T})_{21} = -\alpha_2(k_0)_2$$

$$(\mathbf{K_T})_{22} = [\alpha_2 + (1-\alpha_2)Y_2 \frac{\Delta z_2}{\Delta v_2}](k_0)_2 + \alpha_3(k_0)_3$$

$$(\mathbf{K_T})_{23} = -[\alpha_3 + (1-\alpha_3)Y_3 \frac{\Delta z_3}{\Delta v_3}](k_0)_3$$

$$(\mathbf{K_T})_{32} = -\alpha_3(k_0)_3 \qquad (2.2)$$

$$(\mathbf{K_T})_{33} = [\alpha_3 + (1-\alpha_3)Y_3 \frac{\Delta z_3}{\Delta v_3}](k_0)_3 + \alpha_4(k_0)_4$$

$$(\mathbf{K_T})_{34} = -[\alpha_4 + (1-\alpha_4)Y_4 \frac{\Delta z_4}{\Delta v_4}](k_0)_4$$

$$(\mathbf{K_T})_{43} = -\alpha_4(k_0)_4$$

$$(\mathbf{K_T})_{44} = [\alpha_4 + (1-\alpha_4)Y_4 \frac{\Delta z_4}{\Delta v_4}](k_0)_4$$

$$(\mathbf{K_T})_{13} = (\mathbf{K_T})_{14} = (\mathbf{K_T})_{24} = (\mathbf{K_T})_{31} = (\mathbf{K_T})_{41} = (\mathbf{K_T})_{42} = 0$$

where $(\mathbf{K_T})_{ij}$, $i,j = 1,...,4$, are components of the 4×4 tangent stiffness matrix, $0 \leq \alpha_i \leq 1$, $i=1,...,4$, is the ith storey bi-linear factor, which determines the change in slope between elastic and plastic regimes of that storey ($\alpha_i=0$ represents a fully hysteretic and $\alpha_i=1$ a fully elastic structure.), and z_i, $i=1,...,4$, is the dimensionless hysteretic component of the ith storey and is governed by the following first-order nonlinear differential equation (Constantinou and Tadjbakhsh 1985; Ikhouane and Rodellar 2007):

$$\dot{z}_i(t) = \frac{A_i\dot{r}_i(t) - \beta_i|\dot{r}_i(t)||z_i(t)|^{n_i-1}z_i(t) - \gamma_i\dot{r}_i(t)|z_i(t)|^{n_i}}{Y_i}$$

$$A_i > 0, \beta_i > 0, -\beta_i < \gamma_i \leq \beta_i, n_i \geq 1 \qquad (2.3)$$

$$i = 1,...,N$$

where A_i, β_i, γ_i, and n_i are stiffness, loop fatness, loop pinching, and abruptness parameters in the classical Bouc-Wen model, respectively. Further, n_i, the power factor, determines the sharpness of the curve from elastic to plastic force-deflection behaviour of each storey. Finally, $\dot{r}_i(t)$ is the velocity of storey i relative to storey i-1, Y_i is the yield displacement of ith story, and N is the number of stories in a shear-type structure. The five dimensionless parameters, A_i, β_i, γ_i, n_i, and α_i determine the hysteresis loop

shape. The conditions under Equation (2.1) limit the loop shape to the actual hysteretic behaviour seen in physical systems. Hysteresis loops that do not satisfy these conditions do not represent a physical hysteretic behaviour (Ikhouane and Rodellar 2007). Detailed information on the Bouc-Wen model can be found in an excellent review by Ismail et al. (2009).

Neither degradation nor pinching of hysteresis is accounted for by the classical Bouc-Wen model. Over the years, this classical model has been modified to a more contemporary version. This version accommodates changes in hysteresis loops arising from deteriorating systems (Baber and Noori 1986).

In this study, as illustrated in Figure 2.1a, the classical Bouc-Wen model, in conjunction with a variable linear structural stiffness over time, has been used to model nonlinearities arising from both the hysteretic behaviour of the structure and degradation of structural stiffness including model error. As shown in Figure 2.1b, the hysteretic baseline model parameters may also change over time due to damage to the structure. This latter behaviour is accounted for in Section 2.5 by introducing an on-line identification method for the Bouc-Wen model parameters.

The overall approach can also detect combination of the two damage scenarios, nonlinear yielding damage and structural stiffness degradation. Overall, with more *a priori* knowledge, the more detailed contemporary baseline model could be used and more damage cases be considered.
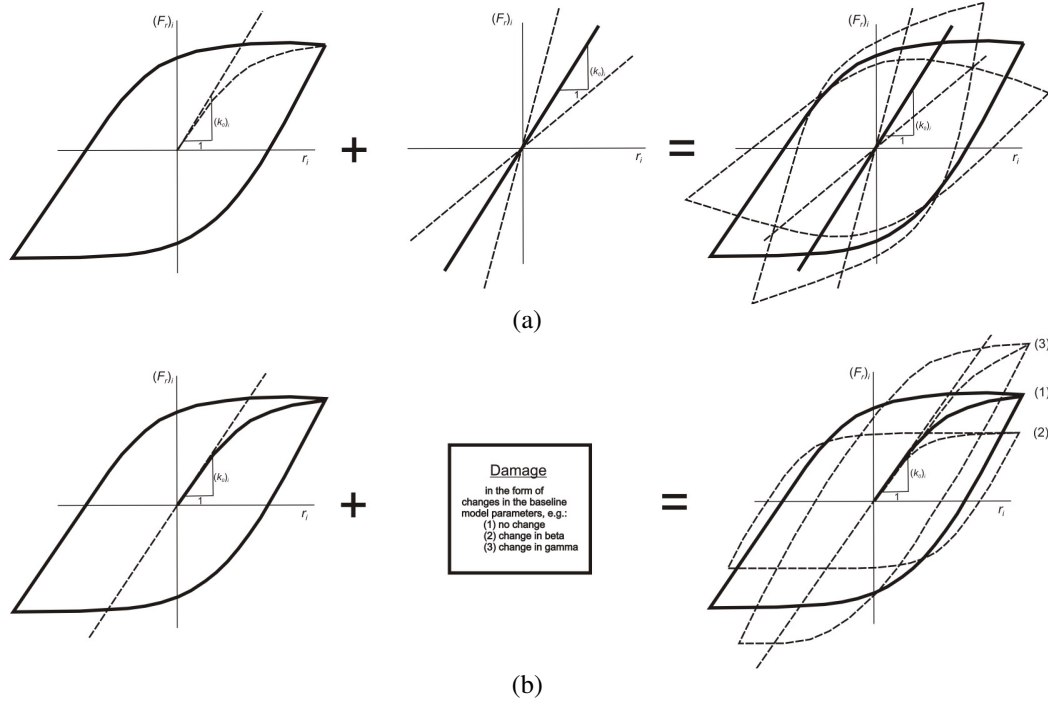
Figure 2.1: Damage models used: a) change in stiffness and b) change in the hysteretic baseline model parameters ($(F_r)_i$ is the restoring force of storey i)

Since the Bouc-Wen model captures dominant energy dissipation due to nonlinear behaviour, structural damage may be assessed by its impact on stiffness and plastic deformations over time. The potentially time-varying equations of motion for a damaged structure can be defined:

$$\mathbf{M}\cdot\{\Delta\ddot{\bar{v}}\}+\mathbf{C}\cdot\{\Delta\dot{\bar{v}}\}+(\overline{\mathbf{K}}_{\mathbf{T}}(\mathbf{t})+\Delta\overline{\mathbf{K}}_{\mathbf{T}}(\mathbf{t}))\cdot\{\Delta\bar{v}\}=-\underline{\mathbf{M}}\cdot\Delta\ddot{x}_g \qquad (2.4)$$

where $\{\Delta\ddot{\bar{v}}\}$, $\{\Delta\dot{\bar{v}}\}$, and $\{\Delta\bar{v}\}$ are the measured changes in responses of the damaged structure, $\overline{\mathbf{K}}_{\mathbf{T}}$, is the tangent stiffness matrix of the damaged structure from Equation (2.2) using damaged structural responses, and $\Delta\overline{\mathbf{K}}_{\mathbf{T}}(\mathbf{t})$ contains changes in the tangent stiffness of the structure due to damage and can be a function of time. Using the Bouc-Wen model of Equation (2.2), $\Delta\overline{\mathbf{K}}_{\mathbf{T}}$ can be written:

$$(\Delta \overline{\mathbf{K}}_{\mathbf{T}})_{11} = [\alpha_1 + (1-\alpha_1)Y_1 \frac{\Delta \overline{z}_1}{\Delta \overline{v}_1}](\Delta k_0)_1 + \alpha_2 (\Delta k_0)_2$$

$$(\Delta \overline{\mathbf{K}}_{\mathbf{T}})_{12} = -[\alpha_2 + (1-\alpha_2)Y_2 \frac{\Delta \overline{z}_2}{\Delta \overline{v}_2}](\Delta k_0)_2$$

$$(\Delta \overline{\mathbf{K}}_{\mathbf{T}})_{21} = -\alpha_2 (\Delta k_0)_2$$

$$(\Delta \overline{\mathbf{K}}_{\mathbf{T}})_{22} = [\alpha_2 + (1-\alpha_2)Y_2 \frac{\Delta \overline{z}_2}{\Delta \overline{v}_2}](\Delta k_0)_2 + \alpha_3 (\Delta k_0)_3$$

$$(\Delta \overline{\mathbf{K}}_{\mathbf{T}})_{23} = -[\alpha_3 + (1-\alpha_3)Y_3 \frac{\Delta \overline{z}_3}{\Delta \overline{v}_3}](\Delta k_0)_3$$

$$(\Delta \overline{\mathbf{K}}_{\mathbf{T}})_{32} = -\alpha_3 (\Delta k_0)_3 \tag{2.5}$$

$$(\Delta \overline{\mathbf{K}}_{\mathbf{T}})_{33} = [\alpha_3 + (1-\alpha_3)Y_3 \frac{\Delta \overline{z}_3}{\Delta \overline{v}_3}](\Delta k_0)_3 + \alpha_4 (\Delta k_0)_4$$

$$(\Delta \overline{\mathbf{K}}_{\mathbf{T}})_{34} = -[\alpha_4 + (1-\alpha_4)Y_4 \frac{\Delta \overline{z}_4}{\Delta \overline{v}_4}](\Delta k_0)_4$$

$$(\Delta \overline{\mathbf{K}}_{\mathbf{T}})_{43} = -\alpha_4 (\Delta k_0)_4$$

$$(\Delta \overline{\mathbf{K}}_{\mathbf{T}})_{44} = [\alpha_4 + (1-\alpha_4)Y_4 \frac{\Delta \overline{z}_4}{\Delta \overline{v}_4}](\Delta k_0)_4$$

$$(\Delta \overline{\mathbf{K}}_{\mathbf{T}})_{13} = (\Delta \overline{\mathbf{K}}_{\mathbf{T}})_{14} = (\Delta \overline{\mathbf{K}}_{\mathbf{T}})_{24} = (\Delta \overline{\mathbf{K}}_{\mathbf{T}})_{31} = (\Delta \overline{\mathbf{K}}_{\mathbf{T}})_{41} = (\Delta \overline{\mathbf{K}}_{\mathbf{T}})_{42} = 0$$

Identifying the $\Delta \overline{\mathbf{K}}_{\mathbf{T}}$ term enables the structure's condition including any plastic/permanent deformation to be directly monitored.

To determine $\Delta \overline{\mathbf{K}}_{\mathbf{T}}$ using adaptive LMS methods, a new form of $\Delta \overline{\mathbf{K}}_{\mathbf{T}}$ is defined with time-varying scalar parameters $\hat{\alpha}_i$, to be identified using the LMS filter based on (Chase et al. 2005a; Chase et al. 2005b; Chase et al. 2005c). For a 4-DOF four-story example shear building, $\Delta \overline{\mathbf{K}}_{\mathbf{T}}$ can be sub-divided into four matrices to allow independent identification of changes in the linear elastic stiffness component of each story i.e. $(\Delta k_0)_1$, $(\Delta k_0)_2$, $(\Delta k_0)_3$, and $(\Delta k_0)_4$:

$$\Delta \overline{\mathbf{K}}_{\mathbf{T}} = \hat{\alpha}_1 \mathbf{K}_1 + \hat{\alpha}_2 \mathbf{K}_2 + \hat{\alpha}_3 \mathbf{K}_3 + \hat{\alpha}_4 \mathbf{K}_4 \tag{2.6}$$

where,

$$\mathbf{K}_1 = \begin{bmatrix} \alpha_1 + (1-\alpha_1)Y_1 \frac{\Delta \overline{z}_1}{\Delta \overline{v}_1} & 0 & 0 & 0 \\ 0 & 0 & 0 & 0 \\ 0 & 0 & 0 & 0 \\ 0 & 0 & 0 & 0 \end{bmatrix} \tag{2.7}$$

$$\mathbf{K_2} = \begin{bmatrix} \alpha_2 & -[\alpha_2 + (1-\alpha_2)Y_2 \dfrac{\Delta \bar{z}_2}{\Delta \bar{v}_2}] & 0 & 0 \\ -\alpha_2 & \alpha_2 + (1-\alpha_2)Y_2 \dfrac{\Delta \bar{z}_2}{\Delta \bar{v}_2} & 0 & 0 \\ 0 & 0 & 0 & 0 \\ 0 & 0 & 0 & 0 \end{bmatrix} \qquad (2.8)$$

$$\mathbf{K_3} = \begin{bmatrix} 0 & 0 & 0 & 0 \\ 0 & \alpha_3 & -[\alpha_3 + (1-\alpha_3)Y_3 \dfrac{\Delta \bar{z}_3}{\Delta \bar{v}_3} & 0 \\ 0 & -\alpha_3 & \alpha_3 + (1-\alpha_3)Y_3 \dfrac{\Delta \bar{z}_3}{\Delta \bar{v}_3} & 0 \\ 0 & 0 & 0 & 0 \end{bmatrix} \qquad (2.9)$$

$$\mathbf{K_4} = \begin{bmatrix} 0 & 0 & 0 & 0 \\ 0 & 0 & 0 & 0 \\ 0 & 0 & \alpha_4 & -[\alpha_4 + (1-\alpha_4)Y_4 \dfrac{\Delta \bar{z}_4}{\Delta \bar{v}_4}] \\ 0 & 0 & -\alpha_4 & \alpha_4 + (1-\alpha_4)Y_4 \dfrac{\Delta \bar{z}_4}{\Delta \bar{v}_4} \end{bmatrix} \qquad (2.10)$$

and

$$\hat{\alpha}_1 = (\Delta k_0)_1, \hat{\alpha}_2 = (\Delta k_0)_2, \hat{\alpha}_3 = (\Delta k_0)_3, \hat{\alpha}_4 = (\Delta k_0)_4 \qquad (2.11)$$

Hence, Equations (2.6)-(2.11) can be summarised:

$$\Delta \bar{\mathbf{K}}_\mathbf{T} = \sum_{i=1}^{n} \hat{\alpha}_i \mathbf{K_i} \qquad (2.12)$$

where n is the number of degrees of freedom of the model, and $\mathbf{K_i}$ is the corresponding time-varying matrix to i^{th} DOF in Equations (2.6)-(2.10). Rewriting Equation (2.4) using Equations (2.6)-(2.12) yields:

$$\sum_{i=1}^{n} \hat{\alpha}_i \mathbf{K_i} \cdot \{\Delta \bar{v}\} = -\underline{\mathbf{M}} \cdot \Delta \ddot{x}_g - \mathbf{M} \cdot \{\Delta \ddot{\bar{v}}\} - \mathbf{C} \cdot \{\Delta \dot{\bar{v}}\} - \bar{\mathbf{K}}_\mathbf{T} \cdot \{\Delta \bar{v}\} \qquad (2.13)$$

where $\{\Delta \ddot{\bar{v}}\}$, $\{\Delta \dot{\bar{v}}\}$, and $\{\Delta \bar{v}\}$ are measured, and $\bar{\mathbf{K}}_\mathbf{T}$ at each time step is calculated using Equations (2.2) and (2.3). To this end, the $Y_i \Delta \bar{z}_i$ term in $\bar{\mathbf{K}}_\mathbf{T}$ and the $\mathbf{K_i}$ matrices can be re-defined by introducing a hysteretic displacement, h_i, for each storey defined:

$$h_i = Y_i z_i, i = 1, ..., N \qquad (2.14)$$

where Y_i and z_i are the yield displacement and the hysteretic component of the ith storey,

30

respectively. Therefore, Equation (2.3) can be rewritten:

$$\dot{h}_i(t) = \dot{r}_i(t)\left\{ A_i - \beta_i \frac{|\dot{r}_i(t)|}{\dot{r}_i(t)}\left|\frac{h_i(t)}{Y_i}\right|^{n_i-1}\frac{h_i(t)}{Y_i} - \gamma_i\left|\frac{h_i(t)}{Y_i}\right|^{n_i}\right\}, i = 1,...,N \tag{2.15}$$

Equation (2.15) is equivalent to:

$$\dot{h}_i(t) = \dot{r}_i(t)\left\{ A_i - \left|\frac{h_i(t)}{Y_i}\right|^{n_i}\left(\beta_i \frac{|\dot{r}_i(t)|}{\dot{r}_i(t)}\frac{h_i(t)}{|h_i(t)|} + \gamma_i\right)\right\}, i = 1,...,N \tag{2.16}$$

where,

$$\frac{|\dot{r}_i(t)|}{\dot{r}_i(t)}\frac{h_i(t)}{|h_i(t)|} = sign\left(\dot{r}_i(t)h_i(t)\right), i = 1,...,N \tag{2.17}$$

yielding,

$$\dot{h}_i(t) = \dot{r}_i(t)\left\{ A_i - \left|\frac{h_i(t)}{Y_i}\right|^{n_i}\left(\beta_i sign\left(\dot{r}_i(t)h_i(t)\right) + \gamma_i\right)\right\}, i = 1,...,N \tag{2.18}$$

Using Equation (2.18) and assuming $\dot{h}_i$ is constant over the small interval (Δt) for each time step, the changes in hysteretic displacement of storey i over each time step, $\Delta h_i = Y_i \Delta z_i$, are defined:

$$h_i(t+\Delta t) - h_i(t) = \dot{r}_i(t)\left\{ A_i - \left|\frac{h_i(t)}{Y_i}\right|^{n_i}\left(\beta_i sign\left(\dot{r}_i(t)h_i(t)\right) + \gamma_i\right)\right\}\Delta t$$

$$i = 1,...,N \tag{2.19}$$

Therefore, $\Delta\bar{h}_i = Y_i\Delta\bar{z}_i$, changes in damaged hysteretic displacement of ith storey over each time step, can be determined from Equation (2.19) using measured or estimated damaged structural responses, $\{\Delta\ddot{\bar{v}}\}$, $\{\Delta\dot{\bar{v}}\}$, and $\{\Delta\bar{v}\}$.

The damaged structure stiffness, or effective stiffness changes due to nonlinear behaviour, can then be determined by identifying the $\hat{\alpha}_i$ in Equation (2.13) at every time step using a LMS-filtering approach (Chase et al. 2005b):

$$\{y\}_k = \sum_{i=1}^{n}\hat{\alpha}_i \mathbf{K_i} \cdot \{\Delta\bar{v}\}_k = -\mathbf{M}\cdot(\Delta\ddot{x}_g)_k - \mathbf{M}\cdot\{\Delta\ddot{\bar{v}}\}_k - \mathbf{C}\cdot\{\Delta\dot{\bar{v}}\}_k - \mathbf{\bar{K}_T}\cdot\{\Delta\bar{v}\}_k \tag{2.20}$$

where $(\Delta \ddot{x}_g)_k$ is the change in the input ground acceleration over a given time step of k, and $\{\Delta \ddot{\overline{v}}\}_k$, $\{\Delta \dot{\overline{v}}\}_k$, and $\{\Delta \overline{v}\}_k$ are the measured changes in the acceleration, velocity, and displacement vectors of the damaged structure over the same time step, respectively. Matrices $\overline{\mathbf{K}}_{\mathbf{T}}$ and $\mathbf{K_i}$ are calculated sample-to-sample using Equations (2.2) and (2.7)-(2.10) with the measured damaged structural responses. The elements of the vector signal $\{y\}_k$ can be readily modelled in real-time using adaptive LMS filters to identify the coefficients $\hat{\alpha}_i$ reflecting changes in linear stiffness of each storey (Chase et al. 2005b).

2.3.   Plastic displacement

Plastic displacements can also be calculated using the Bouc-Wen model. As Figure 2.2 illustrates, the plastic displacement range of storey i relative to storey i-1 during a stable hysteresis loop, $\Delta(r_p)_i(t)$, can be written (Dowling 2007):

$$\Delta(r_p)_i(t) = \Delta r_i(t) - \Delta(r_e)_i(t) = \Delta r_i(t) - \frac{\Delta(F_r)_i(t)}{(k_0)_i}, i = 1,...,N \tag{2.21}$$
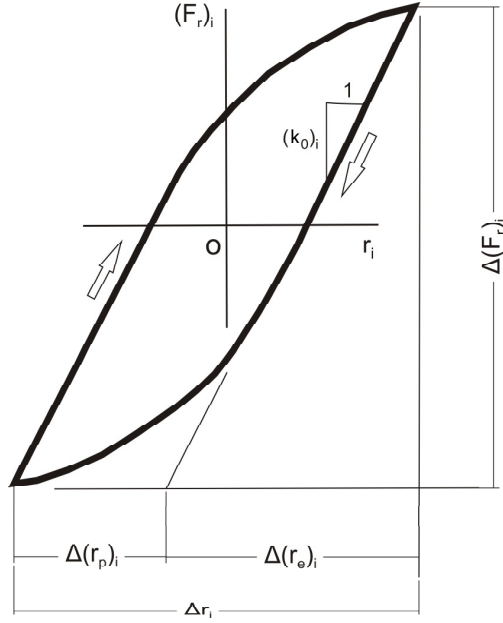
Figure 2.2. Stable force-displacement hysteresis loop

where, $\Delta r_i(t)$ and $\Delta(r_e)_i(t)$ are the total and elastic displacement ranges of storey i relative to storey i-1 during the same hysteresis loop, respectively. Moreover, $\Delta(F_r)_i(t)$ is the restoring force range of the loop, $(k_0)_i$ is the linear elastic stiffness of ith storey, and N is the degrees of freedom of the structure. $\Delta(F_r)_i(t)$ in Equation (2.21) can be written using the Bouc-Wen model (Constantinou and Tadjbakhsh 1985; Ma et al. 2006; Ismail et al. 2009):

$$\Delta(F_r)_i(t) = \alpha_i \frac{(F_y)_i}{Y_i} \Delta r_i(t) + (1 - \alpha_i)(k_0)_i \Delta h_i(t), i = 1,...,N \tag{2.22}$$

where $(F_y)_i$, Y_i, and α_i are the yield force, the yield displacement, and the bi-linear factor of storey i, respectively, and $\Delta h_i(t)$ is the hysteretic displacement change during the loop. Substituting $\Delta(F_r)_i(t)$ in Equation (2.21) with its equivalent from Equation (2.22) yields:

$$\Delta(r_p)_i(t) = \frac{\Delta r_i(t) - \Delta h_i(t)}{1 + \left(\dfrac{\alpha_i}{1 - \alpha_i}\right)}, i = 1,...,N \tag{2.23}$$

For structures with symmetric hysteresis loops with respect to tension and compression, this equation can be written using half of the ranges or amplitudes:

$$(r_p)_i(t) = \frac{r_i(t) - h_i(t)}{1 + \left(\dfrac{\alpha_i}{1 - \alpha_i}\right)}, i = 1, ..., N \tag{2.24}$$

Therefore, $(x_p)_i(t)$, the absolute plastic displacement of storey i can be calculated as sum of the relative plastic displacements of the first i stories:

$$(x_p)_i(t) = \sum_{i=1}^{i} (r_p)_i(t), i = 1, ..., N \tag{2.25}$$

$(x_p)_i(t)$ is the deflection of the structure if the elastic component of displacement were removed. It is a function of time, and is zero for an elastically responding structure. Importantly, permanent deflection is typically defined as the final plastic deflection. Plastic displacements over time along with material specific fatigue life curves thus provide greater information to assess damage and to evaluate the remaining life of the structure (Vayas et al. 2003; Dowling 2007; Nastar et al. 2010).

2.4. Adaptive LMS filtering theory

Adaptive filters are digital filters with coefficients that can change over time. The general idea is to update filter coefficients and assess how well the existing coefficients are performing in modelling a noisy signal, and then adapt the coefficient values to improve performance. The LMS algorithm is a widely used adaptive filtering technique and approximates the Steepest Descent Method using an estimator of the gradient (stochastic-gradient) instead of its actual value, considerably simplifying the calculations for real-time applications. In this case, the goal is to identify the individual scalar $\hat{\alpha}_i$ elements by modelling the signal $\{y\}_k$ of Equation (20) using the adaptive LMS filter.

In adaptive LMS filtering, as shown in Figure 2.3, the coefficients are adjusted from sample-to-sample to minimize the Mean Square Error (MSE) between a measured

scalar signal and its modelled value from the filter.
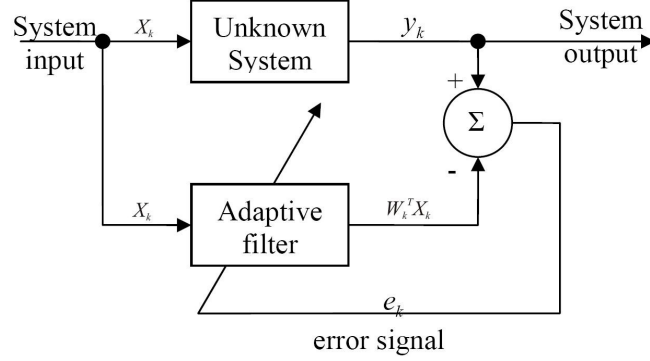
Figure 2.3. Adaptive LMS filtering process (Blome 2004)

$$e_k = y_k - W_k^T X_k = y_k - \sum_{i=o}^{m-1} w_k(i) x_{k-i} \tag{2.26}$$

where W_k is the adjustable filter coefficient vector or weight vector at time k, y_k is the measured scalar signal at time k, to be modelled or approximated, X_k is the input vector to the filter, model of current and previous filter inputs, x_{k-i}, so $W_k^T X_k$ is the vector dot product output from the filter at time k to model a scalar signal y_k, and m is the number of prior time steps or taps considered. The Widrow–Hopf LMS algorithm for updating the weights to minimize the error, e_k, is defined (Ifeachor and Jervis 1993):

$$W_{k+1} = W_k + 2\mu e_k X_k \tag{2.27}$$

where μ is a user-selected positive scalar, called step size, that controls the stability and rate of convergence. Several similar stochastic-gradient methods can be used to improve stability and convergence at different computational costs (Sayed 2003).

To identify $\Delta \overline{\mathbf{K}}_{\mathbf{T}}$ at time k, using LMS adaptive filters, the One-Step method (Chase et al. 2005b) and Equation (2.26) in matrix form can be used. Substituting $W_k^T X_k$ with its equivalent from Equation (2.20), yields:

$$\{e\}_k = \{y\}_k - \sum_{j=0}^{m-1} \sum_{i=1}^{n} \hat{\alpha}_{ij} \mathbf{K}_{\mathbf{i}} . \{\Delta \overline{v}\}_k \tag{2.28}$$

Minimizing the MSE with respect to $\hat{\alpha}_{ij}$ using Equation (2.27) yields the following

weight update formula for each coefficient in the weight matrix of the SHM problem:

$$w_{k+1} = w_k + 2\mu\{e\}_k^T \mathbf{K_i}.\{\Delta\bar{v}\}_{k-j} \tag{2.29}$$

Summing $\hat{\alpha}_{ij}$ over j filter taps, yields the $\hat{\alpha}_i$, change in stiffness of each story in Equation (2.20). The subscript k-j in Equation (2.29) represents the contribution of prior time step inputs in updating filter weights.

2.5.   Identification of the Bouc-Wen parameters

To identify the Bouc-Wen parameters for any given structure, a two-step procedure is presented. First, based on limited *a priori* knowledge of the structure, such as mass, geometrical properties, and material specifications, push-over finite element analysis (FEA) is done to obtain estimates of α_i, Y_i, and $(F_y)_i$, the bi-linear factor, the yield displacement, and the yield force of stories, respectively. Estimations of two other structural parameters, linear damping ratio and n_i, the power factor of each storey, are also assumed to be available from the basic knowledge of the structure. The second step, which can be done off-line or on-line as an event occurs, yields the basic Bouc-Wen hysteresis loop parameters (A_i, β_i, and γ_i).

To identify the basic loop parameters, Equation (2.19) can be written:

$$\beta_i sign\left(\dot{r}_i(t)h_i(t)\right) + \gamma_i - A_i\left|\frac{h_i(t)}{Y_i}\right|^{-n_i} = \frac{h_i(t)-h_i(t+\Delta t)}{\dot{r}_i(t)\Delta t}\left|\frac{h_i(t)}{Y_i}\right|^{-n_i}, i=1,...,N \tag{2.30}$$

Therefore,

$$\begin{cases} \gamma_i + \beta_i + A_iQ(t) = P(t) & \dot{r}_i(t)h_i(t) > 0 \\ \gamma_i + A_iQ(t) = P(t) & \dot{r}_i(t)h_i(t) = 0 \\ \gamma_i - \beta_i + A_iQ(t) = P(t) & \dot{r}_i(t)h_i(t) < 0 \end{cases} \tag{2.31}$$

where,

$$P(t) = \frac{h_i(t)-h_i(t+\Delta t)}{\dot{r}_i(t)\Delta t}\left|\frac{h_i(t)}{Y_i}\right|^{-n_i} \tag{2.32}$$

$$Q(t) = - \left| \frac{h_i(t)}{Y_i} \right|^{-n_i} \tag{2.33}$$

In Equations (2.31)-(2.33), $\dot{r}_i(t)$, relative velocity between stories i and i-1, is calculated using measured velocities of the stories, Y_i is known from the push-over analysis, and the hysteretic displacement, $h_i(t)$, is then calculated from Equation (2.34) assuming zero initial values for the hysteretic displacements (Baber and Wen 1981):

$$\begin{cases} \ddot{r}_i(t) - (1-\delta_{i1}) \dfrac{q_{i-1}}{m_{i-1}} + \dfrac{q_i}{m_i} \left[1 + (1-\delta_{i1}) \dfrac{m_i}{m_{i-1}} \right] - (1-\delta_{in}) \dfrac{q_{i+1}}{m_{i+1}} \left(\dfrac{m_{i+1}}{m_i} \right) = -\delta_{i1} \ddot{x}_g(t) \\[2ex] q_i(\dot{r}_i, r_i, h_i) = c_i \dot{r}_i(t) + \alpha_i \dfrac{(F_y)_i}{Y_i} r_i(t) + (1-\alpha_i) \dfrac{(F_y)_i}{Y_i} h_i(t) \\[2ex] i = 1, ..., N \end{cases} \tag{2.34}$$

where q_i is the nonlinear hysteretic restoring force, m_i is mass, c_i is the equivalent viscous damping, $(F_y)_i$ is the yield force, Y_i is the yield displacement, and α_i is the bi-linear factor, all for storey i. Finally, $r_i(t)$, $\dot{r}_i(t)$, and $\ddot{r}_i(t)$ are relative displacement, velocity, and acceleration between storeys i and i-1, respectively, $\ddot{x}_g(t)$ is the ground acceleration, and δ_{ij} is the Kronecker delta:

$$\delta_{ij} = \begin{cases} 1, i = j \\ 0, i \neq j \end{cases} \tag{2.35}$$

In Equation (2.34), all of the terms are either known or measured. Hence, it yields a set of independent equations for each storey. These equations can be solved for $h_i(t)$ sample-by-sample, in real time.

For the simpler case of a single-degree-of-freedom (SDOF) shear-type nonlinear hysteretic structure, the equation of motion is written:

$$m\ddot{v}(t) + c\dot{v}(t) + \alpha \frac{F_y}{Y} v(t) + (1-\alpha) \frac{F_y}{Y} h(t) = -m\ddot{x}_g \tag{2.36}$$

where $\ddot{v}(t)$, $\dot{v}(t)$, and $v(t)$ are acceleration, velocity, and displacement of the structure,

respectively, m is mass, and c is the equivalent viscous damping of the structure. F_y, Y, and α are again the yield force, the yield displacement, and the bi-linear factor of the structure. Using Equation (2.36), $h(t)$ for a SDOF structure can be written:

$$h(t) = \frac{Y}{(\alpha-1)F_y}\left[m\left(\ddot{x}_g + \ddot{v}(t)\right) + c\dot{v}(t)\right] + \left(\frac{\alpha}{\alpha-1}\right)v(t) \tag{2.37}$$

Therefore, Equations (2.31)-(2.33), using Equations (2.34) and (2.35), or in a SDOF case using (2.36) and (2.37), provide three independent equations that yield A_i, β_i, and γ_i in less than one hysteresis loop period. This time period is illustrated in Figure 2.4 for a SDOF hysteretic structure oscillating at 0.5 Hz (T_n=2.0 seconds) with unit amplitude. In this figure, points where the sign of $\dot{r}_i(t)h_i(t)$ changes are shown with black dots. As the figure shows, in one quarter of a loop period (0.5 seconds), the first three points provide enough independent equations to obtain the three unknown parameters.

In this chapter, the proposed two-step structural identification method is presented as an on-line technique to first identify the Bouc-Wen model parameters over the first hysteresis loop time of a structural response assuming no damage to the structure over this short period, comprising the initial small response cycle(s) before strong motion. The identified hysteretic parameters are then used for structural damage detection. One may also use this method as an off-line structural identification technique to obtain the Bouc-Wen parameters using available earthquake records prior to the damage detection in the current event. However, off-line identified models may not necessarily be exact for excitations apart from the excitation used for identification. This choice would thus impose an added error on the damage detection results when subsequently employed.
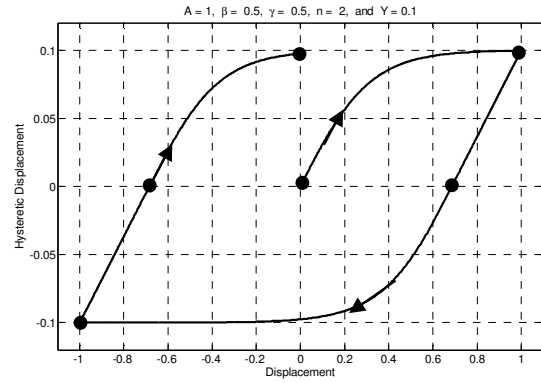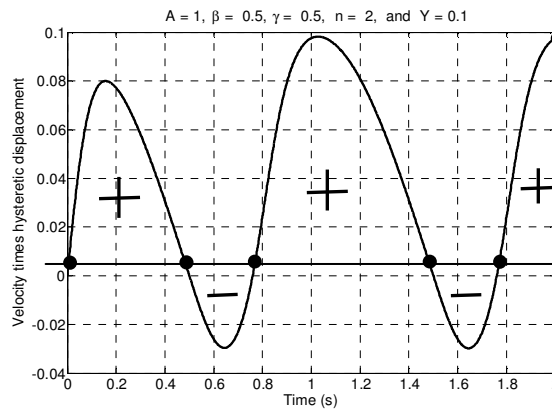
Figure 2.4. a) Hysteresis loop for one period of oscillation of a harmonic oscillator at 0.5 Hz (T_n=2.0 s) with unit amplitude, and b) velocity times hysteretic displacement for the same oscillator over the same period.

The proposed identification method is based on *a priori* knowledge from the structure. Therefore, limitations on the availability of the design data limit the use of the method. In such cases, there are number of more computationally-intensive off-line and on-line identification techniques that can be used. Examples of such methods are least squares (Yang and Lin 2004), Kalman filtering (Zhang et al. 2002), genetic algorithm (Ma et al. 2006), and bootstrap filtering technique (Li et al. 2004a).
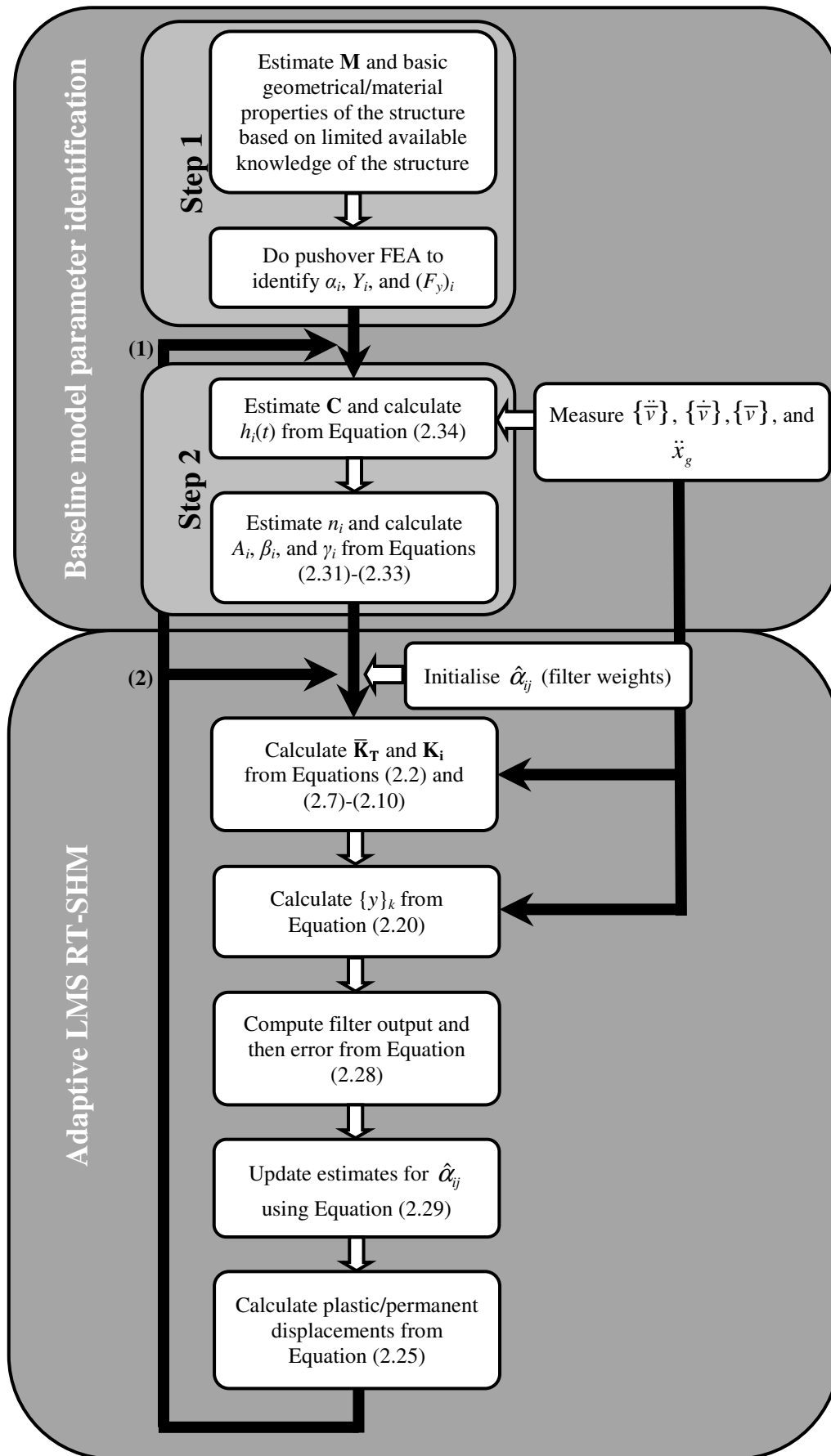
Figure 2.5. Flowchart of the overall adaptive LMS-based RT-SHM developed including the nonlinear baseline model identification. Path 2 is followed when the baseline model is identified off-line.

Overall computational procedure of the adaptive LMS-based RT-SHM, including the nonlinear Bouc-Wen baseline model parameter identification, developed in Sections 2.2 to 2.5 is summarised in Figure 2.5.

2.6. Inputs to the SHM problem

Inputs to this SHM problem are measured structural responses: acceleration, velocity, and displacement. Acceleration can be easily measured with low cost accelerometers at high sampling rates. Due to practical constraints, direct, especially high sampling rate measurement of displacement and velocity is not typically possible. Estimation by integration of measured accelerations is subject to correctable drift and error (Li et al. 2004b; Hann et al. 2009), and other estimations are available. Emerging high speed displacement sensors allow more precise estimation of the velocity at minimal added computational cost and enable this approach (Nayyerloo et al. 2010). Line-scan displacement measurement method, as one such emerging approach, will be explored later in this thesis in Chapters 6 and 7. Hence, all necessary measurements can be assumed available, or readily estimated.

2.7. Simulation proof-of-concept structure

The simulated proof-of-concept structure is a SDOF moment-resisting frame model of a five-story concrete building, chosen for both realism and simplicity. The plan view of a typical floor of the building is shown in Figure 2.6. The floor system consists of 200-series precast hollow-core floor units having a 65-mm topping spanning on long direction of each floor. The seismic weight per floor is 1692 kN for roof level and 2067 kN for other levels. Each storey has 3.8 m height, and the frame system is designed according to the New Zealand Concrete Structures Standard (NZS 3101 2006)

using the displacement-based design approach to sustain a target drift level of 2% under a 500-year return period earthquake.

(a)

(b)
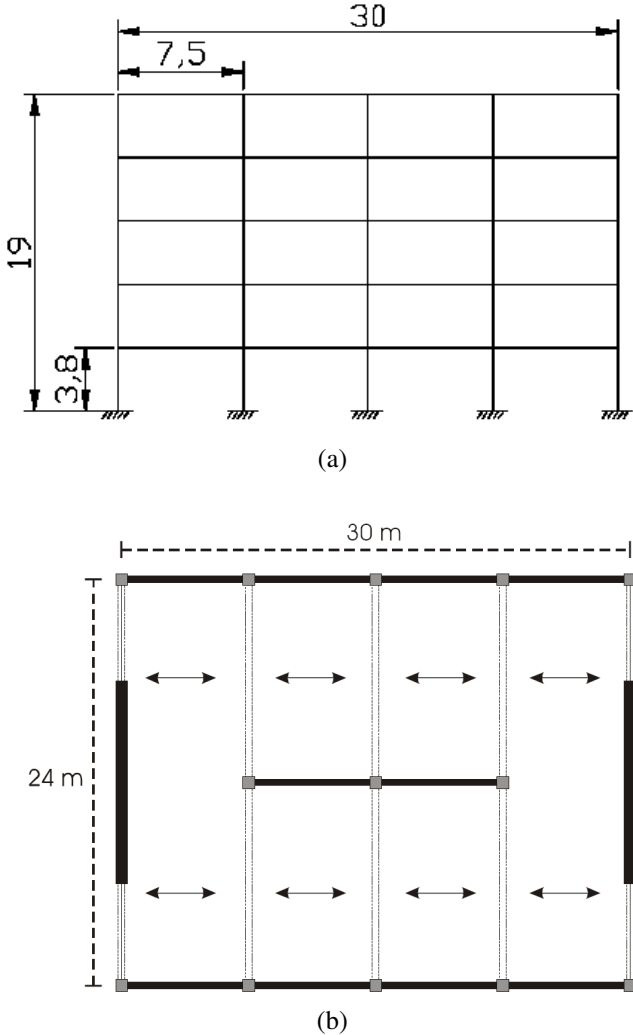
Figure 2.6. The simulated five-storey shear-type concrete building, (a) front view and (b) plan view

The proposed two-step structural identification method of Figure 2.5 is implemented to identify the Bouc-Wen hysteretic model parameters. To simulate structural responses to be used for the identification, $A=1$ and $\beta=\gamma=0.5$ are used, and the structure is subjected to the El Centro earthquake (EQ19 in Table 2-1). Nonlinear dynamic analysis is performed in MATLAB® using the identified parameters to represent the nonlinear hysteretic behaviour of the structure. The simulated structural responses from MATLAB® are used to provide proof-of-concept data and quantify the accuracy of the identified parameters, changes in linear elastic stiffness of each storey,

plastic and permanent displacements.

In simulating the structural responses, 5% constant viscous damping is considered, and the building was given an abruptness or power factor of $n=2$ to provide realistic nonlinear structural behaviour. Further, noise on the structural responses is assumed to be filtered prior to the identification process.

The developed SHM algorithm is implemented in MATLAB® for the stiffness identification process. Identified values were used to recalculate structural responses using the Newmark-β integration method to assess accuracy. The simulated structure was subjected to the Cape Mendocino record with peak ground acceleration (PGA) of 0.23 g, with a 10% reduction in pre-yield stiffness applied to the structure at the 10 second mark to simulate sudden damage (10% change in k_0 in Figure 2.1), and simulation-derived data is recorded at 500 Hz.

Next, to assess the robustness of the proposed method over different ground motions, the simulated structure was subjected to a suite of 20 different ground motions shown in Table 2-1. The same identified hysteretic parameters were used for all of the records, and a 5% reduction in pre-yield stiffness was applied to the structure at the 10 second mark (5% change in k_0 in Figure 2.1). This small amount of damage is chosen to show the capability of the proposed algorithm in capturing small, more likely levels of damage. The adaptive identification process was performed with a fixed filter tuning parameter or step size (μ) for all of the records in Table 2-1. This factor determines the speed of convergence. Simulation-derived data is again recorded at 500 Hz.

More details about the selected records can be found in (Christopoulos et al. 2002). This suite has been selected since it has been widely used for structural dynamic analyses in different studies and is a very popular suite among earthquake engineers.

Table 2-1. Selected ground motions (Christopoulos et al. 2002)

EQ	Event	Year	Station	R-Distance (km)	Soil Type	Duration (s)	Scaling Factor	PGA (g)
EQ1	Cape Mendocino	1992	Fortuna - Fortuna Blvd.	23.6	B	44.0	3.8	0.116
EQ2			Rio Dell Overpass - FF	18.5	B	36.0	1.2	0.385
EQ3	Landers	1992	Desert Hot Springs	23.2	B	50.0	2.7	0.171
EQ4			Yermo Fire Station	24.9	C	44.0	2.2	0.245
EQ5			Capitola	14.5	C	40.0	0.9	0.48
EQ6			Gilroy Array #3	14.4	C	39.0	0.7	0.367
EQ7	Loma Prieta	1989	Gilroy Array #4	16.1	C	40.0	1.3	0.417
EQ8			Gilroy Array #7	24.2	C	40.0	2.0	0.323
EQ9			Hollister Diff. Array	25.8	-	39.6	1.3	0.269
EQ10			Anderson Dam	21.4	B	40.0	1.4	0.244
EQ11			Beverly Hills 14145 Mulhol	20.8	B	30.0	0.9	0.617
EQ12			Canoga Park - Topanga Can	15.8	C	25.0	1.2	0.42
EQ13			Glendale - Las Palmas	25.4	C	30.0	1.1	0.357
EQ14	Northridge	1994	LA - Hollywood Stor FF	25.5	C	40.0	1.9	0.358
EQ15			LA - N Faring Rd	23.9	C	30.0	2.2	0.242
EQ16			N. Hollywood - Coldwater	14.6	B	21.9	1.7	0.298
EQ17			Sunland - Mt Gleason Ave.	17.7	B	30.0	2.2	0.157
EQ18			Brawley	18.2	C	22.0	2.7	0.116
EQ19	Superstition Hills	1987	El Centro Imp. Co. Cent.	13.9	C	40.0	1.9	0.358
EQ20			Plaster City.	21.0	C	22.2	2.2	0.186

2.8.   Results

2.8.1. Hysteretic model parameter identification results

Figure 2.7 shows the push-over analysis results for the proof-of-concept structure from Ruaumoko (Carr 2004). It shows the total yield force (1269.45 kN), the bi-linear factor (0.065), and the yield displacement (46.5 mm) of the structure. These parameters are used for the second step of the identification process to identify A, β, and γ, the basic hysteresis loop parameters of the proof-of-concept structure. Figure 2.8 shows that the hysteretic parameters (A, β, and γ) can be identified in less than a quarter of the natural period of the structure (0.3 seconds in this case).
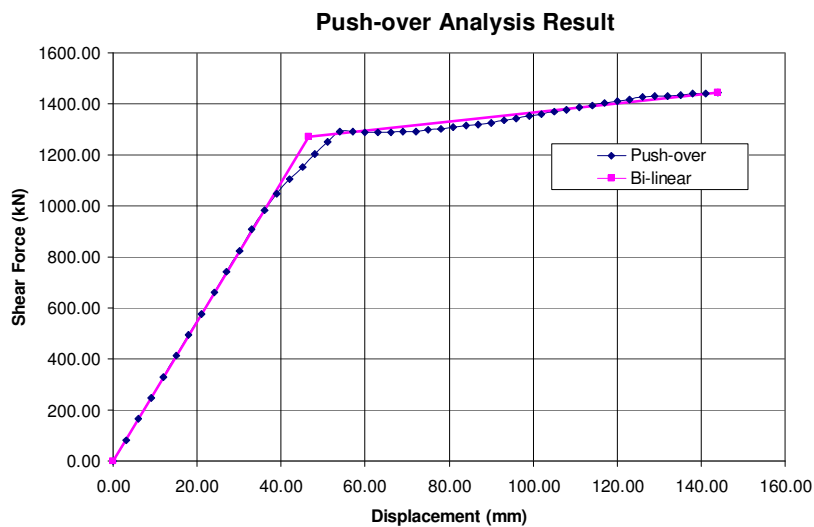
Figure 2.7. Push-over analysis results of the simulated building using the Ruaumoko finite element code
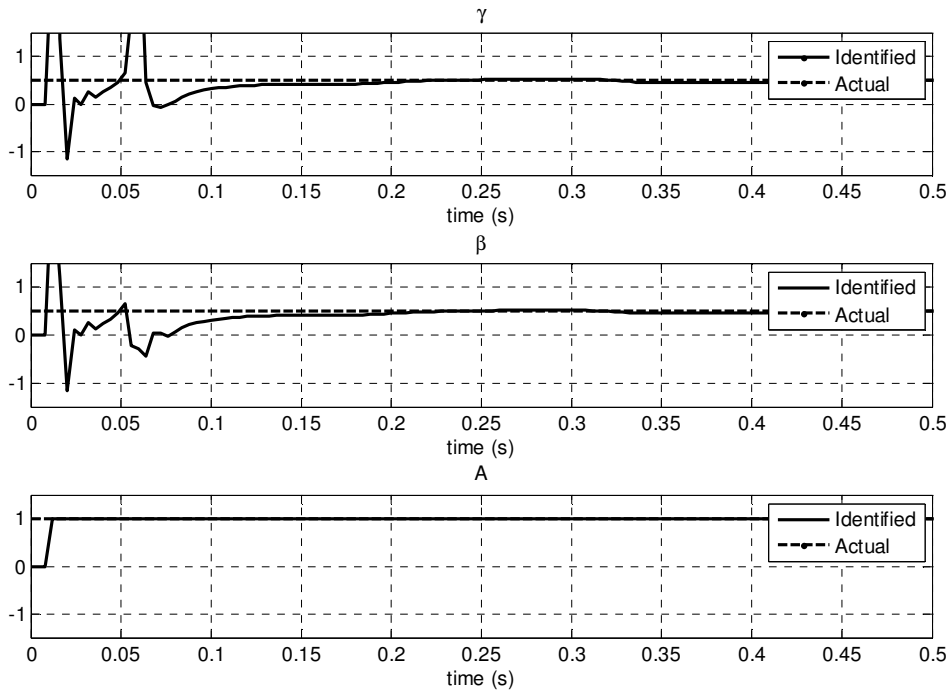
Figure 2.8. Identified hysteretic parameters for the simulated case-study structure subjected to the El Centro earthquake

2.8.2. Damage identification results

Figure 2.9 shows responses of the SDOF proof-of-concept structure with a 10% reduction in the linear elastic stiffness at the 10 second mark for the Cape Mendocino earthquake. As shown in Figure 2.10, in a worst-case, sudden failure situation, Δk_0, changes in the pre-yield linear elastic stiffness of the structure, converge to within 10% of the actual change in less than 2 seconds using 10 filter taps at a 500 Hz sampling rate. Moreover, Figure 2.11 shows that the LMS filter approaches faster and smoother to the final values of the pre-yield stiffness changes (damage) when higher sampling rates or a greater number of taps (or prior time steps) are used.
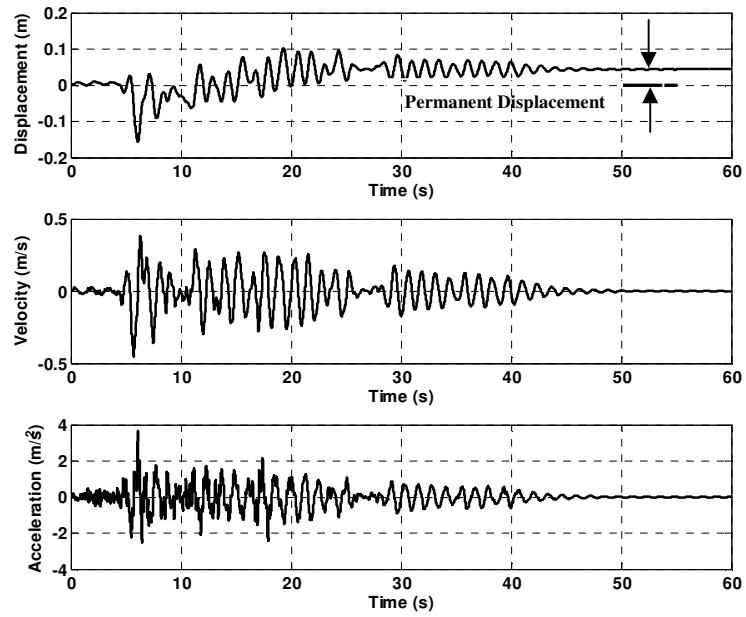
Figure 2.9. Responses of the simulated structure subjected to the Cape Mendocino earthquake and 10% sudden failure at the 10 second mark
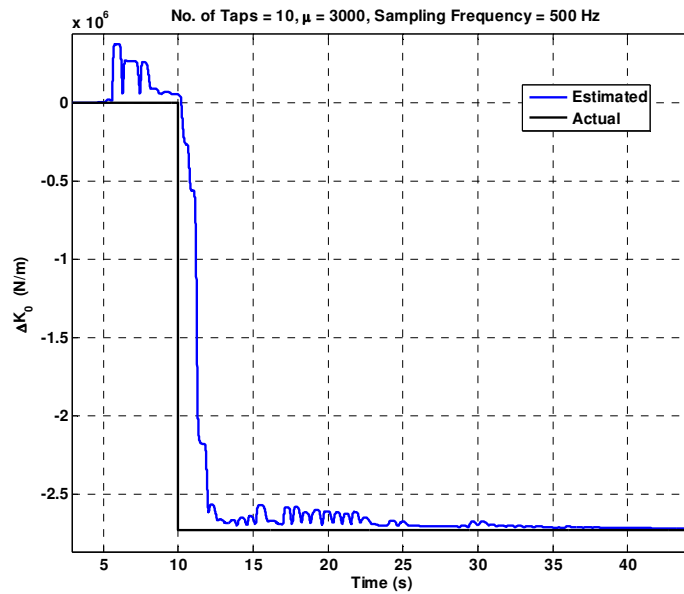
Figure 2.10. Identified changes in the pre-yield stiffness of the simulated structure, with 10% sudden failure at the 10 second mark, using the adaptive LMS algorithm

47
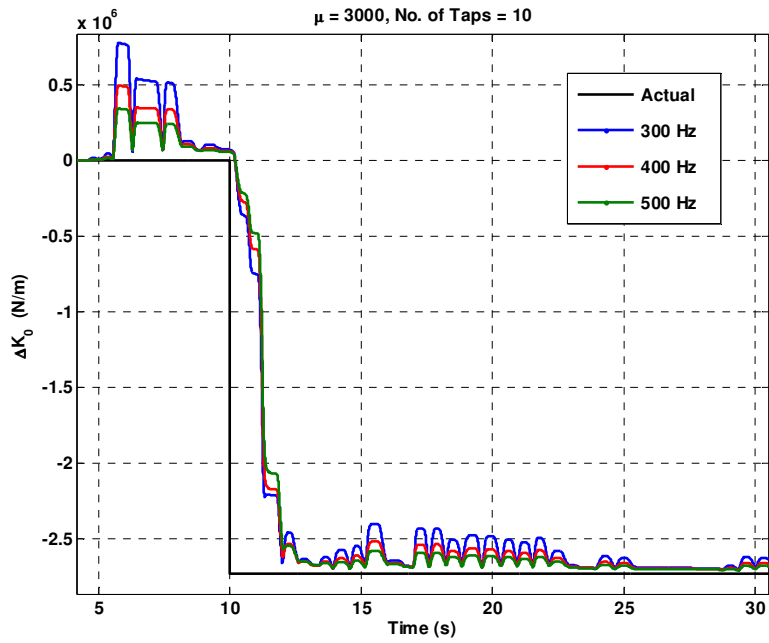
(a)
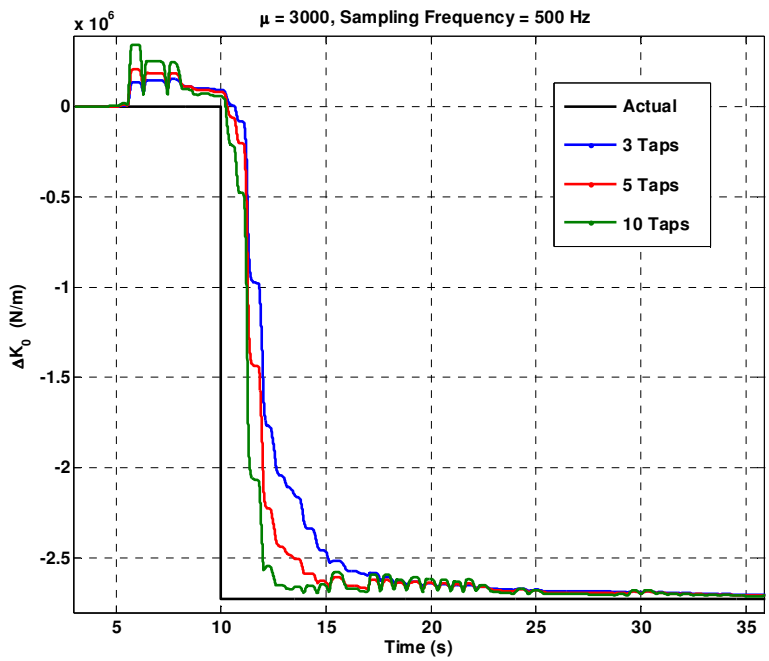
(b)

Figure 2.11. Identified changes in the pre-yield stiffness of the simulated structure, with 10% sudden failure at the 10 second mark, using the adaptive LMS algorithm, (a) at different sampling rates and (b) with different tap numbers

Figure 2.12 shows the nonlinear structure's re-simulation results using Equation (2.20) and the Newmark-β integration method with the identified values for the

hysteretic parameters and changes in stiffness (Δk_0). This figure clearly shows that as the sudden change occurs, plastic deflection begins in this case. The model then tracks the initial sampled behaviour accurately. For the entire record, the ratio between the norm of the error signal in estimating the plastic deflections and the norm of the actual plastic deflection signal is less than 2.5%, and error in identifying the permanent deflection is less than 0.5% of the actual value.

No. of Taps = 10, μ = 3000, Sampling Frequency = 500 Hz

(a)

Sudden Failure

No. of Taps = 10, μ = 3000, Sampling Frequency = 500 Hz

(b)
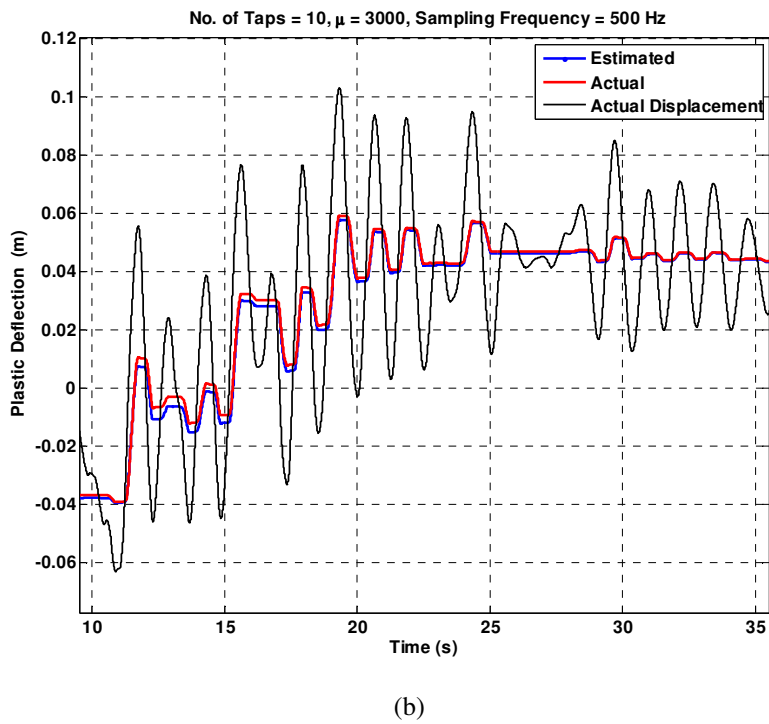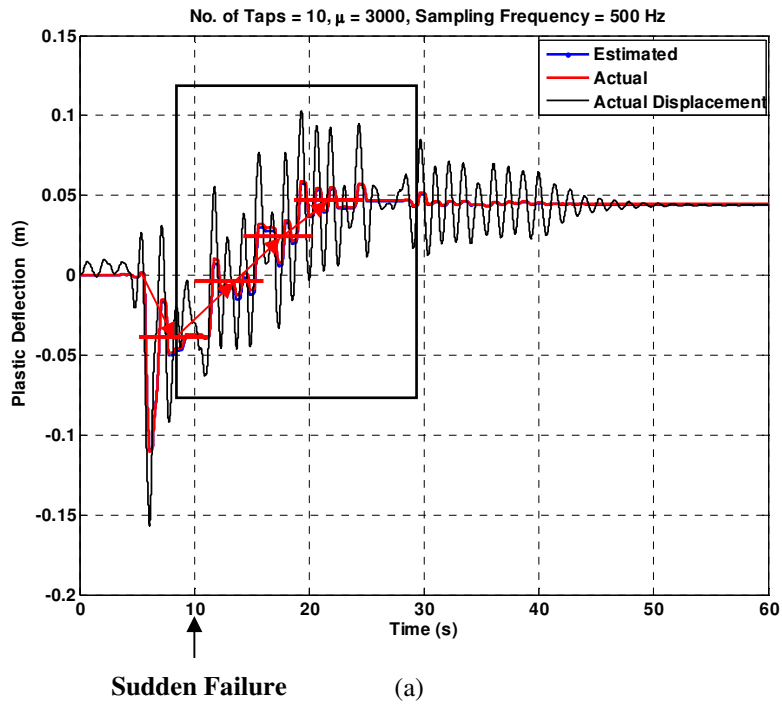
Figure 2.12. Identified plastic displacements of the simulated structure, with 10% sudden failure at the time of 10 second mark, using the estimated changes in the pre-yield stiffness. The box in panel (a) shows the area highlighted in panel (b).

2.8.3. Effect of external loads on damage identification results

Figure 2.13 shows, in a worst-case sudden failure situation, Δk_0 converges to within 10% of the actual value in less than 2 seconds using a fixed step size and 10 taps at a 500 Hz sampling rate under all 20 different excitations in Table 2-1. Once more, re-simulating the structural responses with the identified values shows that as the filter converges, the plastic deflection approaches its actual value, and the errors between the actual and estimated values for plastic deflections become smaller.

For the suite used in this study, Figures 2.14 and 2.15 show the ratio between norms of the error signals in estimating the plastic deflections and norms of the actual plastic deflection signals is less than 12%, and the error in identifying permanent deflections is less than 15% of the actual value over the entire records. Records that caused permanent deflections less than 0.1% of the height of the case-study structure were excluded from the error summary and set to zero due to their very small size and insignificance.
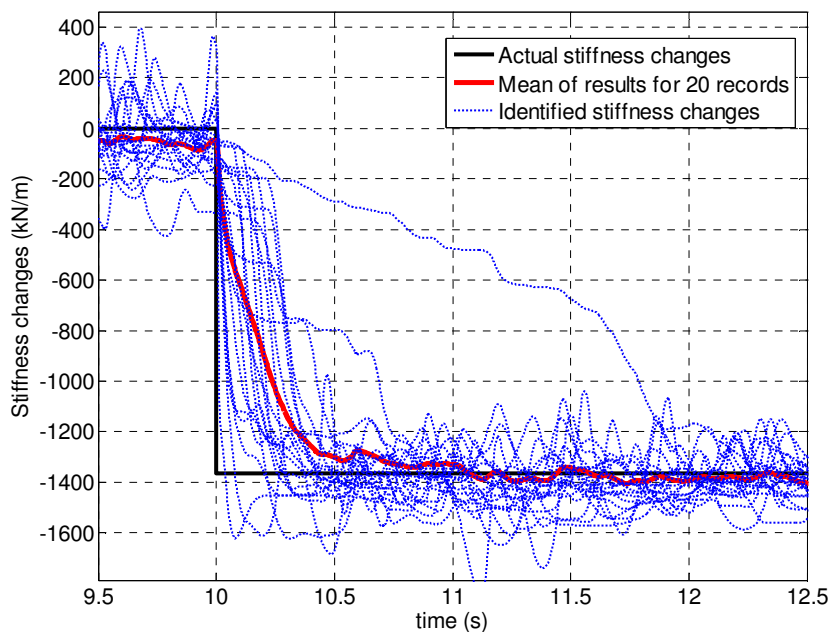
Figure 2.13. Identified changes in the linear elastic stiffness of the simulated structure
(10 taps with μ=25,000)
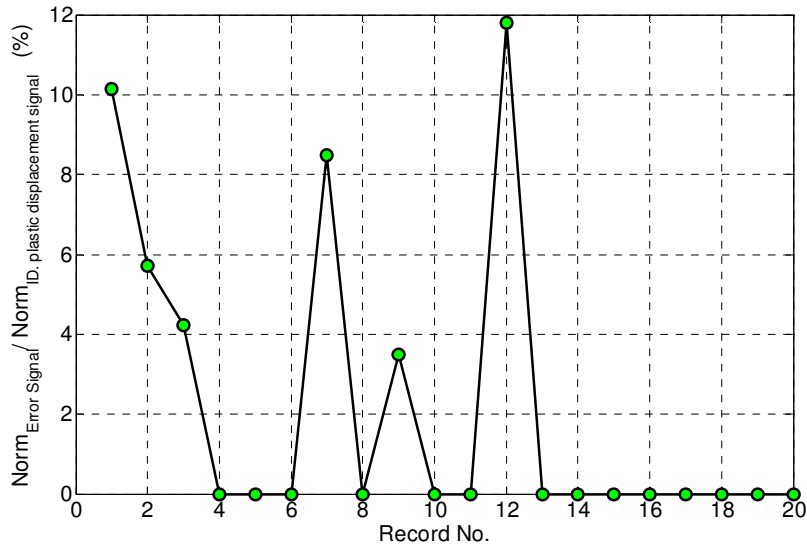
Figure 2.14. Changes in the ratio of norm of the error in identifying plastic deflections and norm of the plastic deflection signal for the 20 different records in Table 2-1 (Mean=7.31%, Median=7.1%, and *IQR*=5.93%)
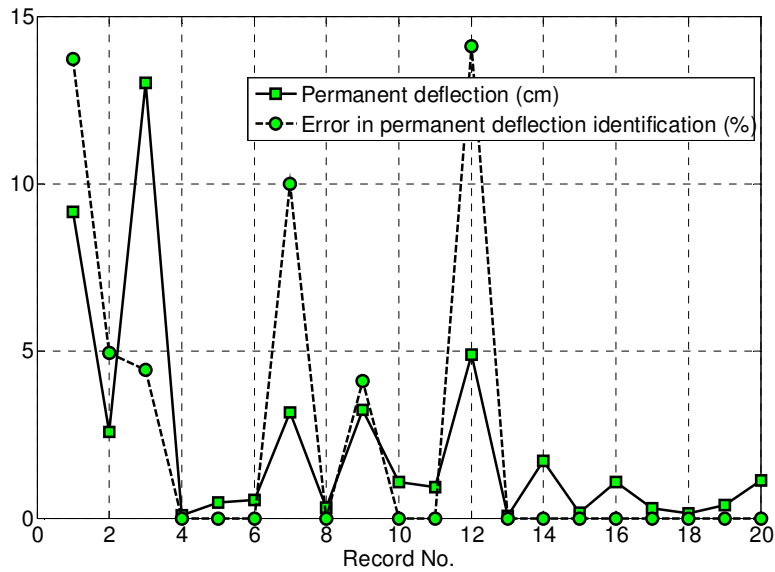
Figure 2.15. Identified permanent deflection and permanent deflection identification error for the 20 different records in Table 2-1 (Mean error=8.54%, Median error=7.46%, and *IQR* = 9.3%)

Figures 2.13-2.15 show that performance of the proposed SHM algorithm in identifying changes in stiffness and plastic or permanent deflections changes for different ground excitations. Thus, for fixed filter tuning parameters in the LMS algorithm, some cases result in fairly large errors, as high as 14% in identified

permanent deflection. This problem can be solved to some extent by implementing a variable step size or self-tuning LMS-based filtering algorithm initially tuned based on past earthquake records and capable of self-tuning to external load changes for the best identification results. Different methods with variable step size can be found in the adaptive filtering literature to improve the identification results (Sayed 2003; Abadi and Far 2008; Costa and Bermudez 2008). However, most of the results here are less than 5%, and even the largest errors are broadly acceptable.

It is worth mentioning that the accuracy of any model-based SHM algorithm relies directly on the correctness and thoroughness of its baseline model, which is the Bouc-Wen model in this case. Therefore, using a more comprehensive baseline model and having more precise estimation of the baseline model parameters would yield more accurate results. These analyses were not included in this thesis, but present a future avenue of research that can be pursued with similar derivation and generalised approach.

2.9.   Summary

SHM algorithms based on adaptive LMS filtering theory can directly identify time-varying changes in structural stiffness in real-time in a computationally efficient fashion. However, better metrics of seismic structural damage and future utility after an event are related to permanent and plastic deformations. This chapter presented a modified LMS-based SHM method and a novel two-step structural identification technique using a baseline nonlinear Bouc-Wen structural model to directly identify changes in stiffness due to damage, as well as plastic and permanent deflections. The algorithm designed is computationally efficient; therefore it can work in real-time.

An *in silico* SDOF nonlinear shear-type structure was used to prove the concept.

The efficiency of the proposed SHM algorithm in identifying stiffness changes and plastic/permanent deflections was assessed under different ground motions using a suite of 20 different ground acceleration records. The results showed that in a realistic scenario with fixed filter tuning parameters, the proposed LMS-based SHM algorithm identifies stiffness changes to within 10% of true values within 2.0 seconds. Median ratio of the norm of error signal in identifying plastic deformations to the norm of actual as-modelled plastic deflection signal was shown to be 7.1% for the suite of records used. Further, permanent deformation was identified to within 7.46% of the actual value using noise-free simulation-derived structural responses. The two latter values provide important post-event information on the future serviceability, safety, and repair cost.

CHAPTER 3

RT-SHM using changes in internal dynamics: Application to base-isolation systems

3.1. Introduction

A novel adaptive LMS-based approach for RT-SHM of nonlinear hysteretic structures under seismic excitations was developed in the previous chapter. It was assumed that only a limited *a priori* knowledge of the structure is available to identify parameters of the nonlinear baseline model used in the SHM process. However, when more design data is available, such as in base-isolation systems, simpler and more suitable real-time techniques can be used.

Base-isolation is an increasingly applied structural seismic protection technique in highly seismic areas in the world. Martelli (2009) reports the number of seismically-isolated structures until October 2008 as over 10,000 structures in about 30 different countries. The range of applications is also very broad and covers both new and existing structures of almost all kinds, such as bridges and viaducts, buildings (private and public), important industrial installations, heritage structures, museum display cases, etc. (Martelli 2009).

Base-isolation systems decouple structures from the ground to protect structural integrity and contents from severe seismic excitations. They support the weight, damp the response and transfer of energy to the isolated structure, and restore the original position of the structure after an earthquake (Saito 2007). Sliding and elastomeric bearing systems are typically used for base-isolation (Narasimhan et al. 2006). These systems reduce the superstructure's response at the cost of an increase in the base displacements in near-fault motions.

The current practice is to use nonlinear passive dampers to limit bearing displacement. However, this approach increases the force at both the base and the isolation level (Narasimhan et al. 2006). Active and semi-active dampers, such as magneto-rheological (MR) dampers (Spencer and Nagarajaiah 2003), provide attractive alternatives to passive dampers by providing more flexibility, and control of the applied damping forces. The performance of the overall nonlinear hysteretic system at the isolation level, shown in Figure 3.1, directly affects the seismic behaviour of the superstructure above the isolation level. Therefore, the base-isolation system needs to be monitored for likely faults to reliably maintain and ensure superstructure integrity.
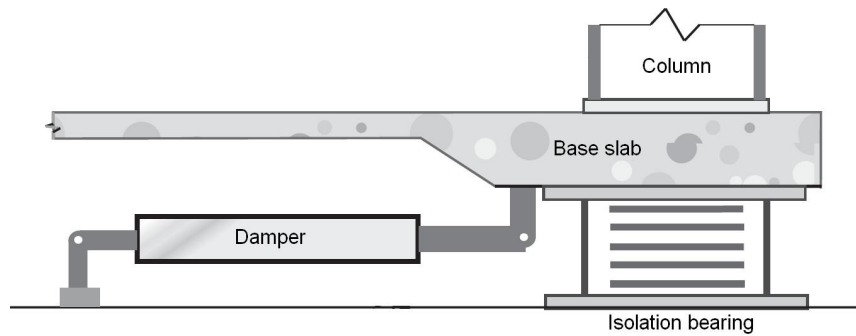
Figure 3.1. Base-isolation system (Narasimhan et al. 2006)

In nonlinear control theory, fault detection and diagnosis have attracted significant attention, particularly for highly sensitive systems where fault detection at the earliest stage is required (Patton 1997; Duan and Patton 1998; Edwards et al. 2000; Saif 2002; Liberatore et al. 2006; Mhaskar et al. 2008). The process of fault detection and diagnosis is often referred to as SHM in the mechanical, aerospace, and the civil engineering fields. Fault detection is typically done by means of a residual signal generated from available measurements (Besançon 2003). It must be a signal that is zero or near zero in the absence of faults and considerably affected when the system is undergoing faults to provide high resolution to the detection process (Kinnaert 1999; Besançon 2003; Liberatore et al. 2006). In addition, the residual signal has to return to its original no-fault state when the faults fade or one repaired away.

Different fault detection and diagnosis algorithms have been proposed in the literature, such as Duan and Patton (1998), Edwards et al. (2000), and Saif (2002), but they all come with significant complexity. This chapter develops a simple fault detection technique based on a comparison between the internal dynamics of the base-isolation system with a healthy baseline model's internal dynamics to detect likely faults. The residual signal is then used for fault quantification using PLLSQ fitting techniques (Hann et al. 2009). It is thus an extension in approach and application of the SHM methods in the previous chapter.

58

Different combinations of stiffness and damping faults are considered for proof-of-concept simulations on a passive second-order base-isolated system. The choice of passive system is only for simplicity. It is straightforward to generalize the method developed to active and semi-active base-isolation systems.

3.2.   SHM problem statement

A nonlinear, seismically excited base-isolation system with passive MR dampers, as shown in Figure 3.2, can be modelled (Constantinou and Tadjbakhsh 1985; Shen et al. 2005; Rodríguez et al. 2009; Tsouroukdissian et al. 2009):

$$m\ddot{v}(t) + c\dot{v}(t) + \alpha k v(t) + (1-\alpha) kYz(t) = -m\ddot{x}_g(t) \tag{3.1}$$
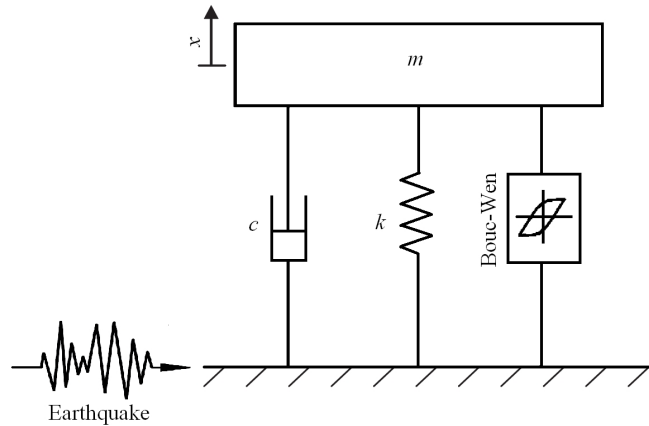
Figure 3.2. Model of a base-isolation system with passive MR dampers

where m, c, and k are the mass, damping, and the stiffness of the system, respectively, v, $\dot{v}$, and $\ddot{v}$ are displacement, velocity, and acceleration of the base-isolation system, respectively, $0 \leq \alpha \leq 1$ is the bi-linear factor defined as the post- to pre-yield stiffness ratio of the system, and $\ddot{x}_g$ is the ground motion acceleration. Moreover, $z(t)$ is the dimensionless Bouc-Wen hysteresis component governed by the following first-order differential equation from the so-called classical Bouc-Wen model, introduced in Section 2.2 and repeated here, in brief, for convenience (Bouc 1967; Wen 1976;

Constantinou and Tadjbakhsh 1985; Ikhouane and Rodellar 2007):

$$\dot{z}(t) = \frac{A\dot{v}(t) - \beta|\dot{v}(t)||z(t)|^{n-1}z(t) - \gamma\dot{v}(t)|z(t)|^{n}}{Y} \qquad (3.2)$$

$$A > 0, \beta > 0, -\beta < \gamma \le \beta, n \ge 1$$

where A, β, γ, and n are stiffness, loop fatness, loop pinching, and abruptness parameters in the classical Bouc-Wen model, respectively. Further, n, the power factor, determines the sharpness of the curve from elastic to plastic force-deflection behaviour of the system, and finally, Y is the yield displacement of the system. This model has been chosen only for simplicity, and more detailed models for MR dampers (Spencer et al. 1997) could also be used.

When a fault occurs in a base-isolation system, assuming the mass and the internal parameters of the damper remain unchanged (Choi et al. 2001), the equations of motion of the faulty or damaged system can be written:

$$m\ddot{\bar{v}}(t) + (c + \Delta c(t))\dot{\bar{v}}(t) + \alpha(k + \Delta k(t))\bar{v}(t) + (1 - \alpha)(k + \Delta k(t))Y\bar{z}(t) = -m\ddot{x}_g(t) \qquad (3.3)$$

where $\ddot{\bar{v}}$, $\dot{\bar{v}}$, and $\bar{v}$ are responses of the faulty system, and Δk and Δc respectively denote time-varying changes in the stiffness and damping of the system due to the fault. Further, $\bar{z}(t)$ is the hysteretic component of the faulty structure from Equation (3.2) using velocities of the faulty base-isolation system.

The problem is to design a fault or damage detection signal that is zero in the absence of fault and non-zero with amplitude relative to the severity of the fault when it occurs. Such signals are called residual signals in fault detection systems (Kinnaert 1999; Besançon 2003; Liberatore et al. 2006). In addition to fault detection, the designed residual signal should provide enough information for diagnosis of the fault detected, such as enabling the identification of time-varying Δk and Δc terms in Equation (3.3).

3.3. Residual signal design

The Bouc-Wen model used to represent the internal dynamics of base-isolation systems has only one state variable. Therefore, any change in the dynamic behaviour of the system will appear in this single state. This outcome suggests rearranging Equation (3.3) by introducing a new hysteretic component, $\bar{Z}(t)$, for the faulty or damaged system:

$$m\ddot{\bar{v}}(t)+c\dot{\bar{v}}(t)+\alpha k\bar{v}(t)+(1-\alpha)kY\bar{Z}(t)=-m\ddot{x}_g(t) \tag{3.4}$$

where,

$$\bar{Z}(t)=\left(1+\frac{\Delta k(t)}{k}\right)\bar{z}(t)+\frac{\alpha\Delta k(t)}{(1-\alpha)kY}\bar{v}(t)+\frac{\Delta c(t)}{(1-\alpha)kY}\dot{\bar{v}}(t) \tag{3.5}$$

A simple comparison between Equations (3.1) and (3.4) shows that these two equations are essentially the same except in the hysteretic component. Therefore, comparing the internal dynamics of the healthy and faulty systems by taking the difference between the hysteretic components reveals any likely changes (faults) in the system.

As Equation (3.5) shows, in the absence of a fault, $\Delta k=\Delta c=0$ and $\bar{Z}(t)=\bar{z}(t)$. Thus, $\bar{Z}(t)-\bar{z}(t)$ is zero in this case. When there is a fault in the system, $\bar{Z}(t)\neq\bar{z}(t)$ and the residual, $\bar{Z}(t)-\bar{z}(t)$, is non-zero. This difference can be used as an indication for the existence of stiffness or damping faults in the base-isolation system:

$$I(t)=\kappa_1\left(\bar{Z}(t)-\bar{z}(t)\right) \tag{3.6}$$

where $I(t)$ is the residual signal and $\kappa_1>0$ is a scaling factor.

Changes in the stiffness and damping of the system typically do not result in the same residual signals. Changes in the damping coefficient usually have much less effect on the structural responses and consequently on the designed residual signal. This difference in the effect of the two different types of fault, with same severity on the

base-isolation system, makes presentation of results for combined cases of fault difficult. Therefore, two more scaling factors, $\kappa_2, \kappa_3 > 0$, are introduced to overcome this problem, yielding:

$$I(t) = \frac{\kappa_1}{kY}\left[\kappa_2 \Delta k(t)\left(Y\overline{z}(t) + \frac{\alpha}{1-\alpha}\overline{v}(t)\right) + \frac{\kappa_3 \Delta c(t)}{(1-\alpha)}\dot{\overline{v}}(t)\right] \qquad (3.7)$$

where $I(t)$ is again the residual signal, and all other terms have been previously defined. The scaling factors, $\kappa_{1\text{-}3}$, can be determined empirically or by following the procedure outlined in Figure 3.3.

To calculate the residual signal in Equation (3.6), $\overline{Z}$ is calculated from Equation (3.4) using measured responses of the possibly faulty system and measured ground accelerations. The internal dynamics of the healthy system, $\overline{z}$, are estimated by calculating its first time derivative, $\dot{\overline{z}}$, from Equation (3.2) using measured velocities of the faulty structure and assuming zero initial state. All other terms in Equations (3.2) and (3.4), including the Bouc-Wen and structural parameters, are either measured or assumed to be known prior to fault detection to represent the healthy dynamics of the base-isolation system in the absence of damaging inputs. Thus, if the system is fault free, $\overline{Z} = \overline{z}$, and $I(t)$=0. Figure 3.4 summarises the fault detection procedure developed.

Initialise $\kappa_{1\text{-}3}$
($\kappa_1=\kappa_2=\kappa_3=1$)

Induce small amounts of damage in c (e.g. ±5%)

Calculate $I(t)$ from Equation (3.7) using $\overline{z}(t)$ estimated from Equation (3.2) and known system parameters

Simulate system responses of Equation (3.2)-(3.3)

Increase κ_3

No Are the changes detectable in $I(t)$?

Yes

Let $\Delta c=0$, and induce small amounts of damage in k (e.g. ±5%)

Calculate $I(t)$ from Equation (3.7) using $\overline{z}(t)$ estimated from Equation (3.2) and known system parameters

Increase κ_2

Decrease κ_2

Lower Is the order of $I(t)$ same as what it was for damage in c? **Higher**

Equal

Is the final order of $I(t)$ low? **Yes** Increase κ_1

No

Report $\kappa_{1\text{-}3}$

Figure 3.3. A simple procedure to determine the scaling factors, $\kappa_{1\text{-}3}$, used in the real-time fault detection and diagnosis method developed
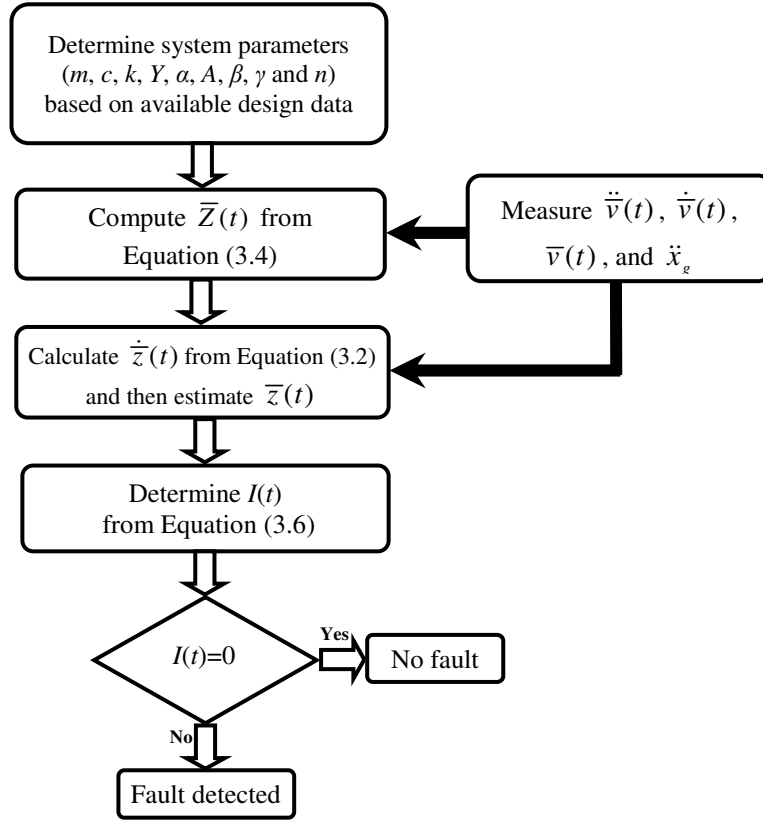
Figure 3.4. Flowchart of each time step in the fault detection method developed

3.4. Fault diagnosis

The aim of the diagnostic part is to determine the type and severity of likely faults detected by the residual signal in the base-isolation system. Quantifying detected faults, for instance in terms of initial stiffness and/or damping values of the system, is of great importance in structural health monitoring and provides the information required for structural control methods with damage avoidance or mitigation goals. Detected faults could be of stiffness type ($\Delta k \neq 0$), damping type ($\Delta c \neq 0$), or a combination of both ($\Delta k \neq 0$ and $\Delta c \neq 0$). Therefore, identifying Δk and Δc in Equation (3.7) determines the fault type, as well as its severity. To identify Δk and Δc in real-time, Equation (3.7) can be rewritten at each time step Δt_k:

$$I_k = \phi_{1,k}\Delta k_k + \phi_{2,k}\Delta c_k \tag{3.8}$$

and

$$\phi_{1,k} = \frac{\kappa_1 \kappa_2}{kY} \left(Y\overline{z}_k + \frac{\alpha}{1-\alpha} \overline{v}_k \right)$$

$$\phi_{2,k} = \frac{\kappa_1 \kappa_3}{kY(1-\alpha)} \dot{\overline{v}}_k$$

(3.9)

where the subscript k denotes values at time k. In Equation (3.9), $\dot{\overline{v}}_k$ and $\overline{v}_k$, are the measured responses of the faulty system at each time step, $\overline{z}_k$ is estimated from Equation (3.2) using measured velocities of the faulty system, κ_{1-3} are user selected scaling factors, and all other parameters are assumed to be *a priori* known. These parameters are mainly design parameters of the base-isolation system and are typically available before fault detection and diagnosis.

Thus, $\phi_{1,k}$ and $\phi_{2,k}$ can be readily calculated at each time step. Moreover, as mentioned earlier, $\overline{Z}_k$ is calculated from Equation (3.4) using measured responses of the faulty system, measured ground motion accelerations, and known parameters of the healthy system. Therefore, from Equation (3.6), I_k is known, and Equation (3.8) is a linear equation in terms of the unknowns (Δk_k and Δc_k) at each time step Δt_k and can be solved using PLLSQ estimation (Hann et al. 2009).

Without loss of generality, one of the two unknowns ($\Delta k(t)$ or $\Delta c(t)$) can be assumed to have a faster dynamics than the other and changes over smaller time steps over Δt_k:

$$\Delta k(t) = \Delta k_k, (k-1)\Delta t_k \le t \le k\Delta t_k, k = 1,...,m'$$

$$\Delta c(t) = \Delta c_l, \ (l-1)\Delta t_l \le t \le l\Delta t_l, \ l = 1,...,n'$$

$$\Delta t_k = p\Delta t_l, p > 1$$

(3.10)

where m' and n' are the number of intervals over which the piecewise time-varying functions, $\Delta c(t)$ and $\Delta k(t)$, are defined. Further, Δt_k and Δt_l are user-selected intervals over which piecewise constant behaviour is reasonable. For ease of fitting, p is assumed to be an integer value greater than one. In this way, p values of Δc_l are fitted alongside

every single value of Δk_k, as shown in Figure 3.5 for the case of $p=3$.
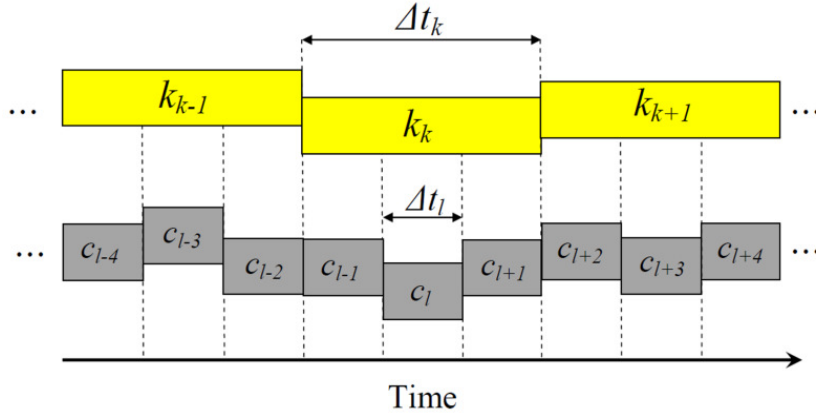
Figure 3.5. Time variation of the fitted parameters for $p=3$

Identification of the unknown parameters, Δk_k and Δc_l, requires a set of linear equations, each in the form of Equation (3.8). For the example of Figure 3.5, three values of Δt_i could be chosen in each time interval Δt_l $(p' = 3)$. Again for ease of fitting, p' is assumed to be an integer value greater than one. This choice will give nine equations $(p \times p')$ for each time interval Δt_k with four unknowns:

$$\mathbf{A_k} \cdot \{x\}_k = \{I\}_k \tag{3.11}$$

where

$$\mathbf{A_k} = \begin{bmatrix} \phi_{1,i} & \phi_{2,i} & 0 & 0 \\ \phi_{1,i-1} & \phi_{2,i-1} & 0 & 0 \\ \phi_{1,i-2} & \phi_{2,i-2} & 0 & 0 \\ \phi_{1,i-3} & 0 & \phi_{2,i-3} & 0 \\ \phi_{1,i-4} & 0 & \phi_{2,i-4} & 0 \\ \phi_{1,i-5} & 0 & \phi_{2,i-5} & 0 \\ \phi_{1,i-6} & 0 & 0 & \phi_{2,i-6} \\ \phi_{1,i-7} & 0 & 0 & \phi_{2,i-7} \\ \phi_{1,i-8} & 0 & 0 & \phi_{2,i-8} \end{bmatrix} , \begin{array}{l} k = 1,...,m' \\ i = 9,10,...,9m' \end{array} \tag{3.12}$$

$$\{x\}_k = \begin{Bmatrix} k_k \\ c_l \\ c_{l-1} \\ c_{l-2} \end{Bmatrix} , \begin{array}{l} k = 1,...,m' \\ l = 3,4,...,3m' \end{array} \tag{3.13}$$

66

$$\{I\}_k = \begin{Bmatrix} I_i \\ I_{i-1} \\ I_{i-2} \\ I_{i-3} \\ I_{i-4} \\ I_{i-5} \\ I_{i-6} \\ I_{i-7} \\ I_{i-8} \end{Bmatrix}, \begin{aligned} k &= 1,...,m' \\ i &= 9,10,...,9m' \end{aligned} \tag{3.14}$$

Further, $I_i, i = 1,...,9m'$ and $\phi_{1-2,i}, i = 1,...,9m'$ are defined from Equations (3.6) and (3.9) at each time step $\Delta t_i, i = 1,...,9m'$, respectively. The least squares solution of the matrix Equation (3.11) yields the unknown vector $\{x\}_k$. The overall fault diagnosis procedure presented is summarised in Figure 3.6.
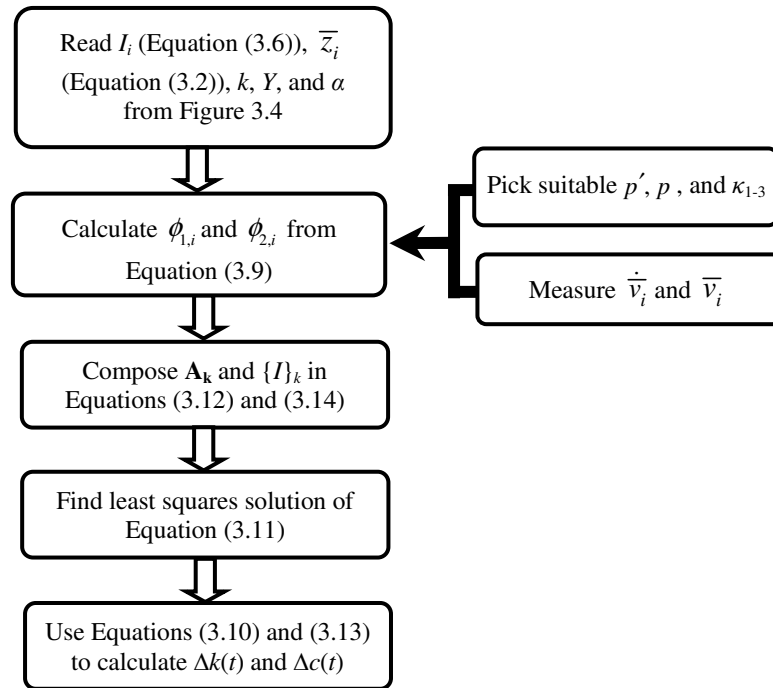
Figure 3.6. Flowchart of each time step in the fault diagnosis method developed using PLLSQ fitting

3.5.   Simulated proof-of-concept structure

To evaluate the performance of this real-time fault detection and diagnosis algorithm for SHM of nonlinear hysteretic base-isolation systems, a realistic base-

isolated system is created. Its basic definition includes: $m=156\times10^3$ kg, $c=2\times10^4$ N.s/m, $k=6\times10^6$ N/m, $\alpha=0.6$, $Y=0.6$ m, $A=1$, $\beta=\gamma=0.5$, and $n=3$, similar to (Ikhouane et al. 2005; Vidal et al. 2010). The simulated structure is subjected to the Loma Prieta earthquake with PGA of 0.27 g (EQ9 in Table 2-1). The values $\kappa_1=500$, $\kappa_2=1$, and $\kappa_3=50$ are used for the scaling factors, and were determined by following the procedure explained in Figure 3.3.

Nonlinear dynamic analysis is performed in MATLAB® to represent the nonlinear hysteretic behaviour of the system. Simulated responses from MATLAB® are used to provide proof-of-concept data for the fault detection and diagnosis algorithm developed and are sampled at 1 kHz. The simulated system is subjected to three worst-case sudden fault patterns, including stiffness, damping, and combined stiffness and damping faults, to evaluate the proposed SHM algorithm's performance.

To assess the efficacy of the method under harmonic motions, which may be the case in marine structures, the proof-of-concept structure is subjected to a sinusoidal excitation of amplitude 0.2 g and frequency of 1.0 Hz. This frequency is chosen to match the natural frequency of the simulated structure and maximise any instability in the base-isolation system. Simulation-derived data is recorded at 1 kHz ($\Delta t_i=0.001$ s), and results are smoothened in real time using a low-pass filter to cancel erroneous jumps occurred at sudden change time stamps in the damage patterns used.

3.6. Results and discussion

Figure 3.7a shows a sample stiffness fault pattern and the resultant residual signal when the simulated structure is subjected to the Loma Prieta earthquake. Figures 3.8a and 3.9a show the same results for the damping, and combined stiffness and damping fault examples, respectively. Finally, Figure 3.10a shows the calculated

residual signal for a combined case of fault where the structure is under harmonic excitation.

As these figures show, the residual signal designed is sensitive to changes as small as ±5% in stiffness and damping of the system, and the residual signal immediately goes back to its zero prior-to-fault state once the fault disappears. In some special cases, the two types of stiffness and damping faults may have equal effects on the system responses, but in opposite directions. In such situations, although there is a fault in the system, the residual signal remains zero. This result is expected given that the residual signal relies on observing a change in the system responses.

Figures 3.7b to 3.10b show the identified changes in stiffness and damping of the simulated base-isolation system using the developed diagnostic approach for each of the different fault patterns used in the simulations. These figures clearly show that the algorithm is very capable of tracking different combinations of faults in real time. The only errors are due to delay in the identification results. This delay is caused in the low-pass filtering process of the erroneous jumps occurring at the sudden damage times and can be shortened using more sophisticated filtering methods or higher sampling rates in the fault diagnosis process. However, maximum delay in the identification results presented is ~0.8 s, which is largely acceptable.

The total computation time for each time step in the simulation is ~5e-5 s on a 1.60 GHz Intel® dual core desktop machine. This is ~5% of the 0.001-second time step (1 kHz sampling rate) used. Moreover, the proposed algorithm only relies on the prior time step values. Therefore, the proposed algorithm is computationally quite light, and can be readily implemented as an on-line fault detection and diagnosis method.

(a)

(b)
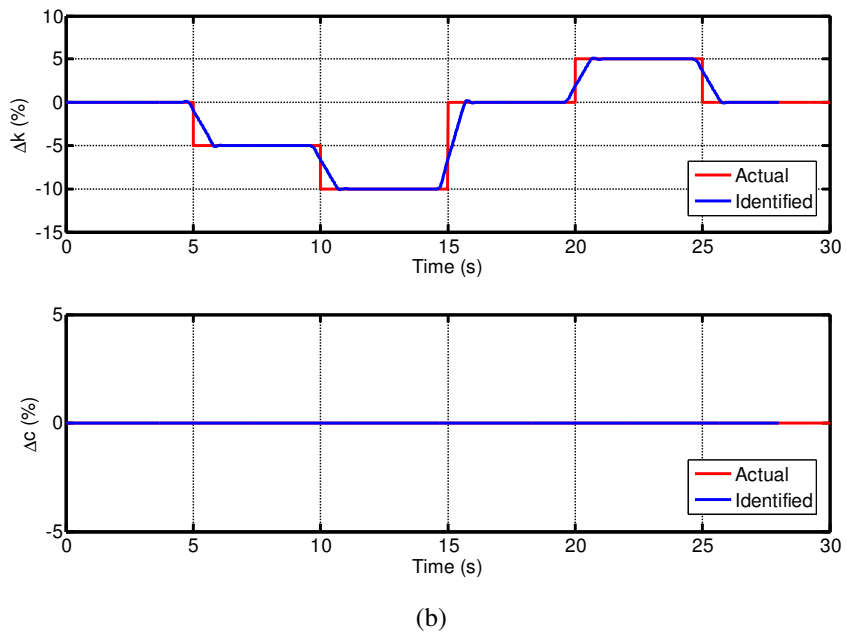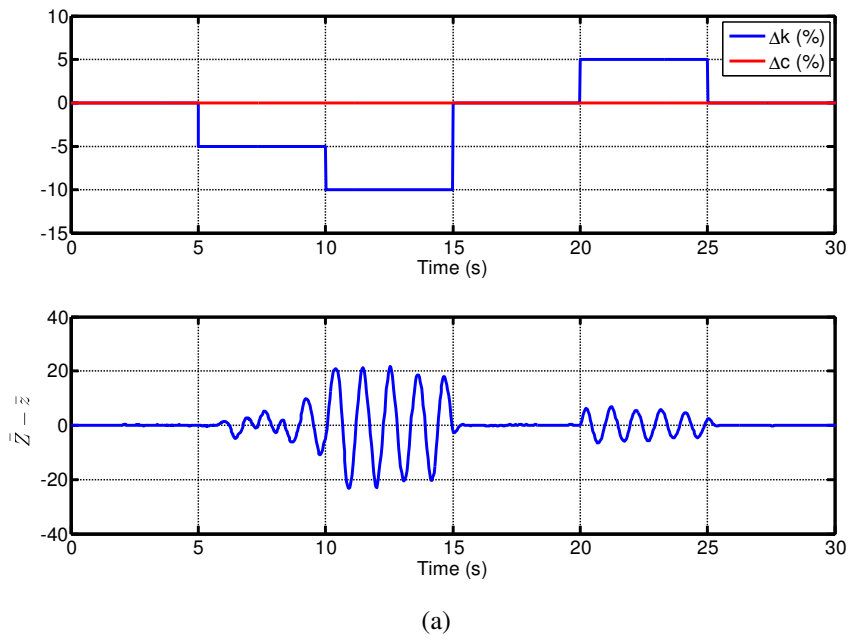
Figure 3.7. a) Fault and residual signal and b) identified faults for a sample stiffness fault in the simulated base-isolation system under the Loma Prieta earthquake
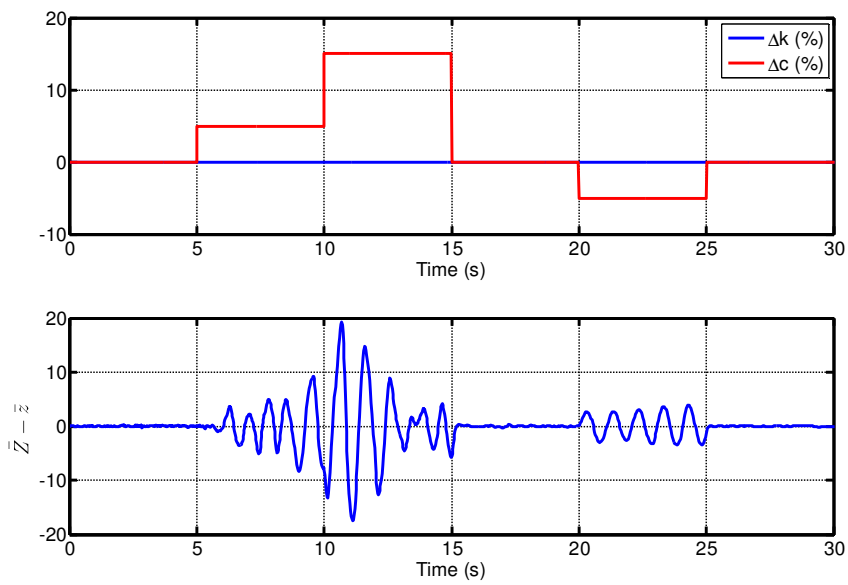
(a)
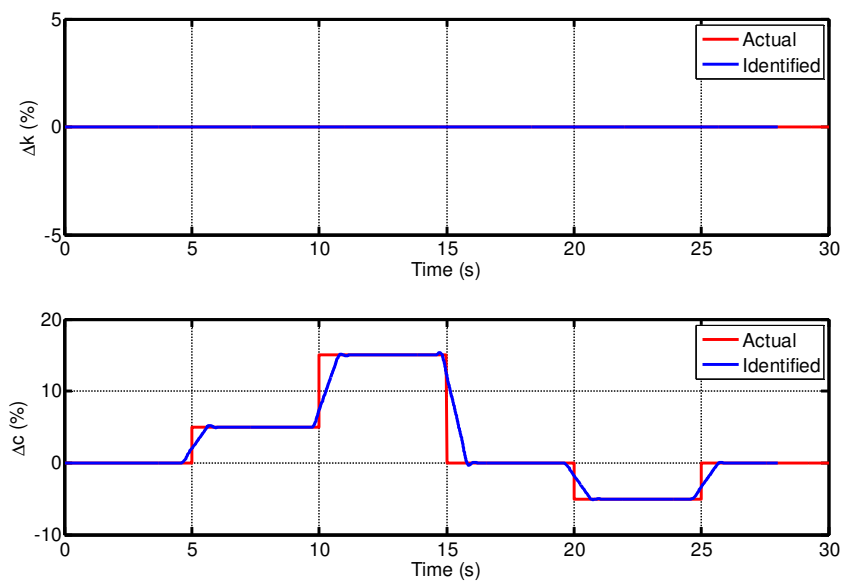
(b)

Figure 3.8. a) Fault and residual signal and b) identified faults for a sample damping fault in the simulated base-isolation system under the Loma Prieta earthquake
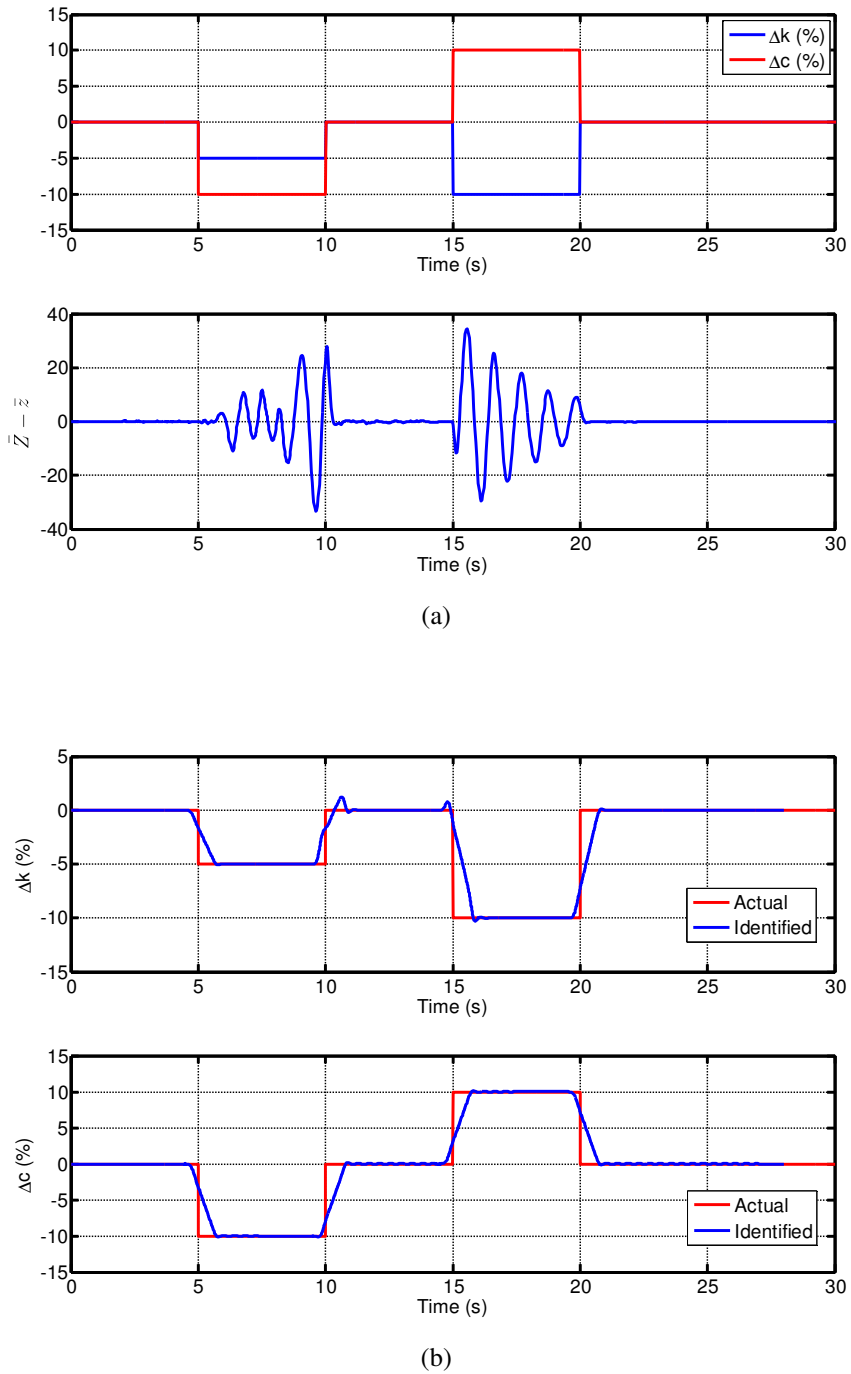
Figure 3.9. a) Fault and residual signal and b) identified faults for a sample combined stiffness and damping fault in the simulated base-isolation system under the Loma Prieta earthquake
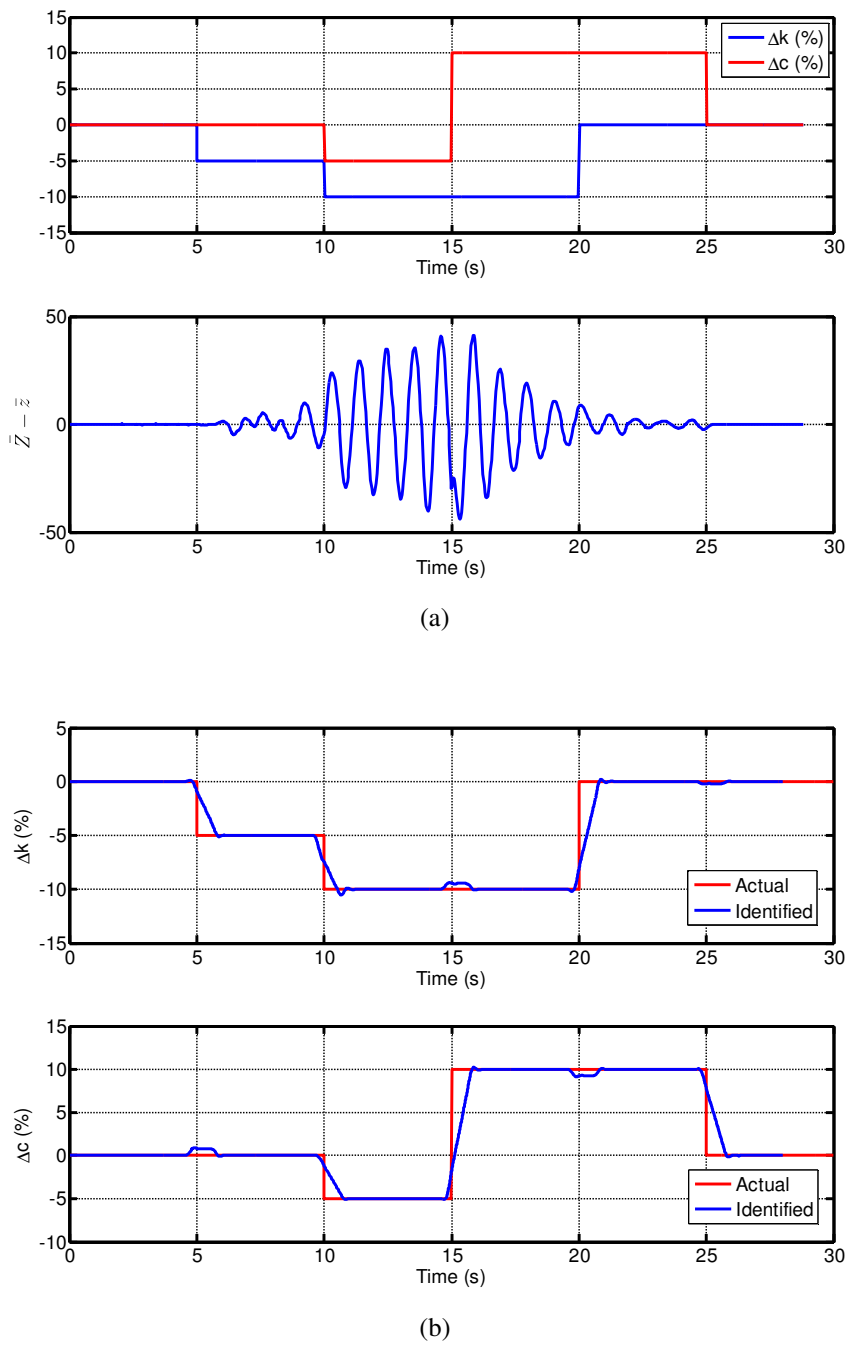
Figure 3.10. a) Fault and residual signal and b) identified faults for a sample combined stiffness and damping fault in the simulated base-isolation system under a harmonic ground motion of amplitude 0.2 g and frequency of 1.0 Hz

3.7.   Summary

In recent years, base-isolation has become an increasingly applied structural design technique in highly seismic areas. Sliding and elastomeric bearing systems are typically used to isolate the top superstructure from the shaking ground to maintain the structure's integrity during earthquakes. However, these systems increase the base displacements in near-fault motions. The state-of-the-art practice to also limit base displacement is to use active or passive MR dampers or similar nonlinear devices. The impact of faults in the overall base-isolation system on the isolated superstructure requires that the resulting nonlinear hysteretic system to be monitored in real time for possible changes in the two most important structural parameters: stiffness and damping.

This chapter developed a simple fault detection and diagnosis technique based on comparing the internal dynamics of the base-isolation system with those of a healthy baseline model to detect faults. It leverages the extensive design knowledge available for such isolation systems. Three different cases of stiffness, damping, and combined stiffness and damping faults were studied, *in silico*, on a realistic base-isolated structure subjected to the Loma Prieta earthquake with a passive MR damper. The simulation results showed that the proposed fault detection and diagnosis algorithm is very capable of detecting the existence, determining the type, and quantifying the severity of faults in the system in real time as the faults occur. The real-time diagnostic information provided can thus be used to provide the input data required for advanced structural control methods to compensate the faults occurred and consequently avoid damage to the overall structural system. Equivalently, they provide real-time information on the system status.

Measured system responses and input ground motion accelerations used in the

fault detection and diagnosis algorithm presented are assumed to be filtered for noise prior to the fault detection and diagnosis process. Noise impact on performance of the RT-SHM method developed needs to be assessed before experimental validation and implementation of the technique in the field.

CHAPTER 4

Parameter analysis of the Bouc-Wen model

4.1.   Introduction

Structures exhibit inelastic behaviour under severe seismic, wind, or repeated wave loads. The restoring forces caused by the internal friction in the structure, if plotted versus structural displacements, form hysteresis loops, where the restoring forces depend not only on the instantaneous displacements, but also on the history. Similarly, some nonlinear vibration isolation devices, such as elastomeric dampers (Constantinou and Tadjbakhsh 1985), MR dampers (Spencer et al. 1997), and wire rope

isolators (Demetriades et al. 1993), are designed to dissipate energy through hysteretic behaviour. Hysteresis is thus particularly important in modelling the damping characteristics of a broad range of nonlinear structures and systems.

One of the most widely accepted models, as described in the previous chapters, is a first-order nonlinear differential equation proposed by Bouc (1967) and later generalized by Wen (1976). The differential equation contains five unspecified parameters that can be chosen to generate a broad range of different hysteresis loop shapes. Results of a parameter or sensitivity analysis (SA) of the Bouc-Wen model could enable using simpler and more suitable forms of the model with less unidentified parameters for RT-SHM. In particular, less sensitive parameters can be fixed on values determined by basic engineering judgements based on limited available information from the structure. This approach removes the need to identify unimportant and difficult-to-determine parameters in the SHM process, particularly, where very limited knowledge of the structure is available prior to the identification.

Some studies have been conducted to quantify the importance of each parameter in the Bouc-Wen model on overall responses of different hysteretic structures, and to rank the parameters, accordingly. One of the first efforts to analyse sensitivity of the Bouc-Wen model parameters is the work by Ni et al. (1998). They used partial derivatives of the overall hysteretic structural model with respect to each parameter, while the others were fixed, to evaluate local sensitivity of the Bouc-Wen model to its five parameters.

In a similar study, Xiaomin et al. (2009) evaluated local and 'global' sensitivity of the output force of a MR damper, as a Bouc-Wen type hysteretic system, to its eight parameters. They changed one parameter at a time, while others were fixed, and compared the maximum mean square error induced in the output force to evaluate the

local sensitivity of the MR damper model to its parameters. To assess the sensitivity of the MR damper model in a global sense, considering interactions and influences of all the parameters simultaneously, Xiaomin et al. proposed a modified local sensitivity analysis (LSA) method. Their method generates input and output distributions required for evaluating model and parameter uncertainties in a global sense. Unlike the LSA, in their global sensitivity analysis (GSA), maximum mean square errors are compared when one parameter is varied at a time and others are left unrestrained.

A more detailed study on the sensitivity of the Bouc-Wen model was conducted by Ma et al. (2004) for the extended Bouc-Wen model with 13 parameters. Local and global sensitivity analyses were conducted using the one-parameter-at-a-time method and the Sobol indices (Sobol' 1990; Sobol' 2001), respectively. Another example of similar studies is the recent work by Worden and Becker (2011), which uses a principled Bayesian approach for parameter sensitivity analysis of the classical Bouc-Wen model with five parameters.

In this chapter, the classical Bouc-Wen model is carefully examined for the sensitivity of the model and consequently the overall responses of the structure to changes in each of the five parameters in the model. In particular, the chapter aims to show the importance of input excitation, natural frequency of the case-study structure, and base values used in the SA on the output results through simple one-parameter-at-a-time SAs. The mean LSA results for each case are then used to provide a 'global' sense of the sensitivity.

Different forms of the Bouc-Wen model and transformations used in the previous studies reviewed make comparison of the results for validation very difficult. However, the results are significant to the field in the sense that they underscore the importance of including factors, such as natural frequency of the case-study structure,

for more detailed SAs of the Bouc-Wen model in the future.

4.2. Variation of hysteresis loops with the Bouc-Wen model parameters

The Bouc-Wen model and its parameters were introduced in detail, in Sections 2.2 and 3.2. Here, only a very brief explanation is given for convenience. A SDOF shear-type nonlinear hysteretic structure can be modelled:

$$m\ddot{v}(t) + c\dot{v}(t) + \alpha \frac{F_y}{Y} v(t) + (1-\alpha)\frac{F_y}{Y} h(t) = -m\ddot{x}_g \tag{4.1}$$

where $\ddot{v}(t)$, $\dot{v}(t)$, and $v(t)$ are acceleration, velocity, and displacement of the structure, respectively, m is mass, and c is the equivalent viscous damping of the structure. The parameter α is the bi-linear factor. Further, F_y and Y are the yield force and the yield displacement of the structure, respectively, and $\ddot{x}_g$ is the input ground motion acceleration. Finally, h is the Bouc-Wen hysteretic displacement from Equation (2.18) (Bouc 1967; Wen 1976; Ikhouane and Rodellar 2007; Nayyerloo et al. 2011):

$$\dot{h}(t) = \dot{v}(t) \left\{ A - \left| \frac{h(t)}{Y} \right|^n \left(\beta sign\left(\dot{v}(t)h(t)\right) + \gamma \right) \right\}$$
$$A > 0, \beta > 0, -\beta < \gamma \le \beta, n \ge 1 \tag{4.2}$$

where A, β, γ, and n are stiffness, loop fatness, loop pinching, and abruptness parameters in the classical Bouc-Wen model, respectively. Further, n, the power factor, determines the sharpness of the curve from elastic to plastic force-deflection (hysteretic displacement versus actual displacement) behaviour of the structure. The five dimensionless parameters (A, β, γ, n, and α) determine the hysteresis force-deflection loop shape, and in the case of hysteretic-actual displacement loop, as used in this chapter, only four parameters (A, β, γ, and n) determine the loop shape.

Figure 4.1 to Figure 4.4 and Table 4-1 show how hysteresis loops evolve with

changes in each of the four parameters of the Bouc-Wen model of Equation (4.2) for a SDOF structure subjected to a harmonic acceleration of amplitude 10.0 and frequency of 1.0 Hz. As Figure 4.1 shows, changes in the stiffness parameter (A), as the name suggests, change the initial slope of the loop, and consequently the rest of the loop shape, as it essentially follows the initial slope. Moreover, the figure clearly shows that greater values of A result in higher maximum hysteretic displacements and widen the hysteresis loops vertically with only a small change in the loop fatness in the horizontal direction. This latter change is basically a result of change in the initial slope.

Figure 4.2 shows how changes in the loop fatness parameter (β) change hysteresis loop shape. Since $-\beta < \gamma \leq \beta$, the nominal value for γ has been set low to 0.1 in this figure to allow a wider range for changes in β to be studied. As the figure shows, higher values of β expand the loop horizontally by lowering the maximum hysteretic displacement and consequently the post-yield slope of the loops, yielding fatter hysteresis loops over a fixed range of actual displacements. Moreover, the resulting changes in the post-yield slope shrink the loops vertically at a greater rate than the horizontal contractions.
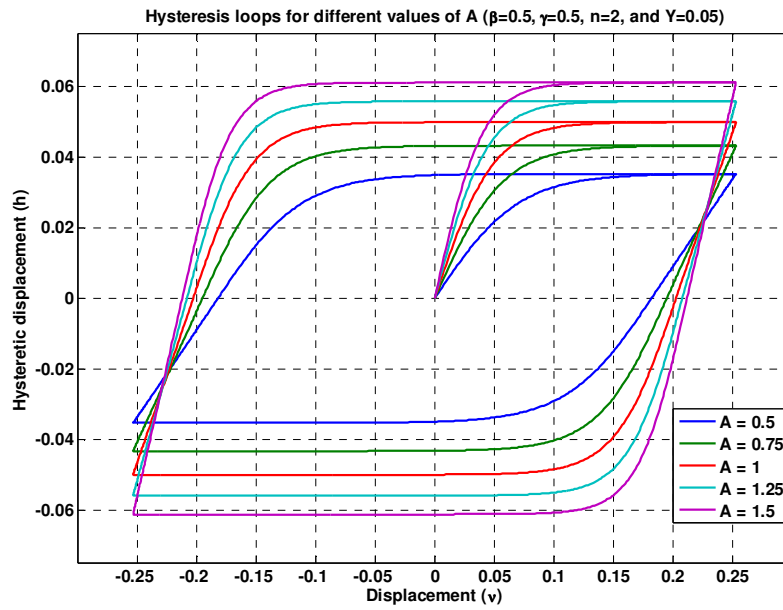
Figure 4.1. Hysteresis loop shape for different values of *A* (*β=γ*=0.5, *n*=2, and *Y*=0.05)
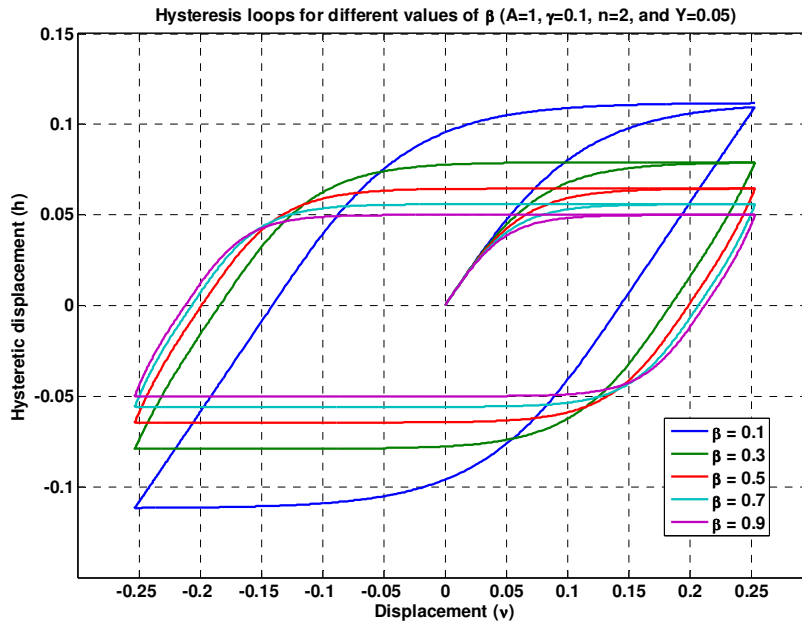
Figure 4.2. Hysteresis loop shape for different values of *β* (*A*=1, *γ*=0.1, *n*=2, and *Y*=0.05)

The effect of changes in the loop pinching parameter (γ) is studied in Figure 4.3. As the figure presents, unlike β, increase in the loop pinching factor shrinks the loops vertically without any important change in the loop fatness in the horizontal direction. The values for γ=-0.5 are quite extreme because γ=-β in this case and no yielding occurs. This case does not represent an actual physical structure, as described in Section 2.2, and only has been given to further evaluate the effect of γ.

Table 4-1 includes a suite of 99 different hysteresis loop shapes for different values of the two loop fatness (0.1≤β≤0.9) and loop pinching parameters (-0.9≤γ≤0.9) of the Bouc-Wen model. In each figure in the table, the dotted loop represents the loop shape for β=γ=0.5 and has been shown as a reference for comparison. The table provides similar comparisons as in Figure 4.2 and Figure 4.3 in each row or column for various fixed values of β or γ, respectively, and confirms the previous results. Once again, the case of γ=-β in the table, does not represent a physical system behaviour and has been given for completeness and only to show the loop shape in this unrealistic limit case.

Finally, as shown in Figure 4.4, the power factor (n) changes the smoothness of transition from elastic to plastic regions in the hysteretic versus actual displacement curve, without any significant change in the overall shape of the loop. As the power factor increases, the curve becomes sharper and approaches to a bi-linear transition as n goes to infinity.
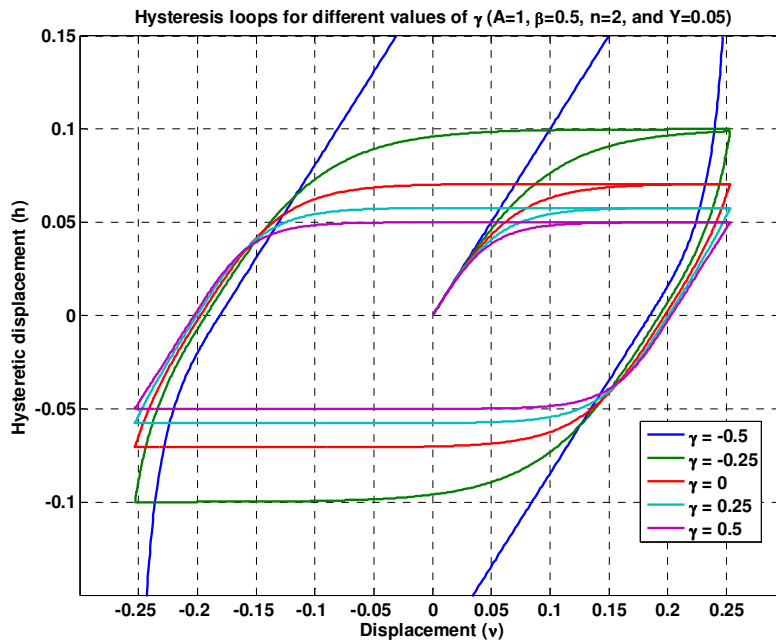
Figure 4.3. Hysteresis loop shape for different values of γ (A=1, β=0.5, n=2, and Y=0.05)
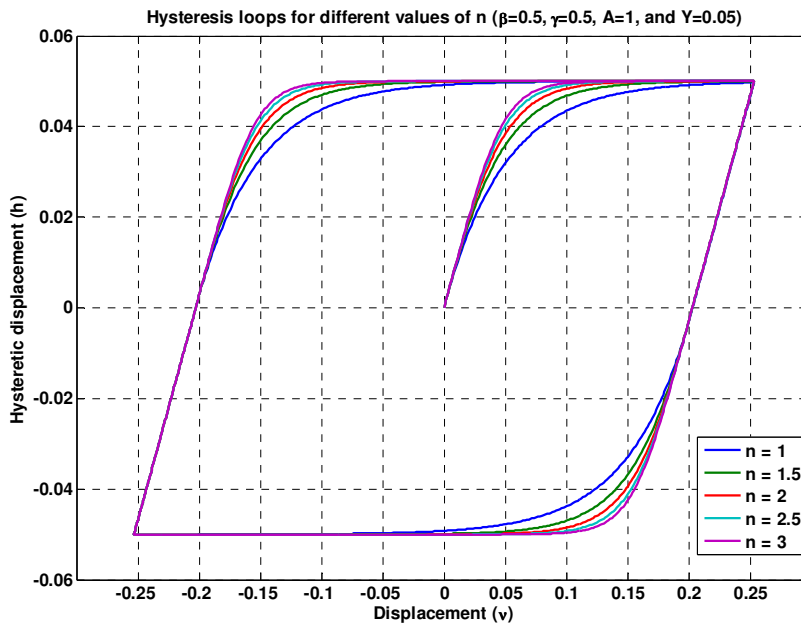
Figure 4.4. Hysteresis loop shape for different values of n (A=1, β=γ=0.5, and Y=0.05)

Table 4-1. Evolution of hysteresis loops with changes in the loop fatness (β) and pinching (γ) parameters (A=1, n=2, and Y=0.05)
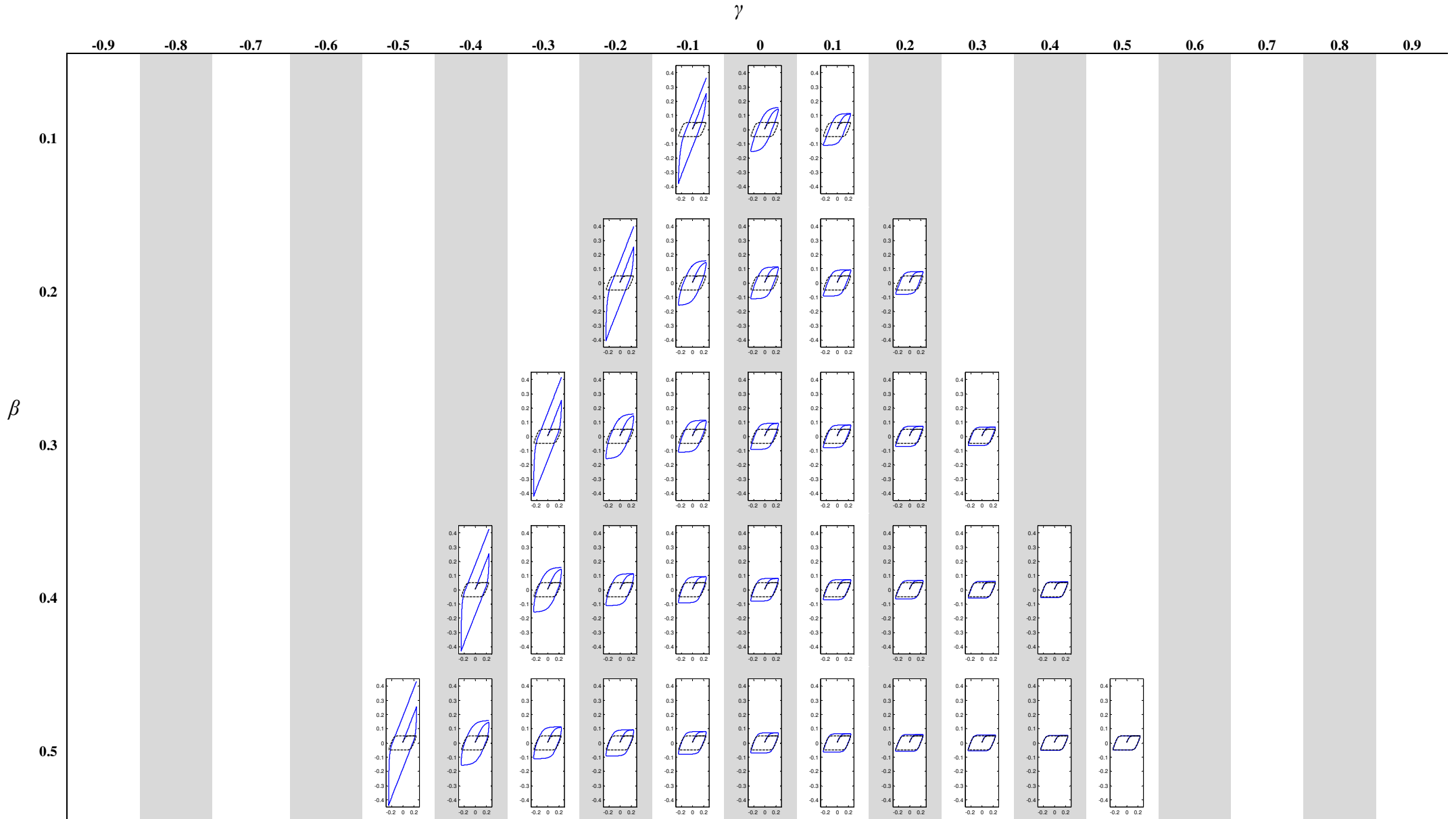
Table 4.1. Continued …

γ
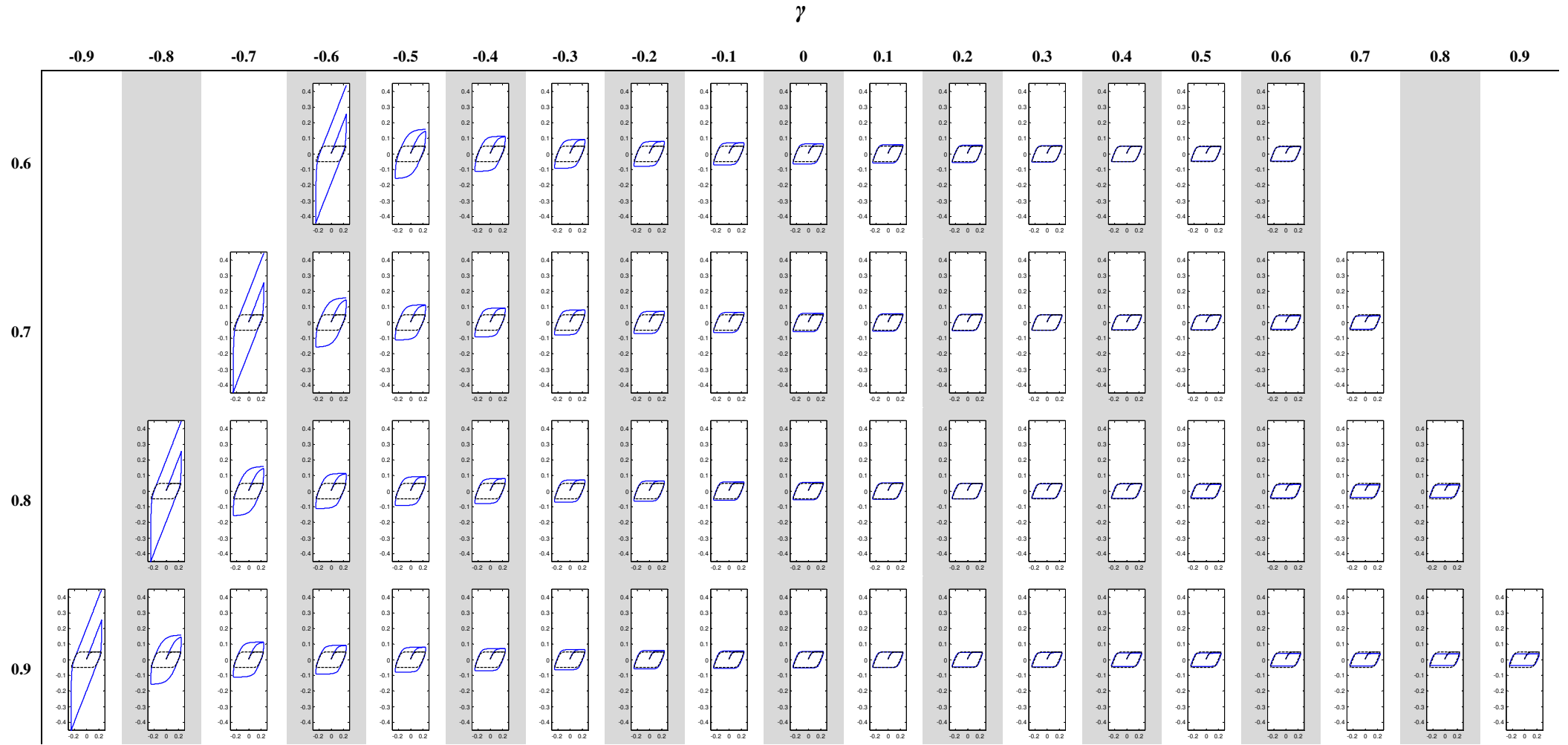
4.3.   Case-study structure

The simulated case-study structure for SA of the Bouc-Wen model is a SDOF model of a five-story concrete building described in Section 2.7 with m=996 tonnes, F_y=1270 kN, Y=50 mm, and 5% constant viscous damping. Three sets of base values, shown in Table 4-2, are chosen for the Bouc-Wen parameters. The choice of the base values is such that when they are varied for SA, the resulting range for each parameter satisfies the conditions under Equation (4.2) and remains within the normal range observed in the hysteresis loops of physical systems (Ikhouane and Rodellar 2007).

Table 4-2. Base values for the Bouc-Wen model parameters used in the LSA

Parameter	Set 1	Set 2	Set 3
A	0.5	1.0	1.5
α	0.0325	0.0650	0.0975
β	0.25	0.50	0.75
γ	-0.1	0.1	0.3
n	2.0	2.5	3.0

To evaluate the effect of different input excitations on the LSA results, the structure is subjected to the suite of ground motions in Table 2-1. Further, three different natural frequencies (0.5, 1.0, and 1.5 seconds) for the structure are considered to evaluate the effect of structure's natural frequency on the LSA results. The simulated structural responses from MATLAB® are then used for comparison with the responses of the baseline model with the nominal parameters in Table 4-2 to quantify the local sensitivity of the overall Bouc-Wen model of Equations (4.1) and (4.2) to its five parameters (A, β, γ, n, and α).

4.4.   Local sensitivity analysis

The simplest way to conduct sensitivity analysis is a method referred to as one-

parameter-at-a-time approach, where one parameter is changed at a time, while others are fixed at chosen nominal values (Hamby 1994). This method is local in the sense that it only addresses sensitivity relative to the chosen base values and not for the entire parameter range. Interactions of the parameters also cannot be evaluated by such a local technique (Ma et al. 2004). Further, the local sensitivity results are limited by the choice of base values, input excitations, and natural frequency of case-study structure used. However, the method is very capable of providing a graphical representation of sensitivity ranking.

To assess local sensitivity of the Bouc-Wen model to each of its five parameters using the one-parameter-at-a-time method, only one parameter is changed at a time and all other factors are fixed at their nominal values. Similar to Ma et al. (2004), maximum of the norm of error in structural responses caused by changes in each of the model parameters is used to quantify the model's local sensitivity:

$$RMSE_{\max} = \max \left\{ \left[\sum_{i=1}^{N} \left((v_i - v_{bi})^2 + (\dot{v}_i - \dot{v}_{bi})^2 + (h_i - h_{bi})^2 \right) \right]^{\frac{1}{2}} \right\}, N = 1, 2, 3, \ldots \qquad (4.3)$$

where v_i, $\dot{v}_i$, and h_i are respectively the displacement, velocity, and the hysteretic displacement of the model when a parameter is varied, and v_{bi}, $\dot{v}_{bi}$, and h_{bi} are respectively the displacement, velocity and the hysteretic displacement of the structure with the nominal base values chosen for the Bouc-Wen model parameters. Further, N is the number of sampling points in simulation of the responses. Finally, $RMSE_{max}$ is the maximum of the norm of error in the responses, or the maximum root-mean-square (RMS) error. Each parameter of the model is varied ±50% of its base value with 5% steps, and the data is sampled at each 0.001 seconds for a total simulation time of 50 seconds (N=50k). There is no bias due to N as it has the same value for all cases.

Three different cases, as outlined in Table 4-3, are studied for LSA. First, the

analysis is carried out for three different natural periods of the case-study structure (0.5, 1.0, and 1.5 s) with a single set of nominal values for the Bouc-Wen parameters (Case 1 in Table 4-3). The structure is subjected to the El Centro ground motion (EQ19 in Table 2-1) in the three simulations to calculate the maximum RMS error in the responses.

Second, a fixed natural period of 1.0 second for the case-study structure with three different sets of base values for the Bouc-Wen parameters are considered (Case 2 in Table 4-3), and the structure is again subjected to the El Centro earthquake in Table 2-1. Finally, a fixed natural period of 1.0 second with a single set of base values for the hysteresis parameters are studied for LSA of the Bouc-Wen model under the suite of 20 different ground motions in Table 2-1 (Case 3 in Table 4-3). Using different input excitations in the simulation significantly reduces errors in LSA results associated with the type of excitation used.

Table 4-3. Different cases studied for LSA of the Bouc-Wen model

Simulation parameter	Case 1	Case 2			Case 3
Natural period (s)	0.5 1.0 1.5		1.0		1.0
A	1.0	0.5	1.0	1.5	1.0
α	0.0650	0.0325	0.0650	0.0975	0.0650
β	0.50	0.25	0.50	0.75	0.50
γ	0.3	-0.1	0.1	0.3	0.3
n	1.5	2	2.5	3	1.5
Input excitation (as in Table 2-1)	EQ19		EQ19		EQ1-20

4.5.   Global sensitivity analysis

Global sensitivity analysis can account for the interactions of the parameters in a multi-parameter model. Some of the popular methods for GSA have been reviewed in (Hamby 1994). There are also several techniques based on conditional variances of model output for GSA such as (Iman and Hora 1990; Chan et al. 2000). However, more

common methods are Fourier Amplitude Sensitivity Test (FAST) (Saltelli and Bolado 1998) and the Sobol probabilistic sensitivity indices (Sobol' 1990; Sobol' 2001).

The Sobol indices are generally superior to FAST in that the single and multi-parameter indices can be represented by the same equations and thus can be calculated in a similar way, yielding a simpler overall procedure for GSA. Homma and Saltelli (1996) introduced the total effect sensitivity indices, based on the work by Sobol, to measure the mutual interactions of parameters in groups of two, three, or more. In this chapter, the mean LSA results for the three different cases in Table 4-3 are used only to provide a 'global' sense of the sensitivity of the model, and the emphasis is on the fact that the model is not equally sensitive to its five parameters. For a more thorough GSA of the Bouc-Wen model, any of the methods reviewed earlier can be used.

4.6.   Results

Results for LSA of the Bouc-Wen model for Case 1 in Table 4-3, with different natural periods for the case-study structure, are shown in Figure 4.5. As the figure shows, the results generate spider-like graphs with zero RMS errors at the centre and growing RMS errors as the change in the parameters increases. For the three different natural periods studied, RMS errors induced in the structural responses due to change in A, are considerably greater than errors for the other four parameters. Moreover, no uniform pattern is observed for the remaining places in the ranking for the three different natural periods studied. For instance, in Figure 4.5a, for the natural period of 0.5 s, changes in the power factor, n, has greater effects on the RMS errors compared to the remaining three, whereas in Figure 4.5c, β has the second greatest effect on the responses.
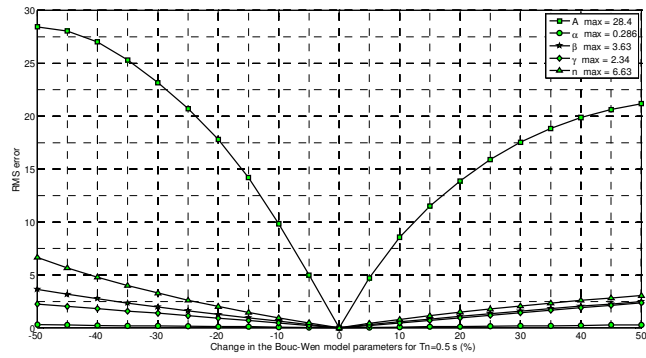
(a)
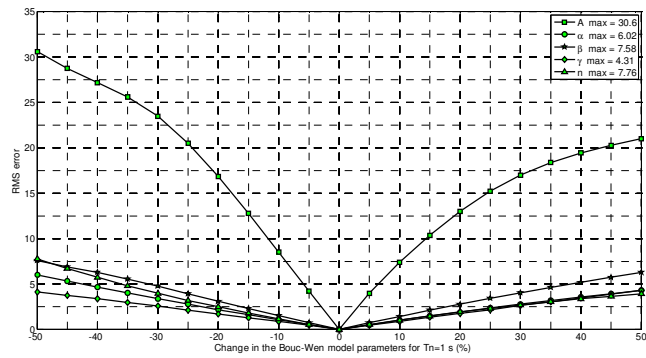
(b)
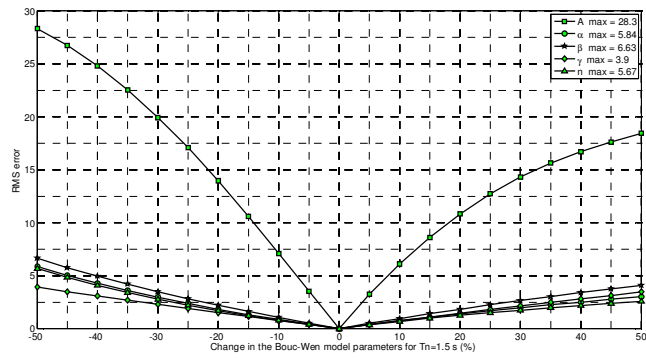
(c)
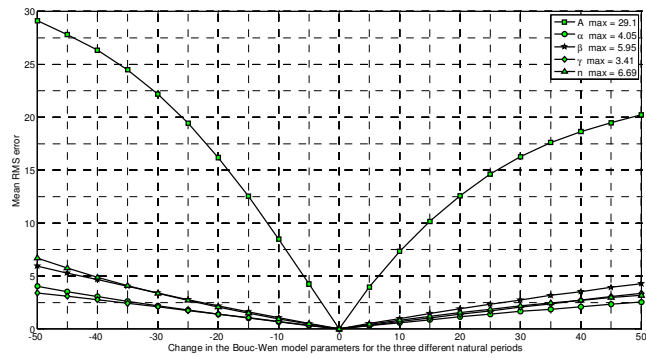
(d)

Figure 4.5. Spider diagrams generated using the LSA results for the Bouc-Wen hysteretic model for structures with different natural periods: a) T_n=0.5 s, b) T_n=1.0 s, c) T_n=1.5 s, and d) the average results.

Maximum RMS errors for the three different natural periods in Case 1 are summarised in Table 4-4. The average maximum RMS errors for the three natural periods are also shown in the table. The average results yield a sensitivity ranking of the parameters as $A>n>\beta>\alpha>\gamma$.

Table 4-4. Results of LSA of the Bouc-Wen model for Case 1 in Table 4-3 with different natural periods for the case-study structure

Natural period (s)	0.5		1.0		1.5		Mean	
	RMSE	Rank	RMSE	Rank	RMSE	Rank	RMSE	Rank
A	28.40	1	30.60	1	28.30	1	29.10	1
α	0.29	5	6.02	4	5.84	3	4.05	4
β	3.63	3	7.58	3	6.63	2	5.95	3
γ	2.34	4	4.31	5	3.90	5	3.52	5
n	6.63	2	7.76	2	5.67	4	6.69	2

Figure 4.6 shows similar LSA spider diagrams for Case 2 in Table 4-3 with different base values for the Bouc-Wen model parameters. As the figure shows, variations of the stiffness parameter again generate much greater errors in the responses compared to the other parameters. The resulting parameter rankings for each of the three different sets of base values are shown in Table 4-5. As the table shows, based on the average maximum RMS errors for each of the Bouc-Wen parameters in the three different sets, the overall ranking for Case 2 is also $A>n>\beta>\alpha>\gamma$.
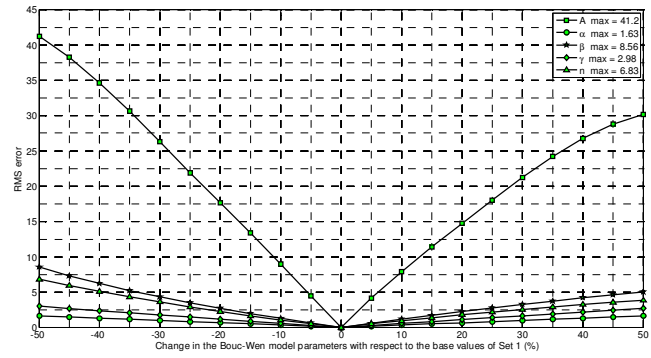
(a)
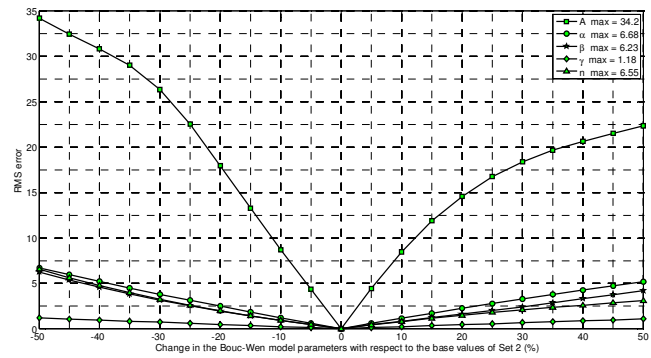
(b)
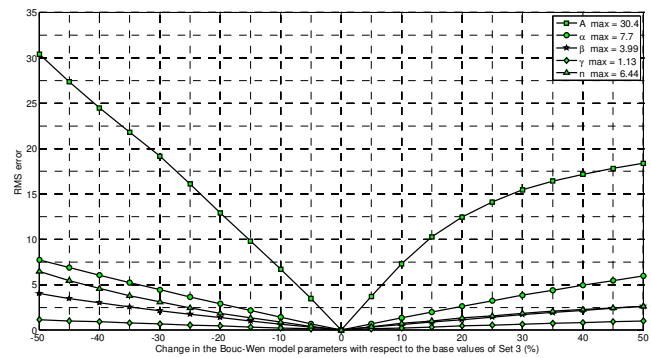
(c)
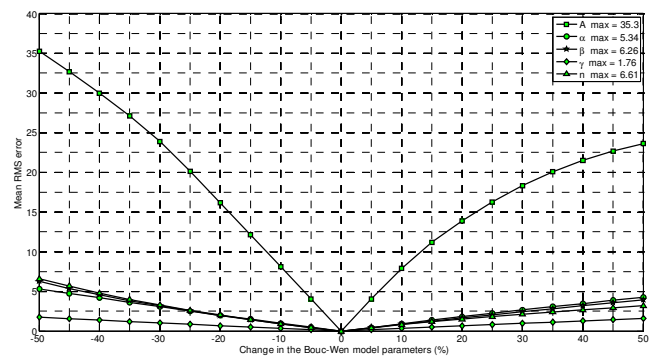
(d)

Figure 4.6. Spider diagrams of the LSA results for the Bouc-Wen hysteretic model generated for different base values for the parameters: a) Set 1, b) Set 2, c) Set 3, all from Table 4-2, and d) the average results.

Table 4-5. Results of LSA of the Bouc-Wen model for Case 2 in Table 4-3 with different base values for the model parameters

Set #	Set 1		Set 2		Set 3		Mean	
	RMSE	Rank	RMSE	Rank	RMSE	Rank	RMSE	Rank
A	41.20	1	34.20	1	30.4	1	35.30	1
α	1.63	5	6.68	2	7.70	2	5.34	4
β	8.56	2	6.23	4	3.99	4	6.26	3
γ	2.98	4	1.18	5	1.13	5	1.76	5
n	6.83	3	6.55	3	6.44	3	6.61	2

Results for the LSA of the Bouc-Wen model for Case 3 in Table 4-3, under the 20 different ground motion records in Table 2-1, are shown in Figures 4.7 to 4.11 for each model parameter individually. Results for each step change in the model parameters for the 20 different records are presented in the format of box plots, and the median values of different boxes are compared to evaluate sensitivity of the model to each parameter. In total, for each parameter, 420 different cases (20 record×21 steps) are studied to generate median RMS error trend lines for LSA of the Bouc-Wen model under different input excitations. Boxes in the figures are stretched along the vertical axis. This result clearly shows that changes in the input excitation have a significant effect on the RMS errors in the structural responses and consequently on the LSA results. This outcome is more evident for greater changes in the model parameters.

The median trend lines of the LSA results for Case 3 are compared for different model parameters in Figure 4.12. As the figure shows, once more, changes in the stiffness parameter have significantly greater effect on the responses compared to the other parameters in the Bouc-Wen model. Further, trend lines on the left-hand side of the centre point in the figure, have higher slopes than the trend lines for the same parameter on the right-hand side. This result reveals that for all the Bouc-Wen model parameters, a decrease in the parameter value results in a higher error in the response compared to the same amount of increase in the parameter value. This behaviour is also

seen in Figures 4.5d and 4.6d for the first two cases in Table 4-3.

Parameter ranking for Case 3 is shown in Table 4-6. The maximum median RMS error results for the entire suite of records used in the analysis are used to rank the parameters in order of their effect on the responses of the case-study structure. The maximum median RMS errors for three earthquake records with different PGAs are also shown in the table for comparison. The maximum median errors for the 20 different records used yields a parameter ranking as $A>n>\beta>\gamma>\alpha$ for Case 3. This ranking largely agrees with the rankings for the first two cases except for the order of the last two parameters.
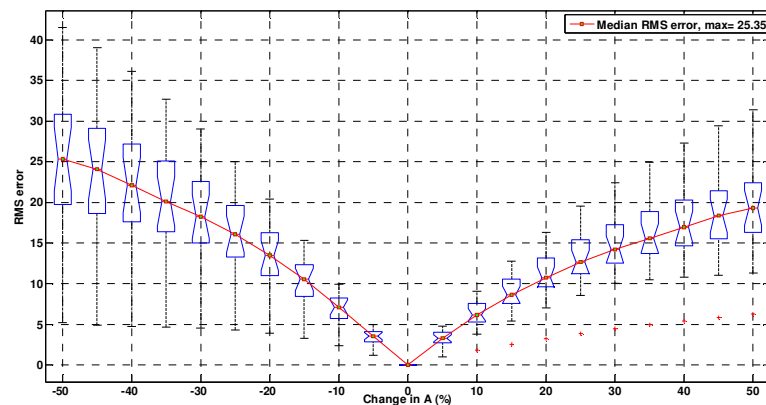
Figure 4.7. RMS error in the responses of the case-study structure due to change in the stiffness parameter of the Bouc-Wen model, A, for Case 3 in Table 4-3.
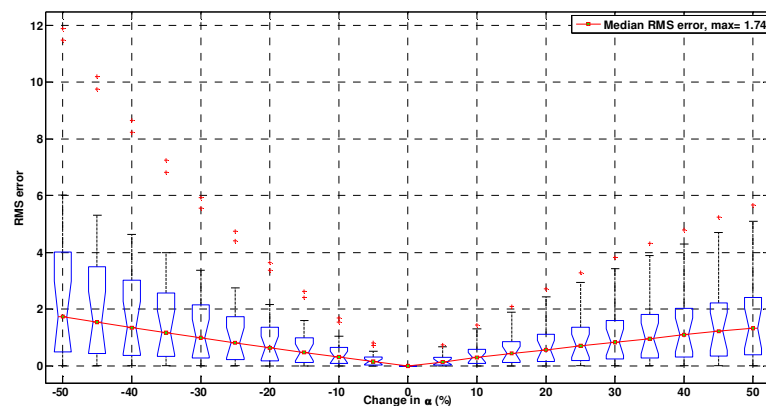
Figure 4.8. RMS error in the responses of the case-study structure due to change in the bi-linear factor of the Bouc-Wen model, α, for Case 3 in Table 4-3
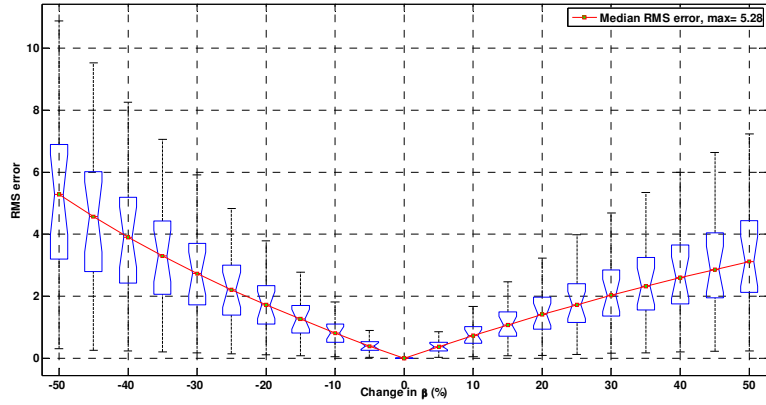
Figure 4.9. RMS error in the responses of the case-study structure due to change in the loop fatness parameter of the Bouc-Wen model, β, for Case 3 in Table 4-3
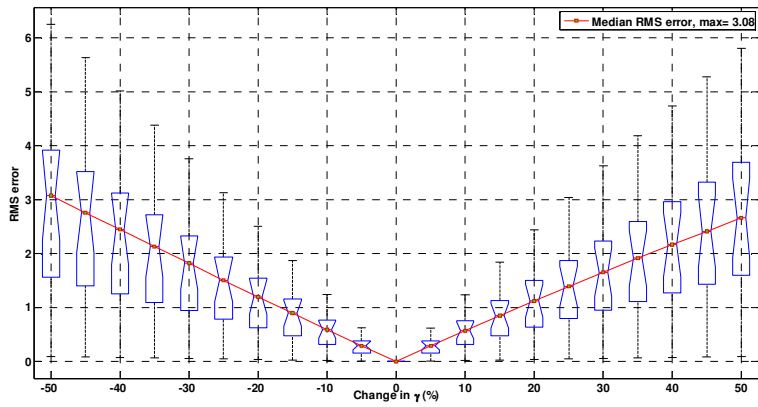
Figure 4.10. RMS error in the responses of the case-study structure due to change in the loop pinching parameter of the Bouc-Wen model, γ, for Case 3 in Table 4-3
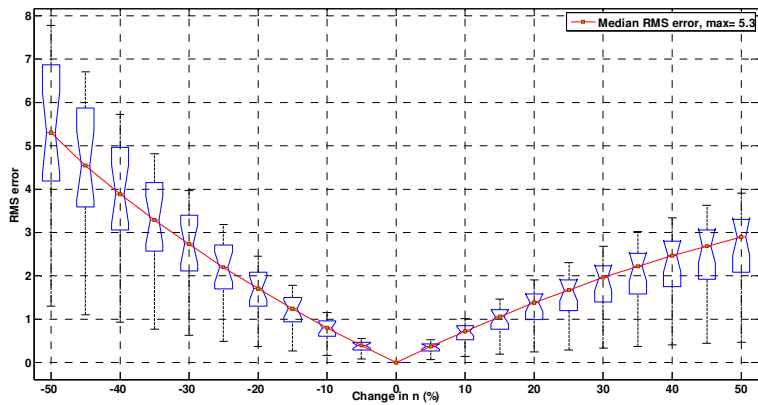
Figure 4.11. RMS error in the responses of the case-study structure due to change in the power factor of the Bouc-Wen model, n, for Case 3 in Table 4-3
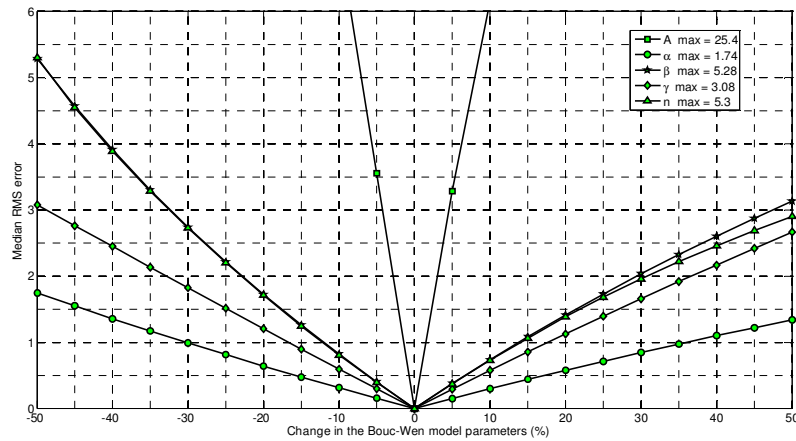
Figure 4.12. Spider diagram generated by median RMS errors in the responses of the case-study structure due to change in the Bouc-Wen model parameters for Case 3 in Table 4-3

Table 4-6. Results of LSA of the Bouc-Wen model for Case 3 in Table 4-3 with different input excitations of Table 2-1.

Record # (PGA in g)	EQ1 (0.116)		EQ19 (0.358)		EQ11(0.617)		Median (EQ1-20)	
	RMSE	Rank	RMSE	Rank	RMSE	Rank	RMSE	Rank
A	41.54	1	30.57	1	15.18	1	25.41	1
α	3.95	5	6.02	4	0.18	5	1.74	5
β	8.14	2	7.58	3	2.60	3	5.28	3
γ	4.95	4	4.30	5	1.23	4	3.08	4
n	7.70	3	7.76	2	3.19	2	5.30	2

Table 4-7 summarises the results for the three different cases considered for LSA in Table 4-3. The overall ranking of the model parameters, based on the maximum mean/median RMS errors induced in the structural responses, due to changes in the model parameters, shows that the Bouc-Wen model is considerably more sensitive to A, followed by a large distance with n, $β$, $α$, and finally $γ$. The ranking, includes the effect of different input excitations (20 records), different base values (3 sets), and different natural periods for the case-study structure (3 periods) and in a sense provides a 'global' sensitivity analysis results for the Bouc-Wen model.

Table 4-7. Summary of the results of LSA of the Bouc-Wen model with mean maximum RMS errors for Case 1 and 2, and maximum median RMS errors for Case 3.

Case # as in Table 4-3	Case 1		Case 2		Case 3		Overall Mean	
	RMSE	Rank	RMSE	Rank	RMSE	Rank	RMSE	Rank
A	29.10	1	35.30	1	25.41	1	29.94	1
α	4.05	4	5.34	4	1.74	5	3.71	4
β	5.95	3	6.26	3	5.28	3	5.83	3
γ	3.52	5	1.76	5	3.08	4	2.79	5
n	6.69	2	6.61	2	5.30	2	6.20	2

4.7.   Summary

The versatile classical Bouc-Wen model is one of the most widely used semi-physical models of hysteresis in structural mechanics. In this chapter, the classical Bouc-Wen model was carefully examined for the effect of its parameters on the overall hysteresis loop shape and consequently on the structural responses. Results for local and global sensitivity analyses were presented to assess relative sensitivity of overall performance of the structure to each of the parameters in the model. The results presented show that some parameters of the hysteretic model have rather less effect on structural responses, and thus could be fixed at values determined by basic engineering judgements based on the limited *a priori* knowledge of the structure. This approach would enable simpler, more suitable hysteretic models with less number of parameters to be identified in SHM of nonlinear hysteretic structures, particularly where RT-SHM is necessary or desired.

Overall, the local and 'global' sensitivity analysis results showed that the five parameters in the classical Bouc-Wen model can be ranked in order of their effect on structural performance as $A>>n>\beta>\alpha>\gamma$. However, the results presented are limited by hereditary problems using LSAs, and a more thorough GSA is needed to further study the mutual interactions of the parameters and limitations associated with the choice of

base values, input excitations, and natural frequencies used. However, the overall result

provides a fundamental and reasonable guideline for the use of these models.

CHAPTER 5

RT-SHM using a fast and slow dynamics separation technique

5.1.   Introduction

In Chapter 2, a simple, more suitable algorithm for RT-SHM of nonlinear hysteretic structures was developed to resolve issues of high computational cost and complexity with existing real-time health monitoring approaches. The parametric algorithm developed uses adaptive LMS filtering theory to identify key structural and nonlinear Bouc-Wen baseline model parameters in real time. The chapter assumes that limited knowledge of the structure is available prior to the SHM process to provide the minimum healthy baseline model data required for identification and health monitoring.

In particular, mass, geometrical or material properties required for a push-over FEA, damping factors, and the power factor in the nonlinear Bouc-Wen baseline model were assumed to be known or reasonably estimated from basic knowledge. Similarly, the RT-SHM method of Chapter 3 was predicated on the availability of full internal dynamics of the healthy Bouc-Wen baseline model prior to the health monitoring process for comparison with the faulty system's dynamics to identify damage. However, some of this information, particularly, the nonlinear baseline model parameters, may not be available *a priori*.

The two-step identification method developed in Chapter 2 can identify the Bouc-Wen model parameters. However, the first step in the identification process proposed is a push-over FEA that is a tedious process and cannot be implemented in real time. Therefore, any change in the off-line identified parameters using the push-over analysis, cannot be detected by the RT-SHM method of Chapter 2.

Simpler forms of the nonlinear Bouc-Wen model, with a smaller number of parameters, require fewer *a priori* known parameters to represent nonlinear hysteretic behaviour of the structure. These simpler forms could thus provide the opportunity of combining the two identification and health monitoring processes developed in Chapter 2, into an integrated one-step RT-SHM process. This approach enables identifying most or all of the structural and nonlinear baseline model parameters in real time, as an event occurs. Moreover, the RT-SHM algorithms of Chapters 2 and 3 require full-state structural response measurement, but displacement and velocity are very difficult to measure. Therefore, RT-SHM methods that are less dependent on structural displacement and velocity measurements are more suitable for implementation in the field.

The present chapter develops an on-line SHM algorithm for identification and

health monitoring of Bouc-Wen type nonlinear hysteretic structures using a simpler form of the Bouc-Wen model than the version used in Chapters 2 and 3. This new form has only three parameters, all of which can be identified in real time with no prior information of the structure, except for the structural mass and the Bouc-Wen power factor. Mass can be estimated reasonably accurately from the design by knowing the type and measuring geometrical dimensions of the structure. The power factor can also be either estimated based on limited *a priori* knowledge of the structure, or, where no such information is available, can be ignored using a linear-in-parameter form of the Bouc-Wen model (Acho and Pozo 2009).

The novel RT-SHM algorithm proposed in this chapter thus removes the need for push-over analysis and makes the health monitoring process significantly easier. Moreover, the algorithm proposed does not require structural displacement measurement, and relies only on measured accelerations and estimated velocities from integration of the accelerations measured. Therefore, the method is also superior to the previous algorithms developed in Chapters 2 and 3, in the sense that it removes the need for difficult to measure structural displacements to provide RT-SHM information.

The on-line parametric SHM algorithm proposed uses a fast and slow dynamics separation technique and robust PLLSQ fitting to identify and track key structural and nonlinear baseline model parameters. The method is thus able to uniquely identify structural stiffness, damping, and the Bouc-Wen hysteretic model parameters. Importantly, all of these values are directly related to well-recognised damage metrics.

Proof-of-method simulations of various combinations of damage, as modelled by changes in these parameters, are performed on a realistic nonlinear case-study structure. Noise-free input responses are used to evaluate the efficacy of the proposed algorithm in identifying structural parameters in real time. The effect of the specific

external load on performance of the proposed SHM method is evaluated using a suite of 20 different ground motions to test robustness of the results across a range of realistic inputs.

5.2.   Definition of the SHM problem

Equations of motion for a m-DOF shear-type nonlinear hysteretic structure under seismic loading can be written (Lin et al. 2001):

$$\mathbf{M} \cdot \{\ddot{v}\} + \{q(\{\dot{v}\}, \{v\}, t)\} = -\mathbf{M} \cdot \{I\} \cdot \ddot{x}_g \tag{5.1}$$

where $\mathbf{M}$, is the $m \times m$ diagonal mass matrix of the structure, $\{v\}$, $\{\dot{v}\}$, and $\{\ddot{v}\}$ are the $m \times 1$ displacement, velocity, and acceleration vectors, respectively, $\ddot{x}_g$ is the ground motion acceleration, $\{I\}$ is the identity column vector of order m, and finally, q is the $m \times 1$ total restoring force vector defined as the difference between the restoring forces of $(i\text{-}1)^{th}$ and i^{th} stories. The nonlinear hysteretic restoring force of each floor including the damping force, q_i, $i=1,..,m$, is governed by the following first-order nonlinear differential equation that is a form of the Bouc-Wen model described in Section 2.2 (Wen 1976; Lin et al. 2001; Yang and Lin 2004; Ismail et al. 2009):

$$\dot{q}_i = c_i \ddot{r}_i + k_i \dot{r}_i - a_i |\dot{r}_i| |q_i|^{n_i-1} q_i - b_i \dot{r}_i |q_i|^{n_i}, i=1,...,m \tag{5.2}$$

where c_i is the equivalent viscous damping and k_i is the equivalent stiffness of storey i, and $\ddot{r}_i$, $\dot{r}_i$, and r_i are the relative acceleration, velocity, and displacement between storey i and $i\text{-}1$, respectively. Further, a_i, b_i, and n_i are loop fatness, loop pinching, and abruptness parameters (power factor) of the ith storey in the Bouc-Wen model of hysteresis, respectively. Finally, m is the number of stories in the shear-type structure.

Ground motion acceleration, as well as accelerations at different floors, can be easily measured with low cost accelerometers at high sampling rates. Therefore, the

104

total restoring force vector, $\{q\}$, can be readily determined from Equation (5.1). Integration of measured accelerations without (Boyce 1970; Trifunac 1971; Trujillo and Carter 1982; Yang et al. 2006) or with (Hann et al. 2009) limited displacement data for integration drift correction also provides the velocities, $\{\dot{v}\}$ or $\{\dot{r}_i\}$. Hence, tracking the time-varying structural and Bouc-Wen parameters, c_i, k_i, a_i, and b_i in Equation (5.2), determines the structure's health in real time. The power factor, n_i, is assumed to be known *a priori* for each floor. In the case where no such information is available, the equivalent linear-in-parameter modified Bouc-Wen model, with the same proposed technique in this paper, can be used (Acho and Pozo 2009).

5.3.   Fast-slow dynamics separation

For simplicity, and due to the fact that when Equation (5.1) is solved for the restoring force vector, $\{q\}$, Equation (5.2) can be independently solved for each DOF, all subsequent equations will be developed for a SDOF model. Thus, the subscript i will be omitted from the terms previously defined. However, all equations and methods can be readily generalised to MDOF cases.

From Equations (5.1) and (5.2), q_k, the restoring force at time k, and its first derivative, $\dot{q}_k$, can be written:

$$q_k = -m(\ddot{v}_k + \ddot{x}_{g,k}) \tag{5.3}$$

$$\dot{q}_k = c_k \ddot{r}_k + k_k \dot{r}_k - a_k |\dot{r}_k| |q_k|^{n-1} q_k - b_k \dot{r}_k |q_k|^n \tag{5.4}$$

where the subscript k denotes values at time k. To further simplify the equations by reducing the number of unknowns to be identified from four (c, k, a, and b) to three (c, k, and d), following a similar procedure as in Equations (2.15)-(2.18), a new form of Equation (5.4) is defined:

$$\dot{q}_k = c_k \ddot{r}_k + k_k \dot{r}_k + d_k \dot{r}_k \left| q_k \right|^n \tag{5.5}$$

where

$$d_k = -\left[a_k sign\left(\dot{r}_k q_k\right) + b_k \right] = \begin{cases} -a_k - b_k & , \dot{r}_k q_k > 0 \\ -b_k & , \dot{r}_k q_k = 0 \\ a_k - b_k & , \dot{r}_k q_k < 0 \end{cases} \tag{5.6}$$

Similar to $\dot{r}_i(t)h_i(t)$ in Figure 2.4, over each period of the structure's motion, the term

$\dot{r}_k q_k$ in Equation (5.6) changes sign four times. Therefore, in a quarter of a period, this

equation yields the two independent linear equations required to determine a_k and b_k.

A finite difference approximation based on a third-order corrector method is

used to relate Equations (5.3) and (5.5) (Lin et al. 2001; Yang and Lin 2004):

$$q_k - q_{k-1} = \frac{\Delta t_k}{12} \left(5\dot{q}_k + 8\dot{q}_{k-1} - \dot{q}_{k-2} \right) \tag{5.7}$$

where Δt_k is the time step. This equation can be rewritten as a linear equation in terms of

the unknowns using Equations (5.3) and (5.5):

$$\phi_{1,k} c_k + \phi_{2,k} k_k + \phi_{3,k} d_k = y_k \tag{5.8}$$

where,

$$\begin{aligned}
y_k &= -m(\ddot{v}_k - \ddot{v}_{k-1} + \ddot{x}_{g,k} - \ddot{x}_{g,k-1}) \\
\phi_{1,k} &= 5\ddot{r}_k + 8\ddot{r}_{k-1} - \ddot{r}_{k-2} \\
\phi_{2,k} &= 5\dot{r}_k + 8\dot{r}_{k-1} - \dot{r}_{k-2} \\
\phi_{3,k} &= 5\dot{r}_k \left| q_k \right|^n + 8\dot{r}_{k-1} \left| q_{k-1} \right|^n - \dot{r}_{k-2} \left| q_{k-2} \right|^n
\end{aligned} \tag{5.9}$$

Equation (5.8) cannot be independently solved for three unique answers for c_k,

k_k, and d_k at each time step. Thus, more independent equations are needed over each

time step. The two stiffness and damping parameters have much slower dynamics

compared to the Bouc-Wen parameter, d_k. As was mentioned earlier, d_k changes sign

four times in every period of motion, while the two other parameters can reasonably be

considered fixed or to change much more slowly. This point suggests that, similar to

Section 3.4, over increasingly smaller time steps of Δt_l, the values c_k and k_k can be

assumed constant compared to the faster dynamics of d_k (Hann et al. 2009):

$$c(t) = c_k, \quad (k-1)\Delta t_k \leq t \leq k\Delta t_k, k = 1,...,m'$$
$$k(t) = k_k \quad (k-1)\Delta t_k \leq t \leq k\Delta t_k, k = 1,...,m'$$
$$d(t) = d_l \quad (l-1)\Delta t_l \leq t \leq l\Delta t_l, \quad l = 1,...,n' \quad (5.10)$$
$$\Delta t_k = p\Delta t_l \qquad p > 1$$

where m' and n' are the number of intervals over which the piecewise time-varying

functions, $c(t)$, $k(t)$, and $d(t)$ are defined. Further, Δt_k and Δt_l are user-selected intervals

over which piecewise constant behaviour is reasonable. For ease of fitting, similar to

Section 3.4, p is assumed to be an integer value greater than one. In this way, p values

of d_l are fitted alongside every single value of c_k and k_k as shown in Figure 5.1 for the

case of p=3.
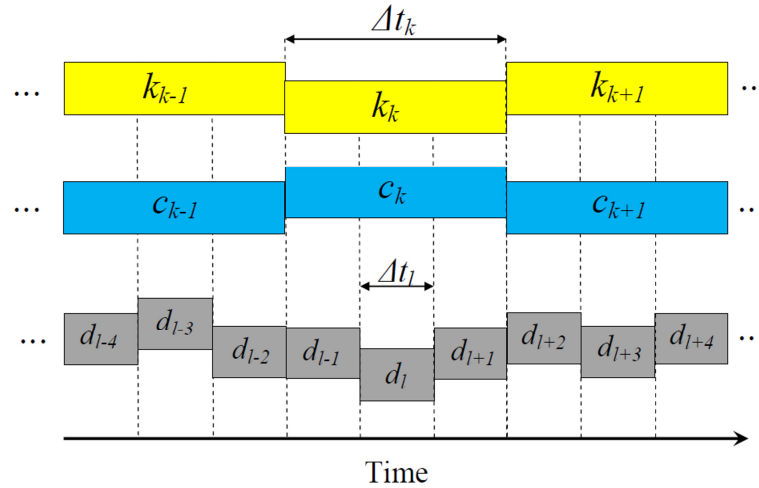
Figure 5.1. Time variation of the fitted parameters for p=3

Identification of the unknown parameters, c_k, k_k, and d_l requires a system of

linear equations (at least three), each in the form of Equation (5.8), at each time step.

For the example of Figure 5.1, three values of Δt_i $(p' = 3)$ could be chosen in each

time interval Δt_l. This choice will give nine equations for each time interval Δt_k with

five unknowns, defined by the system:

$$\mathbf{A_k} \cdot \{x\}_k = \{y\}_k \qquad (5.11)$$

where

$$\mathbf{A_k} = \begin{bmatrix} \phi_{1,i} & \phi_{2,i} & \phi_{3,i} & 0 & 0 \\ \phi_{1,i-1} & \phi_{2,i-1} & \phi_{3,i-1} & 0 & 0 \\ \phi_{1,i-2} & \phi_{2,i-2} & \phi_{3,i-2} & 0 & 0 \\ \phi_{1,i-3} & \phi_{2,i-3} & 0 & \phi_{3,i-3} & 0 \\ \phi_{1,i-4} & \phi_{2,i-4} & 0 & \phi_{3,i-4} & 0 \\ \phi_{1,i-5} & \phi_{2,i-5} & 0 & \phi_{3,i-5} & 0 \\ \phi_{1,i-6} & \phi_{2,i-6} & 0 & 0 & \phi_{3,i-6} \\ \phi_{1,i-7} & \phi_{2,i-7} & 0 & 0 & \phi_{3,i-7} \\ \phi_{1,i-8} & \phi_{2,i-8} & 0 & 0 & \phi_{3,i-8} \end{bmatrix}, \quad \begin{array}{l} i = 9,10,...,9m' \\ k = 1,...,m' \end{array} \tag{5.12}$$

$$\{x\}_k = \begin{Bmatrix} c_k \\ k_k \\ d_l \\ d_{l-1} \\ d_{l-2} \end{Bmatrix}, \quad \begin{array}{l} k = 1,...,m' \\ l = 3,4,...,3m' \end{array} \tag{5.13}$$

$$\{y\}_k = \begin{Bmatrix} y_i \\ y_{i-1} \\ y_{i-2} \\ y_{i-3} \\ y_{i-4} \\ y_{i-5} \\ y_{i-6} \\ y_{i-7} \\ y_{i-8} \end{Bmatrix}, \quad \begin{array}{l} k = 1,...,m' \\ i = 9,10,...,9m' \end{array} \tag{5.14}$$

Further, $\phi_{1-3,i}, i = 1,...,9m'$ and $y_i, i = 1,...,9m'$ are defined from Equation (5.9) at each time step $\Delta t_i, i = 1,...,9m'$. The least squares solution of the matrix Equation (5.11) yields the unknown vector $\{x\}_k$.

The overall RT-SHM algorithm developed is summarised in Figure 5.2. The two Bouc-Wen model parameters, a and b of Equation (5.2), if needed, can then be either calculated at smaller time steps using a similar fast and slow dynamics separation approach, or determined using Equations (5.3) and (5.6) at each quarter of a period of the structure's motion. The overall approach thus identifies parameters within quarter of a response cycle, which should be more than adequate for the application envisioned.
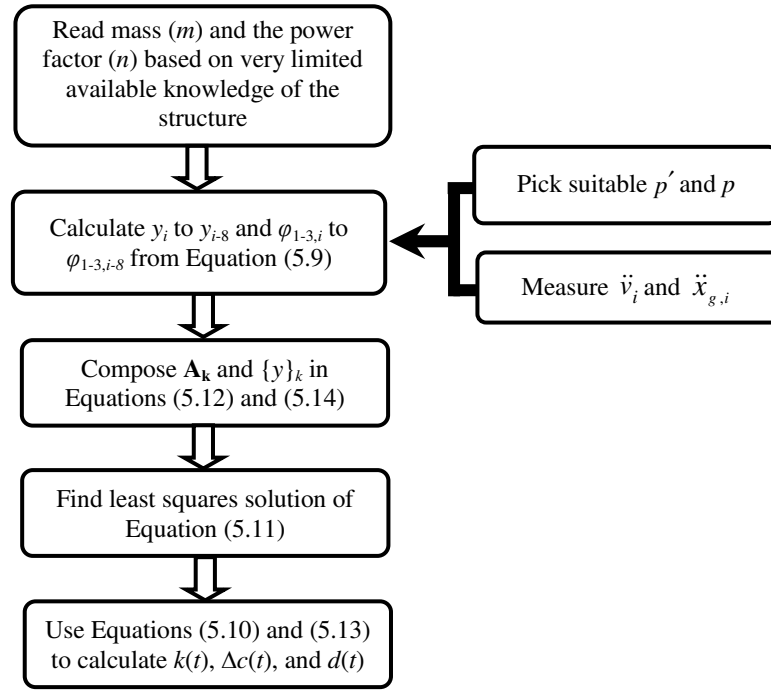
Figure 5.2. Flowchart of one time step of the RT-SHM method developed for nonlinear hysteretic structures using a fast and slow dynamics separation technique

5.4. Simulation proof-of-concept structure

The simulation proof-of-concept structure is a SDOF nonlinear hysteretic structure with the following parametric values similar to (Lin et al. 2001; Yang and Lin 2004): m=125.53 kg, c=0.07 kN.s/m, k=24.2 kN/m, a=0.2, b=0.1, and n=2. The first fundamental natural frequency is 2.21 Hz, and the damping ratio in the same mode is 2%. The structure is subjected to the Northridge earthquake with PGA of 0.617 g (EQ11 in Table 2-1).

Nonlinear dynamic analysis is performed in MATLAB® using the predefined parameters and the Newmark-β integration method to represent the nonlinear hysteretic behaviour of the structure. The simulated structural responses from MATLAB® are then used to provide proof-of-concept inputs to the method and to thus quantify the accuracy of the identified parameters, stiffness, damping, and the combined Bouc-Wen parameter, d.

The structural identification and health monitoring algorithm developed is also implemented in MATLAB® for the identification process under the Northridge earthquake. Further, to evaluate the performance of the proposed SHM method under harmonic single frequency excitations, the simulation proof-of-concept structure is subjected to a harmonic excitation of amplitude 0.2 g and frequency of 2.21 Hz. This frequency is chosen to match the natural frequency of the simulated structure and cause instability. This harmonic excitation case is a worst-case approach, but also is a good representative of the loads seen in marine structures. Finally, to assess the robustness of the proposed method over different ground motions, the simulated structure is subjected to the suite of 20 different ground motions in Table 2-1.

Table 5-1. Damage patterns used in the simulation

Damage pattern #	Description
1	20% reduction in stiffness at the 5 second mark
2	20% reduction in both stiffness and damping at the 5 second mark
3	20% reduction in the Bouc-Wen model parameter (d) at the 5 second mark
4	20% reduction in all three, stiffness, damping, and the Bouc-Wen model parameter at the 5 second mark

The simulated structure is also subjected to four different worst-case, sudden damage scenarios, defined in Table 5-1. The goal is to evaluate the proposed algorithm's performance in damage identification over a range of limit cases and possibilities. The damage cases are applied to the structure at the 5-second mark. Simulation-derived data is recorded at 4 kHz, and results are smoothened using a backward moving average filter in real time to cancel the effect of very ill-conditioned coefficient matrices of $\mathbf{A_k}$ in Equation (5.11).

5.5.   Results

Figure 5.3 shows the nonlinear response of the SDOF proof-of-concept structure undergoing the Northridge earthquake. The figure clearly shows that the case-study structure is highly nonlinear and has a permanent residual deformation after the earthquake. As shown in Figure 5.4a, the algorithm is very capable of identifying the structural and Bouc-Wen model parameters, c, k, and d, in real time. In this figure, in the third graph from the top, the actual upper (a-b) and lower limits ($-a$-b) of the value of d, are shown for easier comparison, instead of its actual as-modelled values.
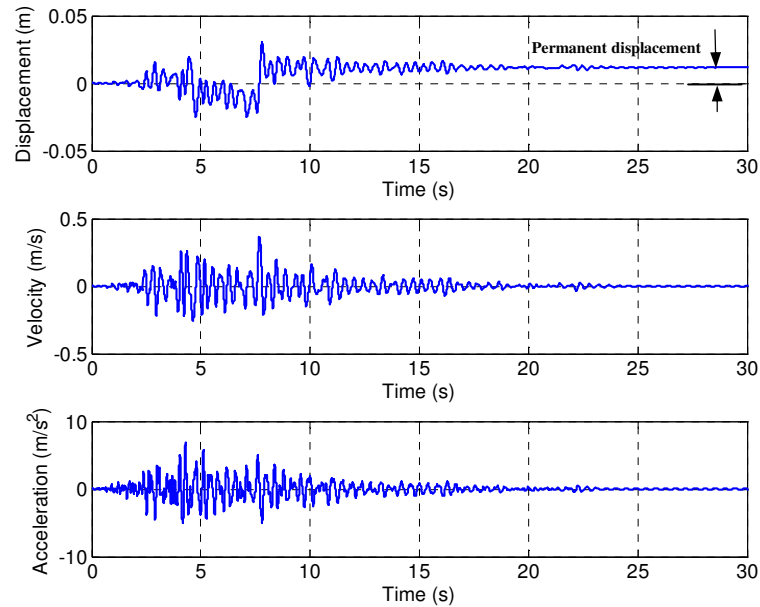
Figure 5.3. Responses of the simulated structure subjected to the Northridge earthquake

The maximum error in the identification process for the entire record after the 2-second mark ($t \geq 2$ s) is 3.04% of the actual as-modelled value for stiffness and 2.35% for damping for the simulated structure under the Northridge earthquake. These error values are well within modelling and construction errors. Identification results for the first two seconds were excluded from the error evaluation process to ignore the effect of incorrect initial values chosen for the parameters.

To further evaluate the accuracy of the RT-SHM algorithm developed, the

identified values were used to recalculate the restoring forces. The result is shown in Figure 5.4b. As the figure shows, the actual and identified restoring forces are almost identical. Figure 5.5 shows the same results for the sinusoidal excitation. The maximum error in the identified values is 1.33% of the actual as-modelled value for k and 5.25% for c when the simulated structure is subjected to the harmonic excitation. Again, these values are quite small next to modelling errors or construction variability.

(a)   (b)
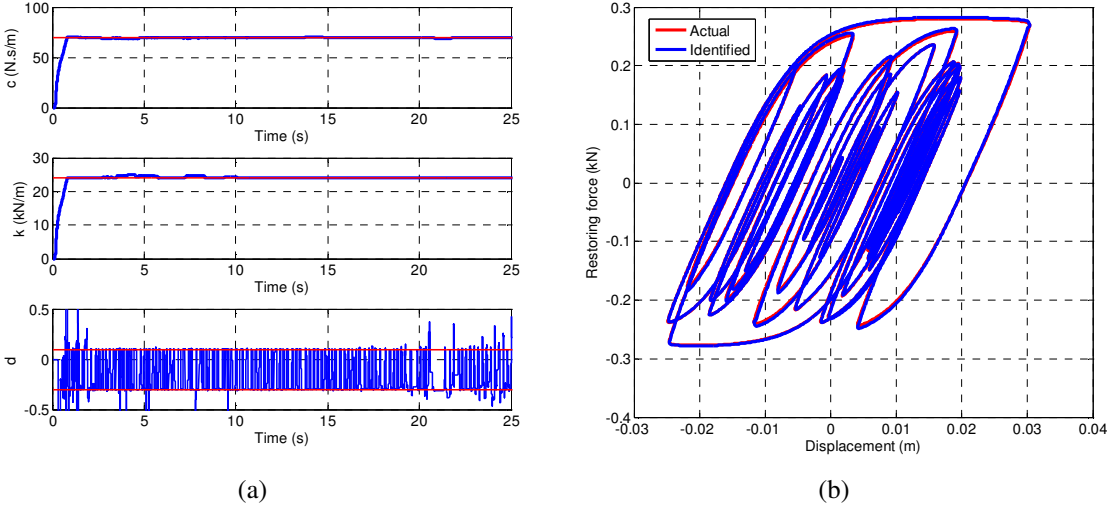
Figure 5.4. a) Identified structural and Bouc-Wen model parameters and b) hysteresis loops of the simulated structure subjected to the Northridge earthquake

(a)   (b)
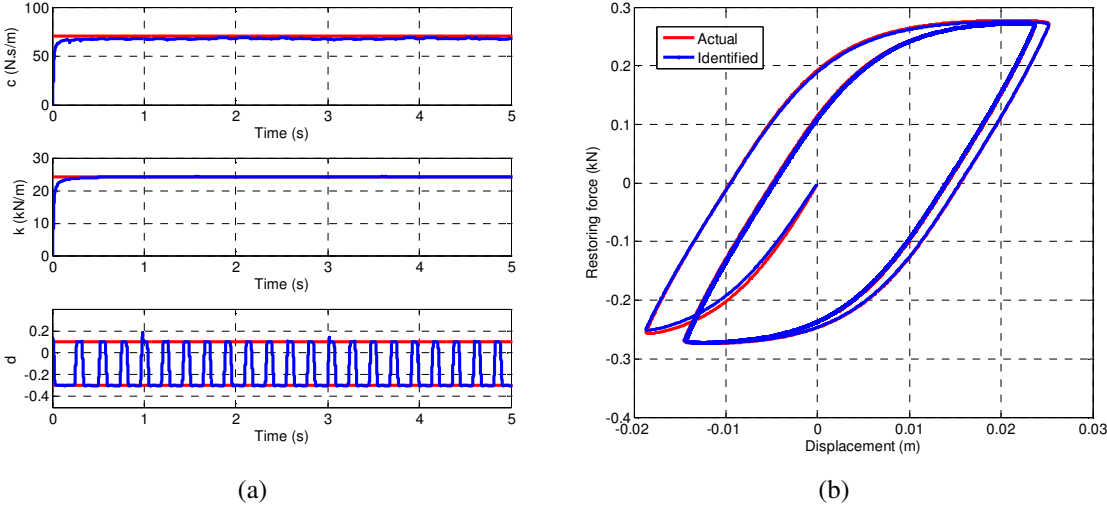
Figure 5.5. a) Identified structural and Bouc-Wen model parameters and b) hysteresis loops of the simulated structure subjected to a harmonic excitation of amplitude 0.2 g and frequency of 2.21 Hz

Figures 5.6 and 5.7 show that the proposed SHM algorithm is robust to different input excitations. The maximum error in the identification process is less than 7.12% (mean=2.67%, median=1.88%, and the 5th-95th inter-percentile=6.78%) for stiffness and 7.19% (mean= 4.3%, median= 4.2%, and the 5th-95th inter-percentile=4.29%) for damping for all the ground motions in Table 2-1. Differences in the maximum error values for the different ground motions used are due to differences in the structural responses. These differences affect the coefficient matrix, $\mathbf{A_k}$, in Equation (5.12) and sometimes result in less accurate least squares solutions for this equation.
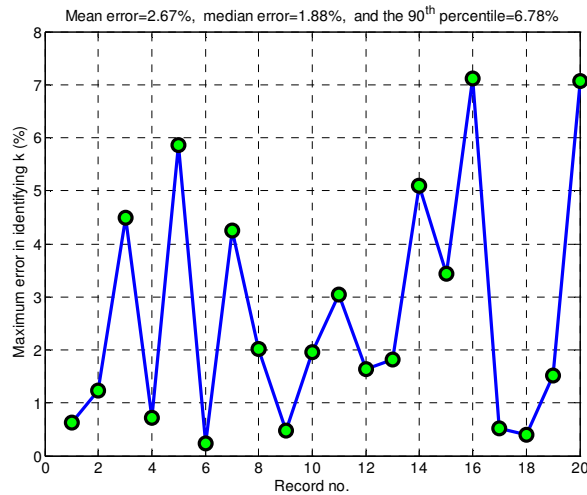
Figure 5.6. Maximum error in stiffness identification using the proposed algorithm when the case-study structure is subjected to the 20 different ground motion records in Table 2-1 (Mean error = 2.67%, median error = 1.88%, and the 5th-95th inter-percentile = 6.78%)
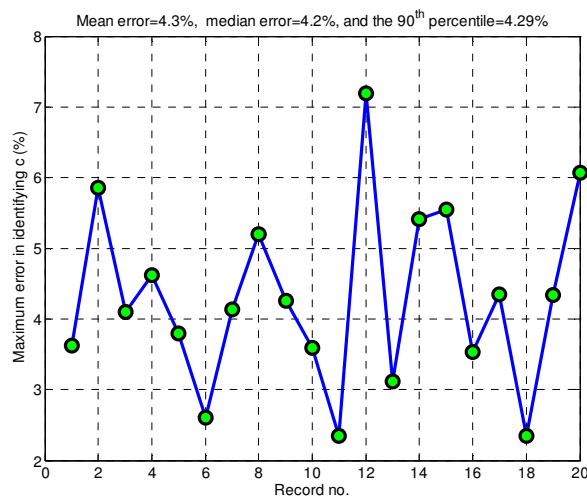
Figure 5.7. Maximum error in damping factor identification using the proposed algorithm when the case-study structure is subjected to the 20 different ground motion records in Table 2-1 (Mean error = 4.3%, median error = 4.2%, and the 5th-95th inter-percentile = 4.29%)

The SHM results for the four different damage patterns in Table 5-1 are shown in Figures 5.8 to 5.11. As these figures show, the RT-SHM approach proposed is readily able to identify damage in all four different damage scenarios with the worst-case abrupt change in the structural parameters. Identified and actual hysteresis loops for the last damage pattern (No. 4) are also shown in Figure 5.11b. As this figure shows, even for the worst damage pattern of the four in Table 5-1, with sudden changes in all the three parameters, the identified hysteresis loops are in a very good agreement with the actual as-modelled loops.
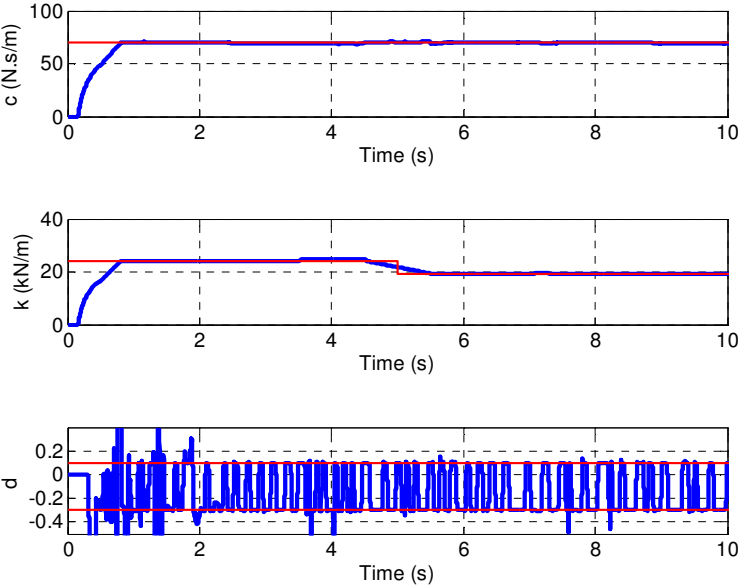
Figure 5.8. Identified structural and Bouc-Wen model parameters of the simulated structure subjected to the Northridge earthquake and damage pattern 1 in Table 5-1
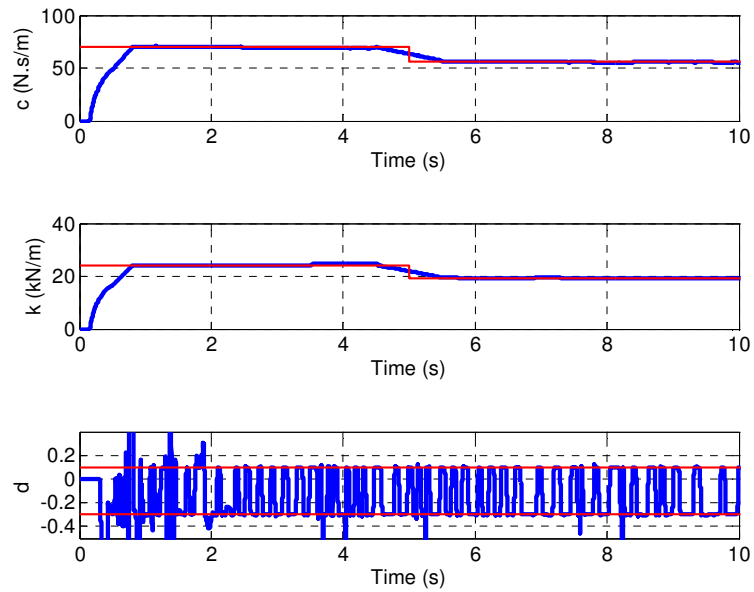
Figure 5.9. Identified structural and Bouc-Wen model parameters of the simulated structure subjected to the Northridge earthquake and damage pattern 2 in Table 5-1
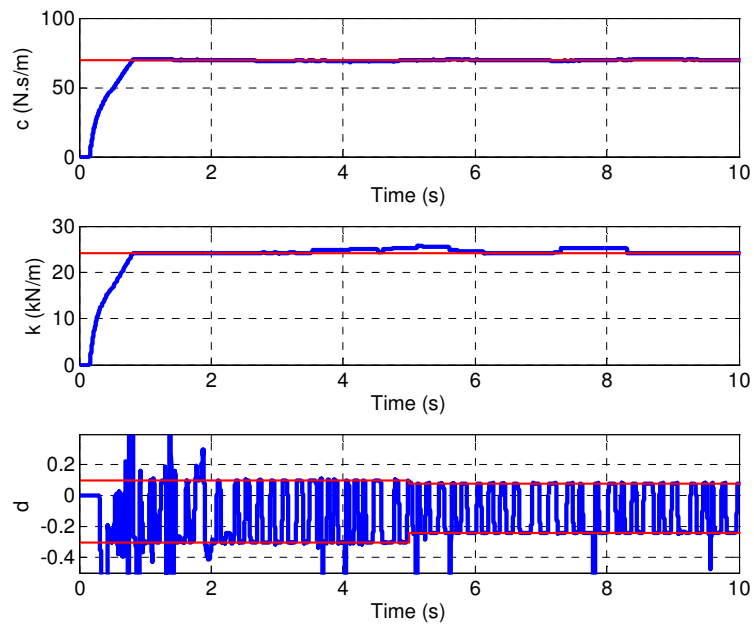
Figure 5.10. Identified structural and Bouc-Wen model parameters of the simulated structure subjected to the Northridge earthquake and damage pattern 3 in Table 5-1
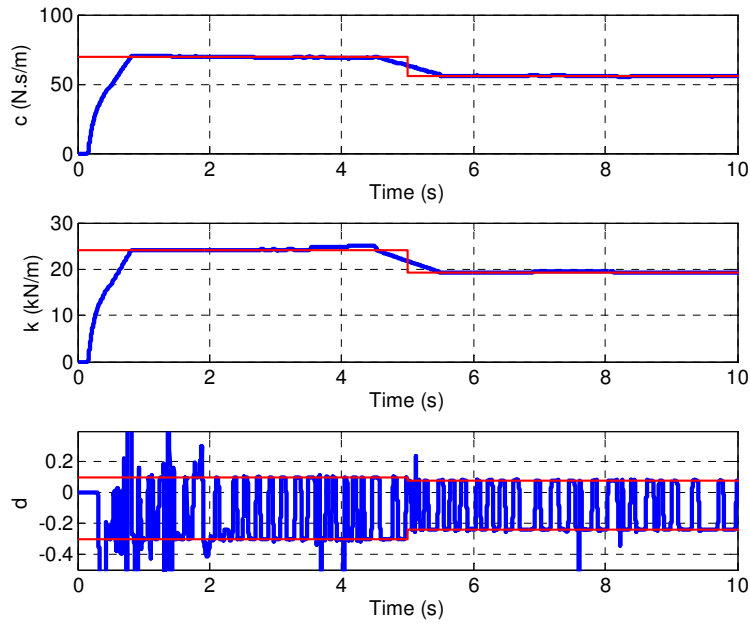
(a)
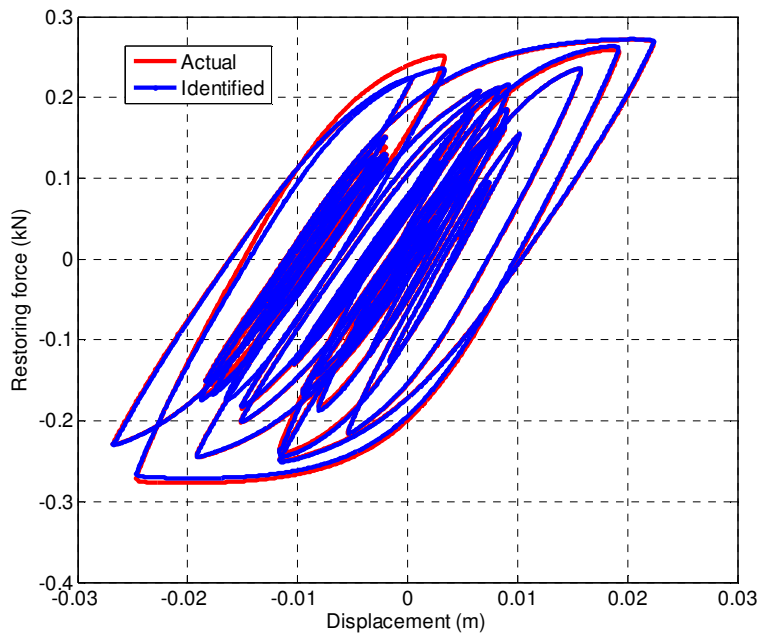
(b)

Figure 5.11. a) Identified structural and Bouc-Wen model parameters and b) hysteresis loops of the simulated structure subjected to the Northridge earthquake and damage pattern 4 in Table 5-1

The SHM results presented in this chapter are functionally equivalent to real-time results. Specifically, using MATLAB$^®$, identification of the three stiffness, damping and the combined Bouc-Wen model parameters takes ~1.37e-5 s for each piecewise step of Δt_i=2.5e-4 s (4 kHz sampling rate) on a 3.16 GHz Intel$^®$ dual-core desktop machine. This execution time is only ~5.5% of the smallest identification time step used (Δt_i). Coding in more sophisticated programming languages, such as C, typically reduces computational time by 10-100×, or more, compared to MATLAB$^®$. In addition, the identification process at each time step only relies on the prior time step values. Hence, the proposed algorithm can be readily used as an on-line SHM method, and is much more computationally-efficient than many of its real-time competitors, such as (Sato and Qi 1998; Loh et al. 2000; Li et al. 2004a).

The method developed remains to be experimentally validated and further tested, particularly against noise-contaminated input responses. However, a range of highly-effective noise-filtering methods that are computationally-efficient are readily available to manage this issue (Ifeachor and Jervis 1993; Sayed 2003). In addition, the best nonlinear model that can represent the structure's nonlinear yielding behaviour is sometimes unknown or is not necessarily of a Bouc-Wen type. In such cases, actual and modelled structural behaviours would not be perfectly the same. Therefore, the effect of different baseline models on the identification results need to be evaluated before implementation on a real structure. However, the method proposed is definitely a first step forward and has significant potential benefits in assessing structural safety and serviceability after major events, such as earthquakes, and provides the input data required for structural control methods with damage mitigation or avoidance purposes.

5.6.   Summary

SHM is the process of identification, localisation, and quantification of structural damage due to external loads, such as an earthquake. SHM results simplify and automate typical visual or localised experimental approaches and enable more informed structural safety assessment and post-event retrofit. On-line SHM is of particular interest for rapid safety assessment by owners and civil defence authorities, particularly in the immediate aftermath of an event. It can also be used during an event to inform active control systems to further avoid or mitigate damage.

This chapter presented an on-line SHM algorithm for identification and monitoring of nonlinear hysteretic structures. It separates fast and slow dynamics and uses robust PLLSQ fitting to identify key structural parameters including stiffness, damping, and the Bouc-Wen hysteretic model parameters in real time. These parameters are directly related to well-recognised damage metrics.

Moreover, the RT-SHM method developed does not require structural displacement measurements, which are typically very difficult to acquire or reasonably estimate. Estimation of displacement by double integration of acceleration measurements is also subject to drift and error, which needs to be corrected using additional displacement data. Therefore, this great advantage of the algorithm developed over many of its competitors makes it more amenable in the field.

Proof-of-method simulations of a realistic nonlinear case-study structure, subjected to a suite of 20 different ground motions, show that the algorithm is well-capable of identifying structural parameters to within 2.7% and 4.3% of the actual as-modelled values for stiffness and damping, respectively. Results for various combinations of changes (damage) in structural parameters also show that the algorithm performs well in tracking the changes in real time. The RT-SHM approach developed

remains to be further studied for noise effect and shorter response times before experimental validation and implementation by the profession.

CHAPTER 6

Line-scan based seismic displacement measurement

6.1. Introduction

As discussed in Chapter 1, SHM is a multi-staged process that includes defining properties of the structure that need to be monitored, instrumentation and data acquisition, identification of damage-sensitive properties to distinguish between damaged and undamaged structures, and, finally, determination of whether the changes observed in the selected features used to identify damage are statistically significant (Sohn et al. 2004). The data collection stage plays a key role in the SHM process by providing the required inputs. Limitations on acquiring the necessary input data have

made the implementation of many existing SHM algorithms difficult or impossible. In particular, most SHM and control algorithms for damage detection and mitigation, including the methods developed in Chapters 2 and 3, require continuous monitoring of dynamic responses: acceleration, velocity, and displacement (Loh et al. 2000; Hann et al. 2009; Nayyerloo et al. 2011). Acceleration can be easily measured using ordinary accelerometers. However, velocity and displacement are typically difficult to capture, especially at the high enough sampling rate required by these algorithms relative to the structural frequencies. Velocity and displacement are usually estimated by integration of measured acceleration. However, the integrated results are subject to drift and error, which needs to be corrected using additional data from an independent, typically lower sampling rate, displacement sensor (Li et al. 2004b).

Displacement sensors can be categorized into two main groups: contact and non-contact. Contact sensors, such as Linear Variable Differential Transducers (LVDTs), piezoelectric (PZT) sensors, or optical fibre sensors are not always non-invasive and require extensive sensor networking to measure structural displacements in multiple directions. Moreover, contact sensors may architecturally interfere with light model structures, or in the case of optical fibre sensors may involve expensive optical spectrum analyzers (Lee 2003).

In the non-contact group, Laser Doppler Vibrometers (LDVs), GPS-based sensors, and computer vision based techniques are common methods with a wide range of applications. LDVs provide high bandwidth and highly accurate displacement and velocity data, but only in one direction and at relatively high cost (Lee et al. 2007). GPS-based and vision-based sensors can provide displacement data in multiple directions and require less networking compared to LDVs and contact sensors. Nonetheless, each has its own problems. GPS-based systems are low-rate and very low-

resolution for precision applications (Li et al. 2004b; Kijewski-Correa et al. 2006). Vision-based methods can be very high-resolution and high-rate depending on sampling rate and resolution of the acquired frames. However, the increasing volume of image data to be processed significantly increases the processing time and computational complexity, making it, at least at this time, unsuitable for cost-effective real-time applications.

Visual techniques are also quite flexible and can be easily adapted to different applications. Light-based motion tracking of buildings subjected to earthquake motions or equipment inside buildings proposed by Hutchinson et al. (2005; 2006) is one application. Three-dimensional (3D) structural displacement measurement with multiple digital cameras is a second (Chang and Ji 2007). Others include, non-target stereo-vision spatio-temporal response measurement of line-like structures (Ji and Chang 2008), digital image correlation based stereovision for 3D displacement measurement (Orteu 2009), and applying edge detection technique with sub-pixel accuracy for structural displacement measurement (Fu and Moosa 2002).

Recently, Lim et al. developed a method that uses a single line-scan camera with a printed pattern to measure foundation pile movements in multiple directions (Lim and Lim 2008). Using line-scan cameras significantly decreases the size and pixel volume of the acquired frames. It thus enables high-speed displacement measurement without the need for very expensive, real-time hardware. However, its resolution is limited for larger displacements, which is particularly a problem where the expected motions cover a wide range of scales, such as seen in seismic response motions. Further, no calibration procedure was proposed in the work by Lim et al. to ensure that the assumptions made in developing the line-scan based method proposed are fully met. However, if these issues can be solved, line-scan cameras offer a high-resolution, high-rate displacement

sensor platform.

This chapter extends and empirically evaluates the efficacy of the proposed line-scan based displacement measurement method by Lim et al. In particular, the method is extended to improve resolution, especially for large seismic events with a wide range of displacement level. This change also ensures maximum resolution across a range of displacements, as a result. Thus, both larger and smaller displacements have equal resolution, which was not the case for the original method.

Further, as the accuracy of the proposed measurement method depends directly on the camera-pattern calibration, a simple and easy-to-implement calibration procedure is proposed that ensures accuracy of the measurement results. Chapter 7 addresses the impact of the correctness or any error of the printed pattern dimensions utilised by this sensor and method on the measurement results. This latter analysis thus quantifies the level of confidence in the measured displacements as a function of inaccuracy in the pattern dimensions at the heart of this approach.

6.2.   Line-scan displacement measurement

6.2.1. Method of Lim et al.

Lim et al. proposed a vision-based displacement measurement method using one high-speed line-scan camera with the special pattern shown in Figure 6.1 to capture vertical, horizontal and rotational movements of any point on the pattern. The pattern is a printed array of black and white triangles and is posted on a desired spot on the structure. The camera is pointed at the array so that the scan line intersects the pattern lines, as shown schematically in Figure 6.1.
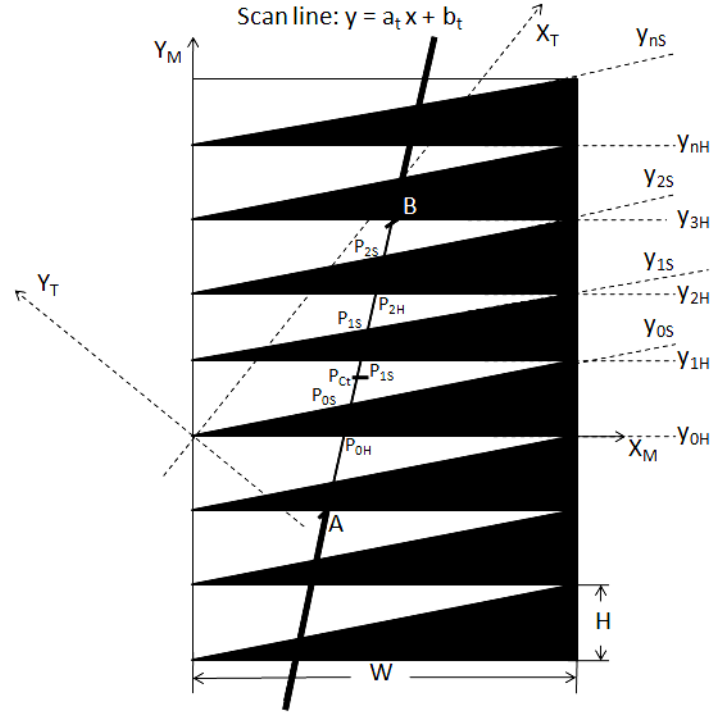
Figure 6.1. Special pattern enables vertical, horizontal, and rotational displacement measurement using only one line-scan camera (Lim and Lim 2008).

The scan line in Figure 6.1 is defined $y = a_t x + b_t$ in the $\{T\}$ coordinate system, which has been rotated by $45°$ with respect to the original coordinate system, $\{M\}$. It thus intersects the normal and slanting lines of the pattern at P_{nH} and P_{nS} ($n=0,1,2,\ldots$), respectively. These intersection points can be written in terms of the known pattern dimensions, H and W, and the unknown scan line parameters, a_t and b_t. At each time step or image, the Euclidian distance between any two consecutive intersection points can be measured in pixels. Therefore, calculating the ratios of two consecutive white to black (or black to white) distances leaves two independent equations in the unknowns a_t and b_t:

$$a_t = \frac{(L_n - L_m)W + \{L_m - L_n + (L_m +1)(L_n +1)(n-m)\}H}{(L_m - L_n)W + \{L_m - L_n + (L_m +1)(L_n +1)(n-m)\}H} \tag{6.1}$$

$$b_t = \frac{\sqrt{2}WH\{m(L_m +1)-n(L_n +1)\}}{(L_m - L_n)W + \{L_m - L_n + (L_m +1)(L_n +1)(n-m)\}H} \tag{6.2}$$

where H and W are the height and the width of a triangle in the pattern in Figure 6.1,

respectively, and L_n ($n=0,1,2,...$) or L_m ($m=0,1,2,...$) are ratios between two consecutive black and white distances in each frame of the line-scan image and are assessed directly from the image. Using ratios of the distances, instead of the distances themselves, makes calibration of measurement results in pixels to the FOV in meters easier. Using Equations (6.1) and (6.2), the centre of the scan line, or in other words, the centre of the camera's FOV can be written in terms of a_t and b_t using coordinates of intersection points adjacent to the centre point:

$$P_{C_t} = \left(\frac{-b_t + \sqrt{2}HR_t}{a_t + 1}, \frac{b_t + \sqrt{2}a_t HR_t}{a_t + 1} \right)$$ (6.3)

where, R_t, as illustrated in Figure 6.2, is the ratio of the distance of the centre point to the closest adjacent intersection point between the scan line and the normal pattern lines over the distance between the two consecutive intersection points between the normal lines and the scan line that passes through the centre point:

$$R_t = \frac{D_{1H} - D_{Centre}}{D_{1H} - D_{0H}}$$ (6.4)
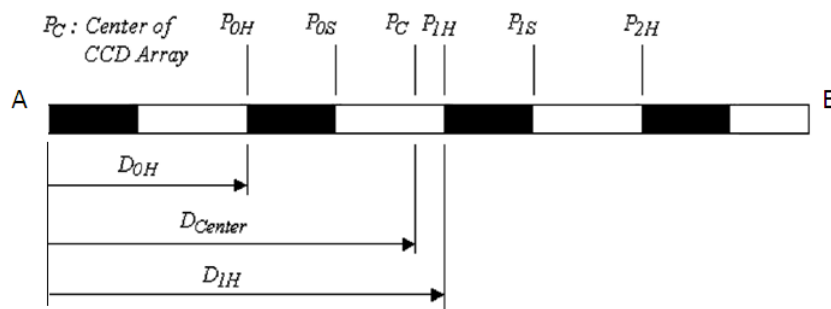
Figure 6.2. R_t is the distance between P_{1H} and P_C over the distance between P_{1H} and P_{0H} (Lim and Lim 2008)

Transferring the movements from $\{T\}$ to a coordinate system with the scan line as one of the axes represents a linear transformation of the pattern. Rotational movements of the pattern can then be calculated as the difference between inverse tangents of a_t for two consecutive captured frames:

$$\begin{pmatrix} \Delta x_t \\ \Delta y_t \end{pmatrix} = \begin{pmatrix} \sin\theta_0 & -\cos\theta_0 \\ \cos\theta_0 & \sin\theta_0 \end{pmatrix} \left(P_{C_0} - P_{C_t} \right) \qquad (6.5)$$

$$\Delta\theta_t = \tan^{-1} a_t - \tan^{-1} a_0 \qquad (6.6)$$

where Δx_t, Δy_t, and $\Delta\theta_t$ are linear movements of the pattern parallel to the scan line, linear movements perpendicular to the scan line, and rotations of the pattern about the centre of the scan line, respectively. Moreover, all the parameters with subscript "0" denote the initial values.

6.2.2. Software design and edge tracking

The image processing provides the time-varying coordinates of the intersection points between the scan line and the pattern lines. Simply, it detects the edges from the white to black and black to white regions. This detection can be done using a relative intensity threshold level to detect location of large changes in the intensity of pixels at each acquired grayscale image from the camera. Following edge detection, edges in the first frame can be tracked to detect relative displacements of the target with respect to its initial position. As the line-scan image acquisition is very fast (up to 20+ kHz) compared to movements of the target, the next position of each edge falls within a small distance to its previous location. Therefore, the next position of each edge can be sought in a small bounded area around its previous position (Lim and Lim 2008). Hence, the new location of an edge can be found by using binary search algorithm (Sedgewick 1997) in the bounded area defined. This bounded area should not be less than maximum estimated movement of the target at each measurement time step on either side of the edge.

This edge tracking algorithm requires a sufficiently wide FOV depending on the maximum likely displacements that may occur. Tracking each edge by simply locating the edge using pixel numbers in each frame requires the edges to always remain in the

FOV of the camera. To ensure that this condition is met, the FOV of the camera must be expanded so that it encompasses all possible locations that the edges may move to. During this process of "zooming-out", the number of pixels in the Charge-Coupled Device (CCD) array remains constant (constant camera resolution), and as a result the number of pixels per millimetres of movement of the target or the output measurement resolution decreases. Hence, if the likely responses span a range of displacement scales, resolution at small motions is lost to enable large motion measurement. Resolving this issue enables using low-cost low-resolution line-scan cameras for structural displacement measurement using the method of Lim et al., as well as improving the overall method.

The resolution problem arising from the edge tracking algorithm can be solved by dynamically altering which edges are being tracked after time zero. The new algorithm renames edges when they cross the centre point of the CCD array such that the required edges for displacement measurement are always centred around the CCD array centre pixel. To this end, offset factors are stored and updated with each renaming to ensure that data is continuous. Therefore, the size of the FOV required to capture the motions is fixed regardless of the size of the motions, and it is a function of the pattern dimensions only. Thus, the resolution is maximised and also, as a result, fixed for all displacement scales sensed.

The new edge tracking method developed is illustrated in Figure 6.3. Six edges, three on the right and three on the left-hand side of the centre point of the CCD array, should be detected in each captured image and tracked over different images to provide the data required for displacement measurement using Lim et al. method. These edges can be simply detected using relative intensity threshold method and tracked using their pixel values. However, when an edge crosses the centre point, an undesired shift in the

edge position values recorded occurs. As a result, the three edges on the left or right-hand side of the centre point will not be the same edges being tracked over the previous frames.

This shift is shown in Figure 6.3 by renaming the edges at t_2, when edge 3 crosses the centre point and becomes 3' instead of 2'. Therefore, at edge renaming time steps, offset or shift values (S_{1-5}) should be stored and added to the edge pixel values for the actual position of each edge. For example, actual position of edge 3 after it crosses the centre point of the CCD array is calculated by adding S_3 to the new position of edge 3 detected (3') to yield 2', the actual position of edge 3 at t_2. Time steps at which such shifting occurs can be detected by tracking the change in the sign of the first derivative of distances between the centre point and the first edge on the right or left-hand side of the centre point in each image. The dotted curve in Figure 6.3 shows this change for the case of using the first edge on the right-hand side of the centre point.
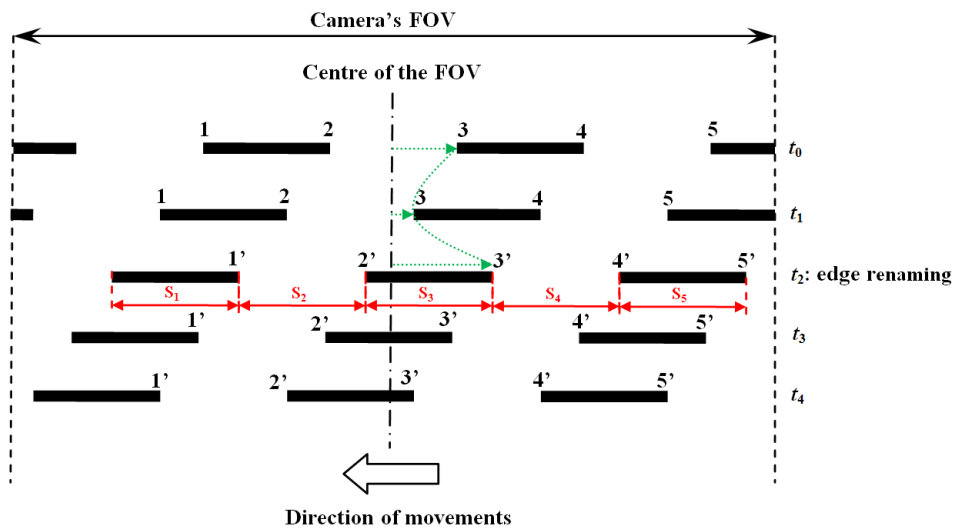
Figure 6.3. The new edge tracking technique proposed.

Figure 6.4 shows the edges tracked during a linear movement of a target in two opposite directions using the direct tracking technique by pixel position of the edges and the new edge tracking algorithm proposed. The discontinuities in Figure 6.4b show the time step marks at which an edge renaming occurs. The figure clearly shows that the

tracked edges span a smaller section of the CCD array than edges tracked by the direct method. Hence, resolution and accuracy are maintained or improved with this novel extension to the method.
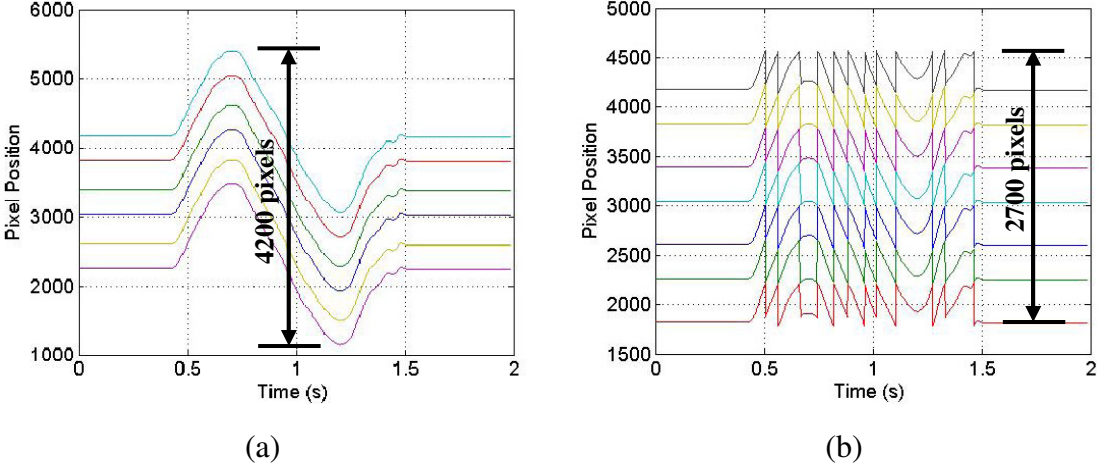
Figure 6.4. Position of the tracked edges, a) when the edges are simply tracked by their pixel position and b) when the proposed edge tracking algorithm is used

6.2.3. Experimental hardware design

Main components of the image acquisition and processing system are introduced in Table 6-1. One of the main components in the displacement measurement chain is the line-scan camera. Line-scan cameras scan a single-pixel-width digital imaging sensor at very high speed. Therefore, the images are only one pixel wide. High-speed line-scan cameras with line rates as high as 23 kHz and longitudinal resolutions in the order of 12k pixels are now commercially available (Teledyne DALSA Corp. 2011). Such cameras provide high resolution and high speed at the same time, which is critical for real-time applications.

Consider a black dot moving against a white background on a linear path in the FOV of the camera. The line-scan camera sees only a moving darker pixel over a series of images, as illustrated in Figure 6.5. Calibrating these pixels to the FOV in meters offers a displacement measurement.

Table 6-1. Specifications of the measurement set-up

Item	Description	
Camera	Teledyne DALSA P2-23-08K40 (Teledyne DALSA Corp. 2008b)	
	Maximum line rate (kHz)	9.3
	Pixel size (μm)	7×7
	Resolution (pixel)	8192
Lens	Schneider Componon-S 4.0/80 (Schneider Kreuznach Corp. 2010) with focusing mount and accessories	
Frame grabber board	National Instruments PCIe-1430 (National Instruments Corp. 2006)	
Light source	Philips MASTERLine 111 halogen reflector lamp 60W 12V 8D (Philips Corp. 2011)	
Host and target PCs	Intel® Core™ 2 Duo CPU 2.66 GHz	
	3.24 GB RAM	
	100 GB HDD	
	LabVIEW™ real-time operating system compatible LAN card	
Image acquisition and processing software	LabVIEW™ 8.5 and LabVIEW™ real-time operating system (LabVIEW™ RTOS)	

(a)   (b)   (c)
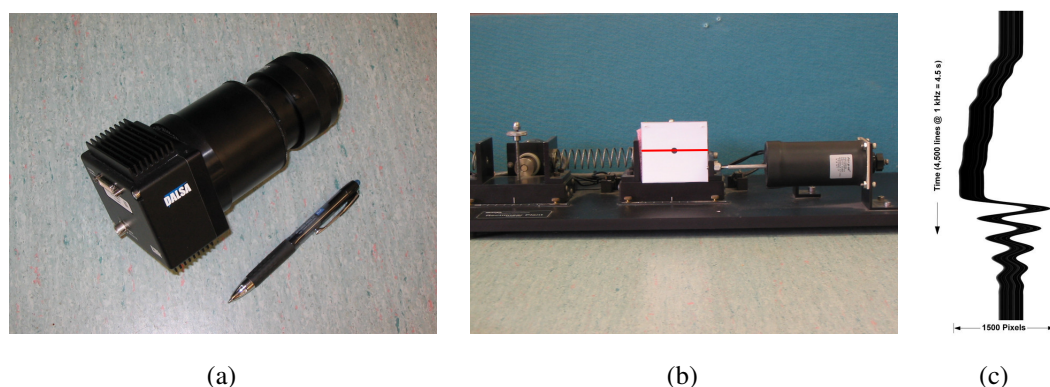
Figure 6.5. a) Line-scan camera used in this study, b) a linear mass-spring-damper system with a printed pattern (a black dot on a white background) posted on the mass (the red line on the pattern shows the FOV of the camera), and c) what the line-scan camera sees over several frames

The light intensity required to capture useful images depends on factors such as the surface roughness, nature, speed, and spectral characteristics of the target being imaged, also on exposure time of the CCD array of the camera (image acquisition rate), light source characteristics, environmental and acquisition system specifications, and more (Teledyne DALSA Corp. 2008a). Further, higher image acquisition rates typically require higher illumination intensities, because at high sampling rates, the CCD array is exposed to light for a shorter period and thus less amount of light is captured. AC light

131

sources are also typically not suitable for line-scan displacement measurement due to fluctuations in the light intensity caused by the alternating nature of the applied current. Therefore, linear LED light sources or Halogen projectors are recommended for the application of this thesis.

Figure 6.6 shows the data flow in the displacement measurement system. The image acquisition and processing code is written in LabVIEW™ on a host PC for real-time execution. The target PC runs under LabVIEW™ real-time operating system (RTOS) to make it dedicated to the image acquisition and processing tasks, to enable high sampling rates. The line-scan camera is connected to a frame grabber board installed on the target PC. This card enables the direct transferring of a high volume of image data to the target PC hard disk drive (HDD). The image processing is performed in real time, but results can be retrieved from the target PC for further processing either after the acquisition process or in real time while it is being performed. Communication through the server makes remote measurement possible.

| line-scan camera | Frame grabber board | Target computer | server | host computer |
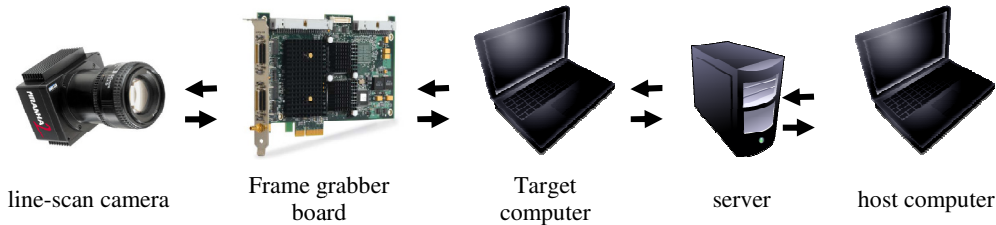
Figure 6.6. Data flowchart of the displacement measurement system (pictures and icons from www.teledynedalsa.com, www.ni.com, and www.iconarchive.com)

6.2.4. Measurement resolution and speed

System settings, such as the number of active camera pixels, FOV, lens magnification, geometrical configurations, and frame rate can be changed to meet different application requirements:

$$r = \frac{FOV}{N} \tag{6.7}$$

$$M = \frac{N \times d}{FOV} \tag{6.8}$$

$$f = \frac{M \times p}{M + 1} \tag{6.9}$$

where *FOV* is the FOV of the camera, *N* is the number of active pixels of the camera, *r* is the resolution of the measurement process, *d* is the pixel size of the camera, *M* is the lens magnification, *f* is the focal length of the lens, and *p* is the distance between the camera and the moving target.

For example, to measure displacements of a structure with maximum likely displacement of ±250 mm, a 500 mm long FOV is needed if the original edge tracking algorithm is used. For the best resolution with the camera used in this study (maximum 8192 active pixels), this FOV results in 61 μm resolution. However, using the new edge tracking algorithm, only a 50 mm long or shorter FOV is needed because using the new method, the length of the FOV depends only on the pattern dimensions to encompass at least five edges at each frame. Fairly low-resolution 1k pixels over this FOV result in a better resolution of 50 μm or less. With the 8192 pixels of the device used here over a 50 mm FOV, the resolution is 6.1 μm, which is 10 times better for no added cost or significant complexity.

By knowing the image size (*N*×*d*) and FOV, magnification, *M*, can be calculated from Equation (6.8), and Equation (6.9) can then be used to find a suitable lens with the required focal length based on a desired or allowed distance between the target and the camera. The resolution from Equation (6.7), can then be improved using sub-pixel interpolation techniques if required. For this paper, full camera resolution at frame rates up to 500 frames per second is used and other settings are chosen to have less than 30 μm resolution in measurements.

6.3. Camera-pattern calibration

If the CCD array of the camera is not perfectly parallel to the pattern plane (out-of-plane angled CCD) or the horizontal plane upon which the camera is mounted (in-plane angled CCD), the measurement results from Lim et al. method will have potentially significant error due to the distortion induced by the non-perpendicular perspective. An out-of-plane angled CCD array results in a non-unique distance between different parts of the pattern and the camera. Hence, closer parts of the pattern appear longer and further parts shorter in the captured frames compared to the non-angled case. This change alters the assumptions made in calculating the intersection points between the slanting and normal pattern lines and the scan line in Equations (6.3) and yields significant errors in the measurement results. The effect of in-plane angle should also be accounted for because the reported measurement results of Equations (6.5) and (6.6) are in the camera coordinate system and any inclination makes it different from the desired frame with horizontal and vertical axes. This section analyzes the effect of rotation about each of the three axes on the assumptions made by Lim et al. and consequently on the measurement results. A procedure for camera-pattern calibration is then proposed to eliminate the resulting errors due to camera-pattern misalignment.

Figure 6.7a shows the reference frames for the other panels in the figure. The three coordinate systems used are $\{G\}$, $\{C\}$, and $\{LS\}$, which are the ground, camera, and the scan line coordinate systems, respectively. In $\{C\}$, X_C axis is parallel to the CCD array, Y_C is perpendicular to X_C, and Z_C is normal to $X_C Y_C$ plane. Further, the dotted line on the pattern plane represents the original FOV of the camera when calibrated. In the ideal case, the two former coordinate systems are perfectly parallel, and the assumptions made in (Lim and Lim 2008) are satisfied.
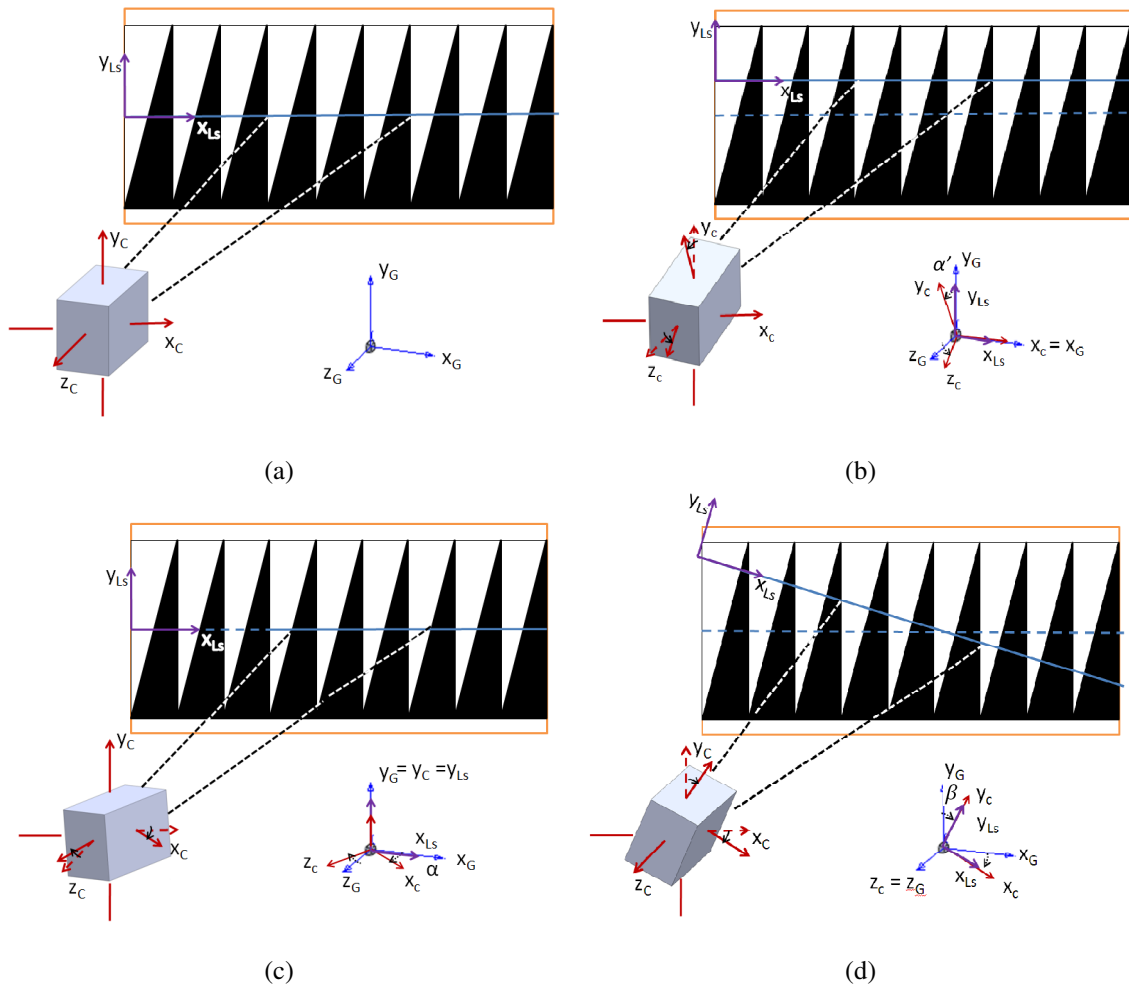
Figure 6.7. Different possible camera misalignments with respect to the global horizontal and vertical coordinates system

Figure 6.7b shows the case where the camera has a small rotation about X_C so that the camera scans a line a bit higher or lower than the original FOV depending on the rotation direction. Moreover, the FOV is wider due to the increase in the distance between the camera and the pattern. However, ratios of distances between the edges in the scanned frame and the orientation of $\{LS\}$ with respect to $\{G\}$ remain unchanged. Therefore, this type of misalignment does not alter the basic assumptions made in the original work.

In the second case, shown in Figure 6.7c, the camera rotates about Y_C axis. In this case, the camera scans a line that is a bit further to the right or to the left of the original FOV depending on the rotation direction. The out-of-plane angle between the

CCD plane (X_CY_C) and the pattern plane (X_GY_G), α, causes a non-perpendicular perspective of the pattern and alters the basic assumptions made by Lim et al. for the normal and slanting line equations in the pattern plane. This occurs because, unlike before, the closer parts of the pattern appear longer and further parts shorter, causing error in the measurement results even though {LS} is still parallel to {G}.

The last case is where the camera rotates about Z_C axis. As Figure 6.7d shows, this in-plane rotation of the camera does not alter any of the basic assumptions, and thus does not cause error on the measurement results. However, camera rotation rotates the coordinates system in which the results are reported (i.e. {LS}). Therefore, the results will no longer be in a desired coordinate system parallel to {G}. In reality, a combination of the two in-plane and out-of-plane angles is usually the case. Each angle should be carefully removed so that cancelling one does not cause the other.

6.3.1. Removing the out-of-plane angle

The out-of-plane angle of Figure 6.7c can be removed using a slightly different pattern designed for calibration. The proposed calibration pattern, shown in Figure 6.8, is an array of black and white rectangles with equal widths. The printed pattern is posted on a desired spot on the structure, and the line-scan camera is pointed at the pattern for calibration. As Figure 6.8 shows, the scan line intersects the parallel pattern lines, and only when there is no out-of-plane angle, the following definition holds:

$$\frac{AB}{A'B'} = \frac{BC}{B'C'} = \frac{CD}{C'D'} = ... = 1 \qquad (6.10)$$

where $A'B', B'C', C'D',...$ are the measured edge to edge Euclidean distances in the linear frame captured by the camera.

In the case where an out-of-plane angle exists, the edge to edge distances in the linear frame, as seen by the camera, would not be the same due to the non-perpendicular

perspective from the pattern. Thus, Equation (6.10) does not hold. Moreover, as the figure clearly shows, the likely existing in-plane-angle, β, does not alter the condition of Equation (6.10). Therefore, the calibration pattern proposed cancels the in-plane angle effect when the camera is calibrated for the out-of-plane angle. Further, Figure 6.8 also shows that there is no need for careful placement of the pattern with respect to the global horizontal and vertical axes, and the angle γ does not affect the calibration process.
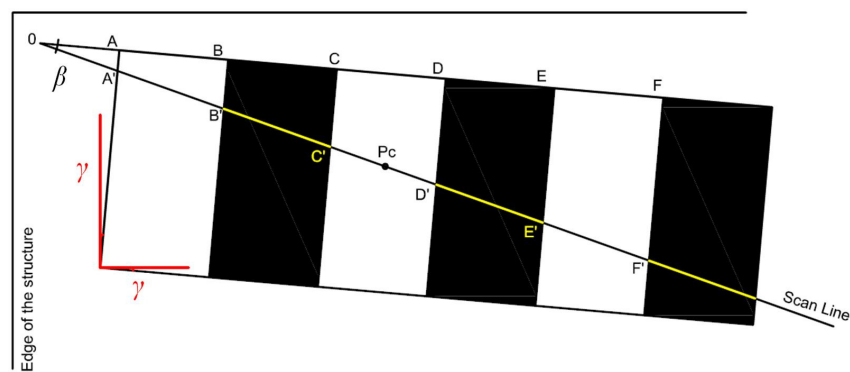
Figure 6.8. The newly designed calibration pattern and the scan line at zero out-of-plane angle situation

To remove the out-of-plane angle of Figure 6.7c using the designed calibration pattern, the edge to edge distances in the first captured frame are measured and compared. If they are not equal, the camera is rotated in the plane upon which the camera is mounted (about Y_C axis in Figure 6.7c) until Equation (6.10) is satisfied to within a desired tolerance. Direction of the rotations is always toward the side with longer distances, since same side of the camera is closer to the pattern plane.

6.3.2. Removing the in-plane angle

The in-plane angle rotates the scan line frame. Therefore, the measurement results would not represent horizontal and vertical displacements of the pattern with respect to the desired global coordinate system. The in-plane angle, or the initial scan line angle with respect to the global frame (β in Figure 6.7d), can be calculated from

Equation (6.6). In this equation, a_0, the initial slope of the scan line in $\{T\}$ can be calculated using the method of Lim et al. with the measured edge to edge distances in the first captured frame. Knowing that $\{T\}$ is rotated by 45° with respect to $\{M\}$ yields the following equation for the in-plane angle provided that $\{M\}$, the pattern frame shown in Figure 6.1, has been precisely posted on the target so that it is parallel to the global frame $\{G\}$:

$$\beta = \tan^{-1} a_0 + \frac{\pi}{4} \tag{6.11}$$

6.4.   Experimental validation

6.4.1. Set-up

To assess the performance of the overall system (extended method and calibration of Sections 6.3.1 and 6.3.2) in capturing seismic structural displacements, a SDOF case-study structure with an undamped natural period of 0.5 seconds was considered. Displacements of the structure under the 20 different earthquakes in Table 2-1 were simulated in MATLAB® with 5% constant damping. Peak displacement results for each record are shown in Table 6-2.

The 0.5 second natural period was chosen to ensure the presence of higher frequencies in the displacement data to examine how well the line-scan measurement system captures these relatively faster motions. Fast Fourier Transform (FFT) analysis of the derived displacement suites for simulated structures with higher and lower natural periods, as shown in Figure 6.9, confirms that there is no significant frequency content in the displacement data greater than 15 Hz. Therefore, sampling at 500 Hz is far beyond the frequencies involved in the structure's motion and guarantees that all necessary motions and dynamics are captured.

Table 6-2. Peak displacements of the case-study structure, used for experimental validation of the line-scan displacement measurement method, under the ground motion records in Table 2-1

EQ	Peak Displacement (cm)	EQ	Peak Displacement (cm)
EQ1	1.71	EQ11	3.77
EQ2	3.78	EQ12	4.53
EQ3	1.5	EQ13	3.09
EQ4	3.39	EQ14	4.14
EQ5	4.85	EQ15	2.61
EQ6	3.90	EQ16	2.03
EQ7	5.26	EQ17	2.76
EQ8	4.23	EQ18	0.94
EQ9	2.86	EQ19	3.83
EQ10	3.8	EQ20	3.52
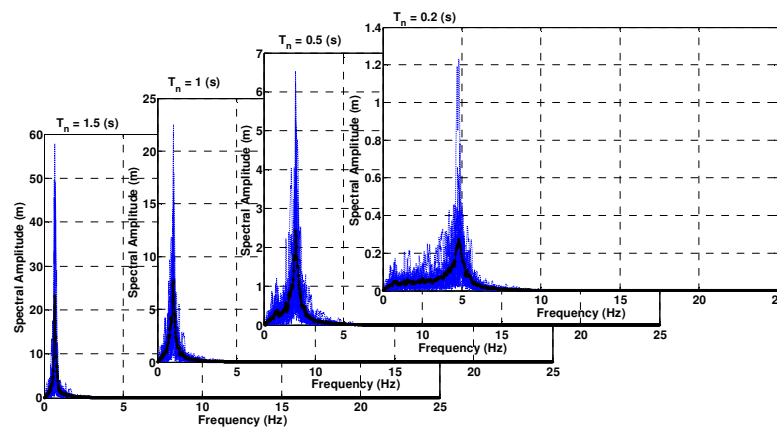
Figure 6.9. FFT analysis of displacement suites derived from records in Table 2-1 for case-study structures with different natural periods

A computer-controlled cart, controlled by a dSPACE® system (dSPACE GmbH, Germany), was used to generate the simulated displacement records. Encoder measurements of the actual position of the cart were used to validate the results from the imaging system. The cart movements represent motions of the centre of mass of a real linear structure with the same natural period simulated. Figure 6.10a shows the experimental set-up in detail.

In addition, to show the capability of the proposed method to capture even higher frequencies and smaller motions, a dynamic material testing machine (MTS 810,

MTS Systems Corporation), shown in Figure 6.10b, was used to generate high-frequency, low-amplitude sinusoidal motions as small as ±1 mm at 5 Hz, which is a value well below most SHM algorithms requirements.

(a)

(b)
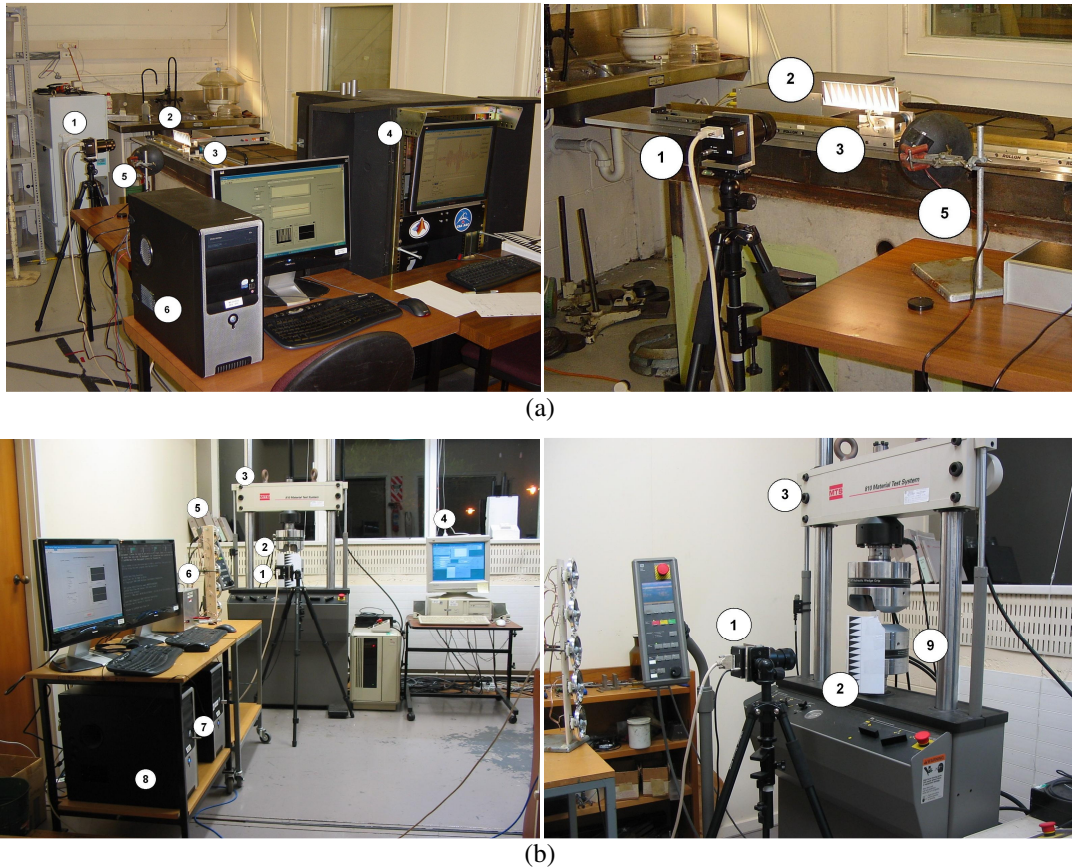
Figure 6.10. Experimental set-up used for a) random (1. Line-scan camera, 2. Pattern, 3. Cart, 4. dSPACE, 5. Light, and 6. Data acquisition computer) and b) harmonic (1. Line-scan camera, 2. Pattern, 3. MTS machine, 4. Computer to control the MTS machine, 5. Light, 6. Camera and light source power supplies, 7. Target computer, 8. Host computer, and 9. Moving head of the MTS machine) displacement measurement tests

In both the random and sinusoidal tests, a 20×60 mm (*H*×*W*) pattern printed with 600 dpi (dots per inch) resolution was posted on the moving target so that the pattern sides (*H* and *W* in Figure 6.1) were parallel to the global horizontal and vertical axes. The line-scan camera was calibrated using the method described in Section 6.3. The pattern is visible in Figure 6.10.

6.4.2. Results and discussion

Figure 6.11a shows variations of the difference between norms of the measured and actual displacement signals over the norm of the actual signal for the 20 different displacement records derived from the earthquake ground accelerations described in Table 2-1 for the case study structure. This ratio is less than 3% for the entire suite, and the measured and actual signals are almost identical. Figure 6.11b shows the results for record 20 in Table 2-1 as an example.

<center>(a)   (b)</center>
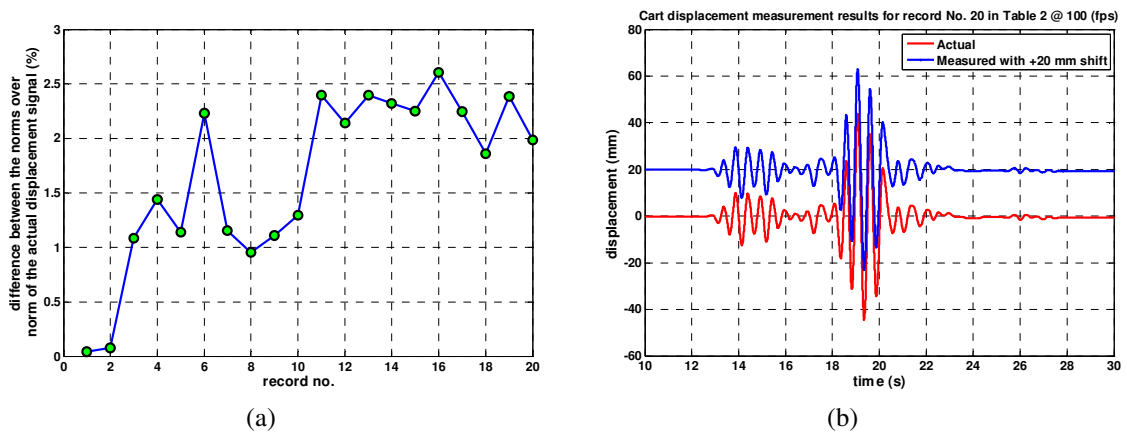
Figure 6.11. a) Absolute value of the difference between norms of the actual and measured displacement signals over the norm of the actual displacement signal in percent for the records in Table 2-1 and b) measurement results for record 20 in Table 2-1, as an example, with a 20 mm shift to show both results clearly as separate lines

Since sampling rate and resolution of the displacement measurement set-up is sufficient to capture movements of the cart, the error is mainly due to inaccurate cart position data from the encoder. These encoder errors are caused by the backlash in a pinion coupled to the encoder. This pinion is moved on a rack by the cart movements. Therefore, the output from the encoder does not change when the cart movements are smaller than the backlash, which is approximately 0.5 mm. Hence, the image-based displacement results are within the encoder error.

Results for the harmonic test are shown in Figure 6.12. Once more, error between the actual and measured displacements at peak points is less than 3%, and the actual and measured displacement signals are almost identical. Moreover, the norm of

the error for the entire 25-second measurement period over the norm of the actual displacement signal from interior LVDT of the MTS machine is 4.64%. These values demonstrate the capability of the proposed method for high-frequency low-amplitude vibration measurement, which is typically the most difficult to measure without a direct contact sensor.
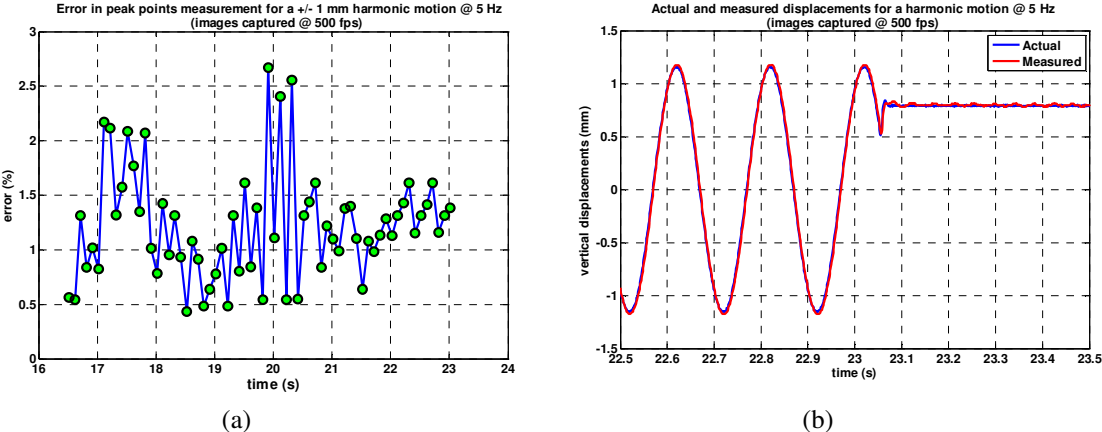
Figure 6.12. a) Error in peak points measurement and b) actual and measured displacements for the lower head of the MTS machine, travelling ±1 mm harmonically at 5 Hz

As will be shown in the next chapter, Monte Carlo simulation of 100k randomly selected possible measurement cases uniformly distributed over possible ranges for each of the parameters involved in the measurements, shows that the 600 dpi resolution used to print out the 20×60 mm pattern (0.2% error in H and 0.07% error in W) has almost no effect on the results reported here. Moreover, the pattern surface is assumed to have no bumps when printed and posted on a desired spot on the structure, and error due to these likely surface bumps are neglected in the measurements. Such a surface smoothness, if required, can be easily achieved by printing the pattern on a hard surface, such as a wood or plastic board.

142

6.5. Summary

The chapter empirically examined high-speed line-scan cameras as a robust and high-speed displacement sensor for a range of seismic monitoring applications. Line-scan cameras have the additional benefit of requiring no invasive mechanisms or added processing to provide a high-resolution output measure, and do not interfere architecturally. Following the method proposed by Lim et al. for measuring foundation pile movements, multiple displacements and motions of any structure can be determined in real time at rates over 1 kHz using only one high-speed line-scan camera and a special pattern. This resolution is more than sufficient for structural monitoring and control problems.

A novel edge tracking algorithm was also developed that enables high-resolution measurement of large motions using relatively low-resolution line-scan cameras, as well as equivalent resolution for very small motions, a unique advance that enables seismic displacement monitoring. Further, as the accuracy of the measurement results depends directly on camera-pattern calibration and satisfying the assumptions made by Lim et al., an easy-to-implement calibration procedure was developed that ensures the accuracy of the measurement results. Finally, the versatility of the total measurement procedure was examined through both harmonic and random vibration experiments with a suite of different input motions applied to a computer-controlled cart. The impact of error in the printed pattern dimensions on the measurement results is assessed in the next chapter using Monte Carlo methods to rigorously determine the level of confidence of the reported measurement results.

Comparing the input and the measured motions confirms that vision-based structural displacement measurement utilizing a high-speed line-scan camera offers a robust, high-resolution and low-cost means of non-invasively measuring structural

vibration displacements. The line-scan displacement measurement method developed, as any other vision-based approach to structural displacement measurement, can only measure relative displacements to the camera and is mainly meant for use in laboratory environments, where the camera can be put on a fixed base. However, it is equally valued where measuring relative displacements, such as inter-storey drifts, is important, which is the situation in many practical and realistic SHM applications.

CHAPTER 7

Monte Carlo simulation of inaccurate pattern dimensions effect on the method of Lim et al.

7.1.   Introduction

Vision-based structural displacement measurement methods (Fu and Moosa 2002; Kanda et al. 2004; Hutchinson et al. 2005; Chang and Ji 2007; Lee et al. 2007; Ji and Chang 2008; Orteu 2009) can be very high-resolution and high-rate, depending on sampling rate and resolution of the acquired images. However, the increasing volume of image data to be processed, as resolution and sampling demands increase, significantly increases the processing time, computational complexity, and the processing hardware

cost. Line-scan based approaches to structural displacement measurement, originally proposed by Lim et al. (2008), significantly decrease the size and pixel volume of the acquired frames and enables high-speed displacement measurement, as seen in the previous chapter.

The method of Lim et al. was empirically evaluated and significantly modified for seismic structural displacement measurement in the previous chapter. In particular, two extensions were made to the original method. First, a new edge tracking algorithm for the image processing part of the original method is developed that enables high-resolution measurement of large seismic displacements using low-cost low-resolution line-scan cameras. Second, it also enables best or maximum resolution for all scales of motion, significantly broadening the potential application space. Third, an easy-to-implement camera-pattern calibration procedure is proposed that guarantees the basic geometrical assumptions required are fulfilled, ensuring the accuracy of the output measurements.

However, measurement accuracy also depends directly on the correctness of the printed pattern dimensions. This chapter evaluates the impact of inaccurate pattern dimensions on measurement results. It uses Monte Carlo Simulation (MCS) of 100k randomly chosen different possible measurement cases to determine the level of confidence in the measured displacements as a function of error in the pattern dimensions. It thus quantifies the potential sources of error in terms of quantifiable errors in the pattern used. Hence, overall, this chapter together with the previous one present and characterize a practical, high-speed, high-accuracy, but low-cost means of non-invasive, non-contact displacement sensing.

7.2.   Sources of error on measurement results

As Equations (6.1)-(6.3) show, any inaccuracy in the pattern dimensions, H (height) and W (width), will lead to an error in the measured movements in Equations (6.5) and (6.6). Moreover, when the CCD array of the camera is not perfectly parallel to the pattern plane (out-of-plane-angled CCD) or the horizontal plane upon which the camera is mounted (in-plane-angled CCD), the results will have further error. As discussed in the previous chapter, the error due to an out-of-plane-angled camera induces distortion, and in-plane angled camera error is produced by the inclination that makes the line-scan frame different from the desired frame with horizontal and vertical axes. The present chapter assumes the camera is calibrated prior to the measurement so that these effects are eliminated, as described in the previous chapter. Thus, all resulting errors are due solely to inaccurate pattern dimensions.

7.3.   Effect of inaccurate pattern dimensions

7.3.1. Error evaluation method

By substituting Equations (6.1) and (6.2) in Equation (6.3), changes in measured coordinates of the centre point at time t can be written using partial derivatives of $(Pc_t)_x$ and $(Pc_t)_y$, components of Pc_t in x and y directions, with respect to H and W:

$$\begin{pmatrix} \Delta(Pc_t)_x \\ \Delta(Pc_t)_y \end{pmatrix} = \begin{pmatrix} \dfrac{\partial(Pc_t)_x}{\partial H}\Delta H + \dfrac{\partial(Pc_t)_x}{\partial W}\Delta W \\ \dfrac{\partial(Pc_t)_y}{\partial H}\Delta H + \dfrac{\partial(Pc_t)_y}{\partial W}\Delta W \end{pmatrix} \tag{7.1}$$

or,

$$\begin{pmatrix} \Delta(Pc_t)_x \\ \Delta(Pc_t)_y \end{pmatrix} = \begin{pmatrix} \dfrac{\sqrt{2}R_t}{2}\Delta H - \dfrac{C+\sqrt{2}AR_t}{2B}\Delta W \\ \dfrac{\sqrt{2}R_t}{2}\Delta H + \dfrac{C+\sqrt{2}AR_t}{2B}\Delta W \end{pmatrix} \tag{7.2}$$

Similarly, using Equation (6.6), the error in rotation angle measurement can be written:

148

$$\Delta\Theta_t = \frac{AB}{A^2 W^2 + B^2 H^2}\left(H\Delta W - W\Delta H\right) \tag{7.3}$$

where A, B, and C are dimensionless parameters defined:

$$A = L_n - L_m \tag{7.4}$$

$$B = L_m - L_n + (L_m + 1)(L_n + 1) \tag{7.5}$$

$$C = -\sqrt{2}\left(L_n + 1\right) \tag{7.6}$$

and all other parameters have been previously defined.

Using Equations (7.2) and (7.3), it is possible to assess the error on measurements made with Lim et al. method due to inaccuracies in pattern dimensions defined by ΔH and ΔW.

7.3.2. Monte Carlo simulation

Monte Carlo Simulation (MCS) can provide approximate solutions for a wide class of non-deterministic problems through statistical sampling on a computer. First, ranges of different parameters affecting the solution are determined. Second, considering the probability distribution of each of the parameters, n different random values within the specified ranges are assigned to each parameter. Simulating the problem for all n random cases provides an approximate solution for the problem. The simulation error decreases by $\frac{1}{\sqrt{n}}$ as the population of the random simulated cases increases (Fishman 1996).

In this case, five different variables are involved in determining the measurement results: 1,2) the pattern dimensions, H and W, and 3,4,5) the frame-dependent parameters measured at each frame, L_n, L_m, and R_t. The pattern dimensions, H and W, can be any real positive number. To keep the pattern within the FOV of the camera as the pattern moves, W should be sufficiently wide. Accordingly, H needs to be

long enough to avoid very thin and hard to detect parts occurring at the corners of triangles in the pattern. Therefore, 10≤W≤200 mm and $0.2 \leq \dfrac{H}{W} \leq 5$ is recommended for the structural displacement measurement case as these values encompass a typical range for this application space.

The frame-dependent parameters, L_n and L_m, change each measurement time step. Depending on the position of the pattern, different values may be obtained from processing the acquired frames. For example, Figure 7.1 shows three possible cases for the scan line position on the pattern. From Case (1) to (3), in the highlighted box on the left, the ratio between black to white distances decreases, and finally approaches zero, as the black part becomes shorter. In addition, rotation in the opposite direction shows that the ratio approaches infinity as the white part shortens. Similar behaviours can occur for the other pattern triangle elements. However, in reality, the width of the pattern is chosen according to the likely maximum rotational and translational movements of the target to keep the FOV of the camera limited to the middle of the pattern. Therefore $0 \leq L_{n(or\ m)} \leq 20$ is suggested.
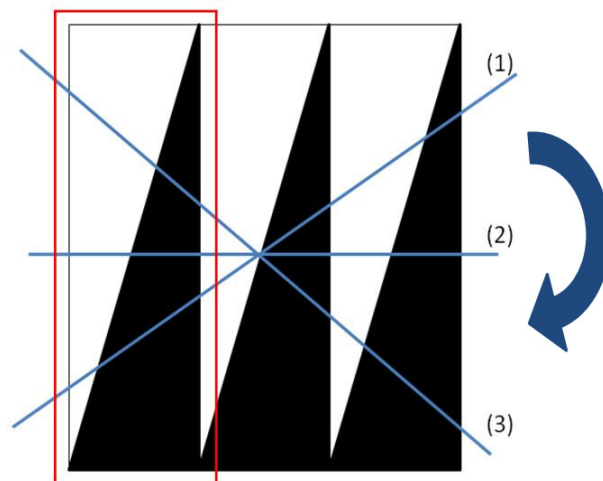
Figure 7.1. Changes in L_n and L_m with pattern rotation relative to the scan line

As Figure 6.2 shows, P_C can be either between P_{0H} and P_{1H}, or outside of this space, depending on the pattern movement resulting from movement of the target.

Therefore, in Equation (6.4), as the pattern moves in one direction, R_t becomes smaller or larger depending on the direction of the movement. Thus, upper and lower bounds for R_t can be any number. However, pattern dimensions can be chosen based on the maximum likely movement of the pattern so that P_C always falls between any set of P_{nH} and $P_{(n+1)H}$. In this case, R_t is between 0 and 1.

To evaluate the independence of the frame-dependent parameters, two illustrative examples are given. The first example is illustrated in Figure 7.2. In this figure, O is the centre of the CCD array and from labels (1) to (3) as the pattern (or the scan line) rotates about O, R_t remains constant:

$$R_t = \frac{\overline{OA}}{\overline{AF}} = \frac{\overline{OB}}{\overline{BE}} = \frac{\overline{OC}}{\overline{CD}}$$
(7.7)

However, it can be shown that $L_{n(or\ m)}$ changes during this rotation:

$$L_{n(or\ m)} : \frac{\overline{AA'}}{\overline{A'F}} \neq \frac{\overline{BB'}}{\overline{B'E}} \neq \frac{\overline{CC'}}{\overline{C'D}}$$
(7.8)
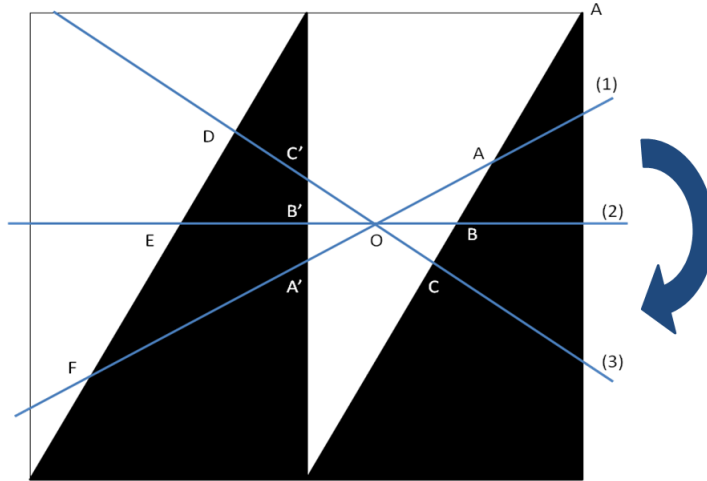
Figure 7.2. From (1) to (3) L_m and L_n change while R_t is constant

The second example occurs when the pattern moves only in the horizontal direction and is perfectly aligned with the scan line. In this case, as shown in Figure 7.3, as the pattern moves, $L_{n(or\ m)}$ is fixed while R_t changes. These two examples clearly show that changes in R_t are independent from changes in L_m or L_n, and R_t is an independent variable that cannot be ignored in the simulation.
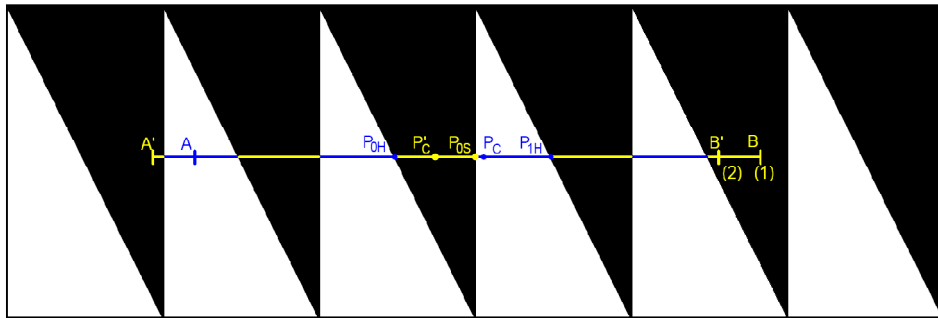
Figure 7.3. From (1) to (2) L_m and L_n are fixed while R_t changes

To simulate the errors in the displacement measurement results due to inaccurate pattern dimensions, 100k uniformly distributed random values are selected over the specified ranges for each of the five parameters: H, W, L_m, L_n, and R_t. Errors in the pattern dimensions are assumed to be within ±1% of the actual values selected for H and W over a step-wise range with 0.2% increments. This range is based on an assessment of standard printer errors (resolution>300 dpi and pattern dimensions>10 mm). Thus, 11×11 different combinations are assessed for the errors in H and W.

7.4. Results and discussion

Figures 7.4 to 7.6 show variations of the median error in the horizontal, vertical, and rotational movement measurement with the error in the pattern dimensions. Figures 7.7-7.9 show the 5th-95th inter-percentile range for each of the median errors in Figures 7.4- 7.6. These inter-percentile values for each case of ΔH and ΔW show a range where 90% of the simulation results can be found for that particular case. The median values are in the middle of these ranges. Therefore, the inter-percentile value can be used as an indication of how the simulation results are spread around the median value, or in other words how well the median value represents the simulation results set for that particular case.

152
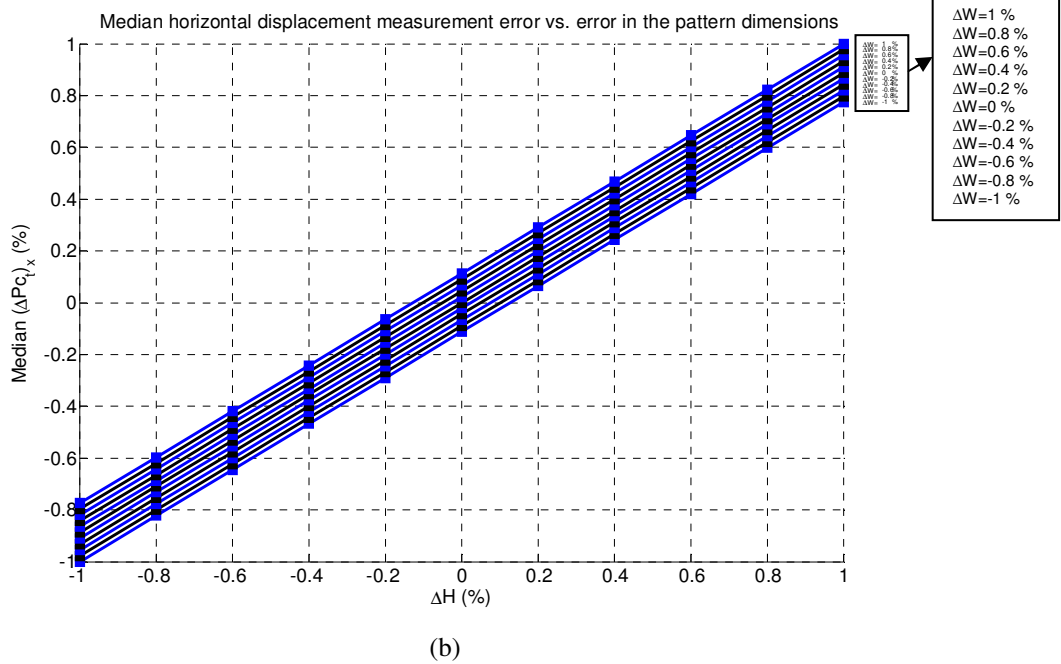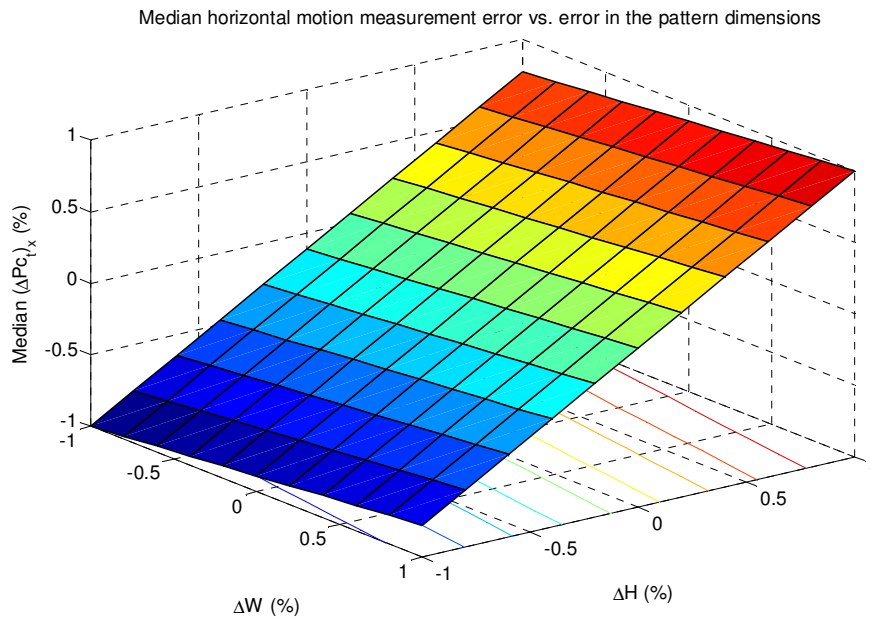
Figure 7.4. Median horizontal displacement measurement error in percent due to imprecise pattern dimensions: a) median horizontal displacement measurement error surface and b) median errors for fixed values of ΔW

Median vertical motion measurement error vs. error in the pattern dimensions

(a)

Median vertical displacement measurement error vs. error in the pattern dimensions

ΔW=-1 %
ΔW=-0.8 %
ΔW=-0.6 %
ΔW=-0.4 %
ΔW=-0.2 %
ΔW=0 %
ΔW=0.2 %
ΔW=0.4 %
ΔW=0.6 %
ΔW=0.8 %
ΔW=1 %

(b)
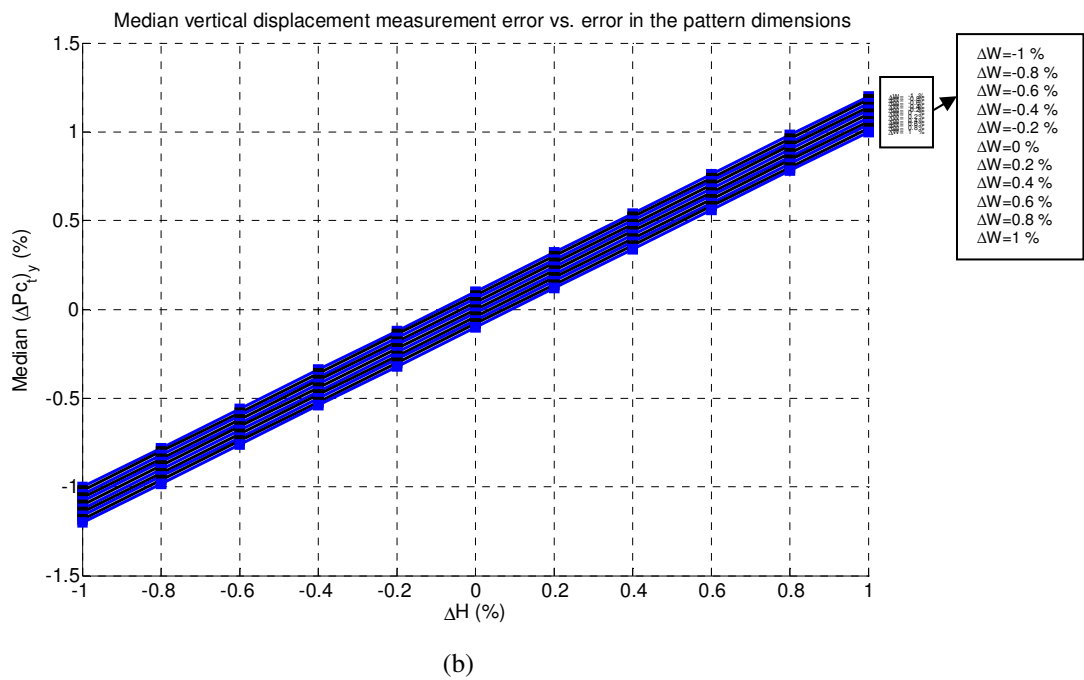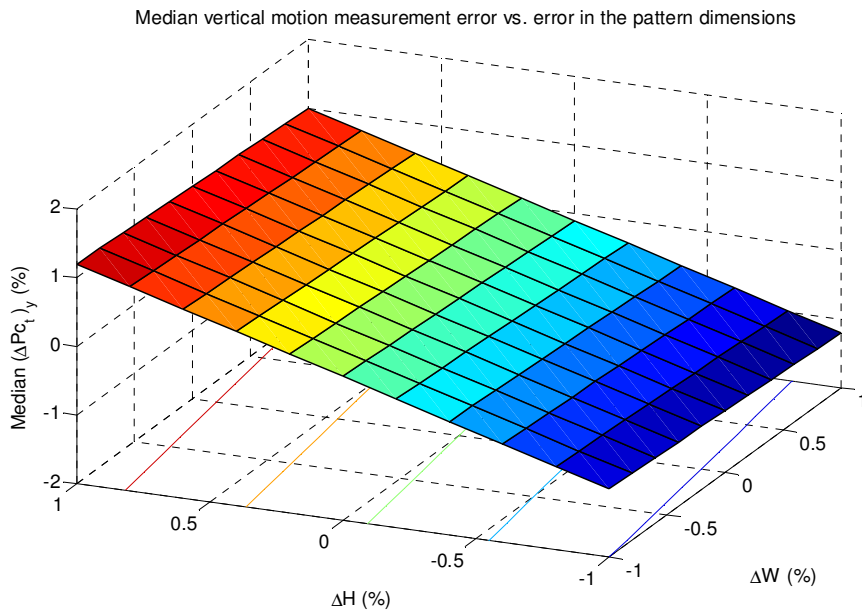
Figure 7.5. Median vertical displacement measurement error in percent due to imprecise pattern dimensions: a) median vertical displacement measurement error surface and b) median errors for fixed values of Δ*W*

154
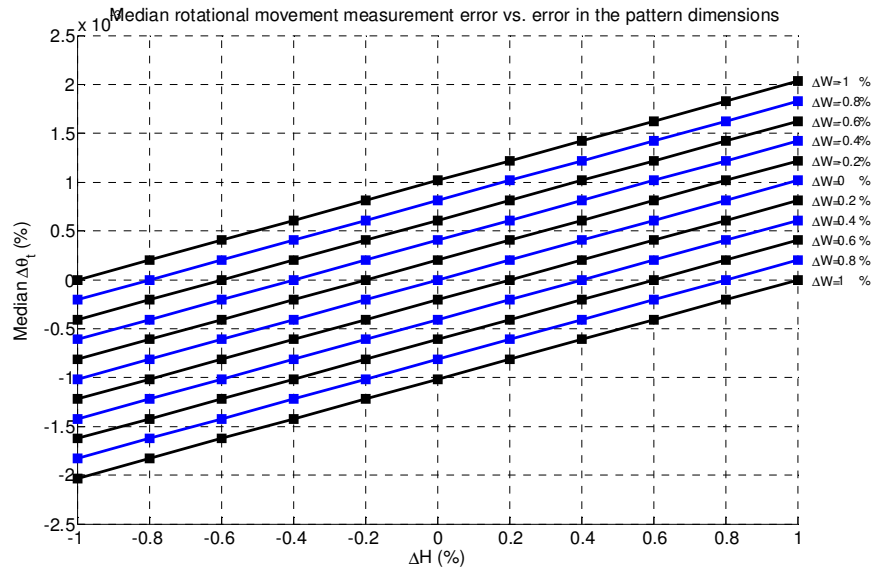
Figure 7.6. Median rotational movement measurement error in percent due to imprecise pattern dimensions

As the simulation results confirm, measurement results for the horizontal and vertical displacements are considerably more sensitive to errors in the pattern dimensions than the rotation measurement results. Errors as large as ±1% in the pattern dimensions, due to imprecise printing process, result in median errors around ±1.0% with inter-percentile ranges of up to 1.3% in measurement results for the horizontal direction. In the vertical direction, the results are ±1.2% with 5th-95th inter-percentile ranges of up to 7.4%. The same amount of inaccuracy in pattern dimensions does not alter the rotational movement measurements, with median error near 0% and an inter-percentile range of 1.1% in the worst case.

Figures 7.4a and 7.5a show that the median error in measurement results for the vertical and horizontal measurements is more sensitive to error in *H* than in *W*. In these figures, both of the median error surfaces are sloped planes in Δ*H* direction with considerably less variation in Δ*W* direction. This result can also be seen in Figures 7.4b and 7.5b, where median errors for fixed Δ*H* values are close to each other across the range of Δ*W*.

155
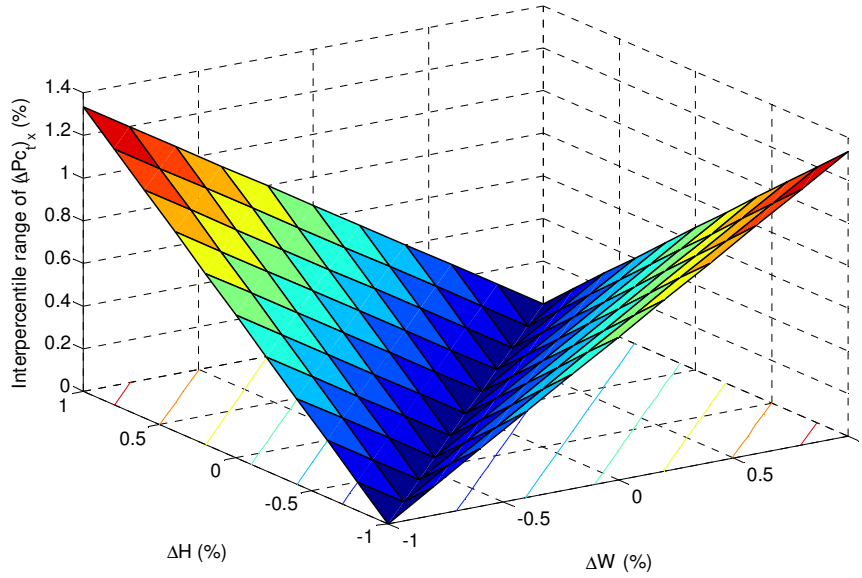
(a)
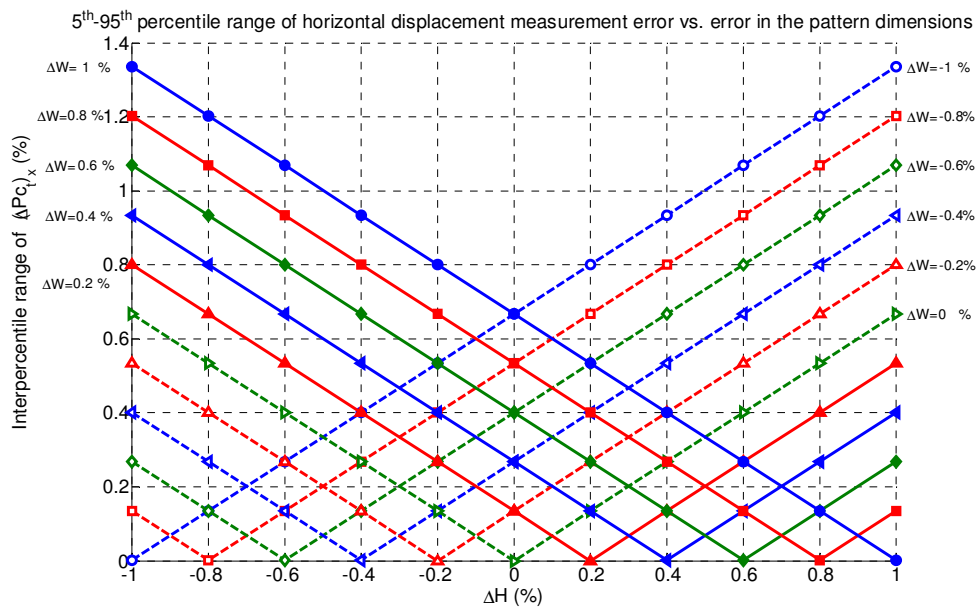
(b)

Figure 7.7. 5th-95th inter-percentile range of the horizontal displacement measurement error in percent due to inaccurate pattern dimensions: a) inter-percentile surface and b) inter-percentile ranges for fixed values of ΔW (solid lines are for $\Delta W > 0$).

5th-95th percentile range of vertical motion measurement error vs. error in the pattern dimensions

(a)

5th-95th percentile range of vertical displacement measurement error vs. error in the pattern dimensions
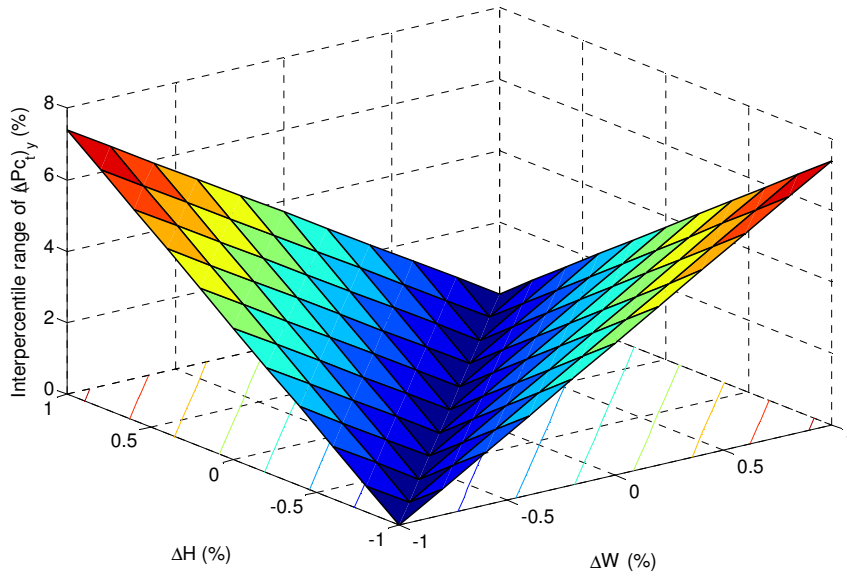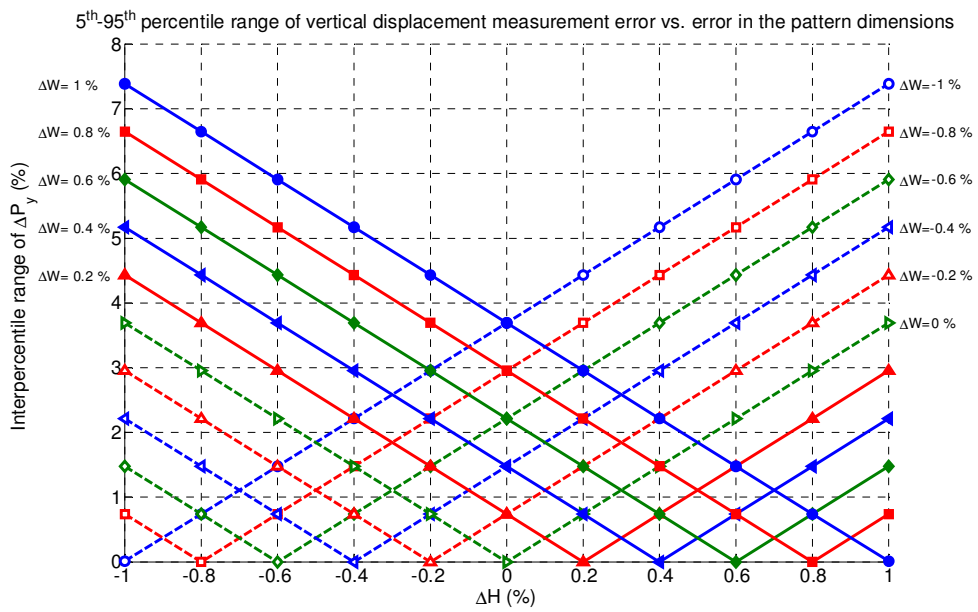
(b)

Figure 7.8. 5th-95th inter-percentile range of the vertical displacement measurement error in percent due to inaccurate pattern dimensions: a) inter-percentile surface and b) inter-percentile ranges for fixed values of ΔW (solid lines are for $\Delta W > 0$)

5th-95th percentile range of rotational motion measurement error vs. error in the pattern dimensions

(a)
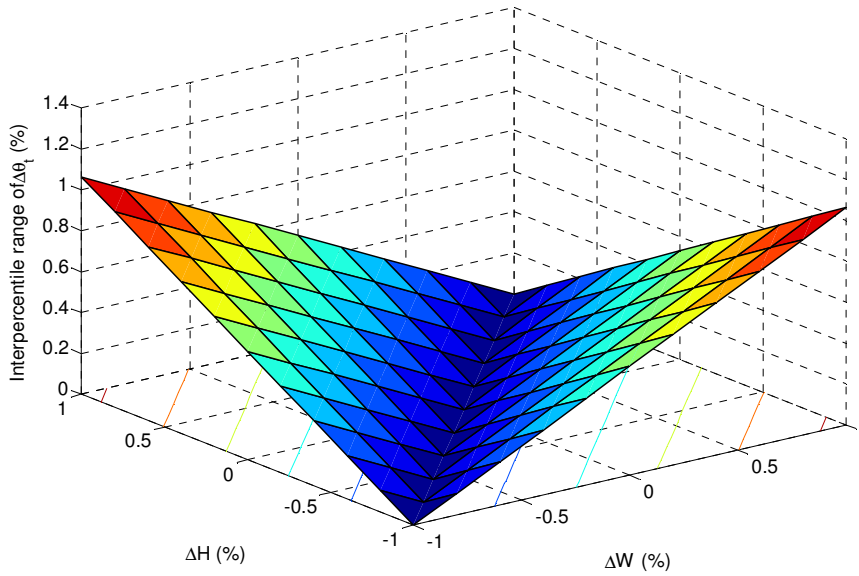
5th-95th percentile range of rotational movement measurement error vs. error in the pattern dimensions
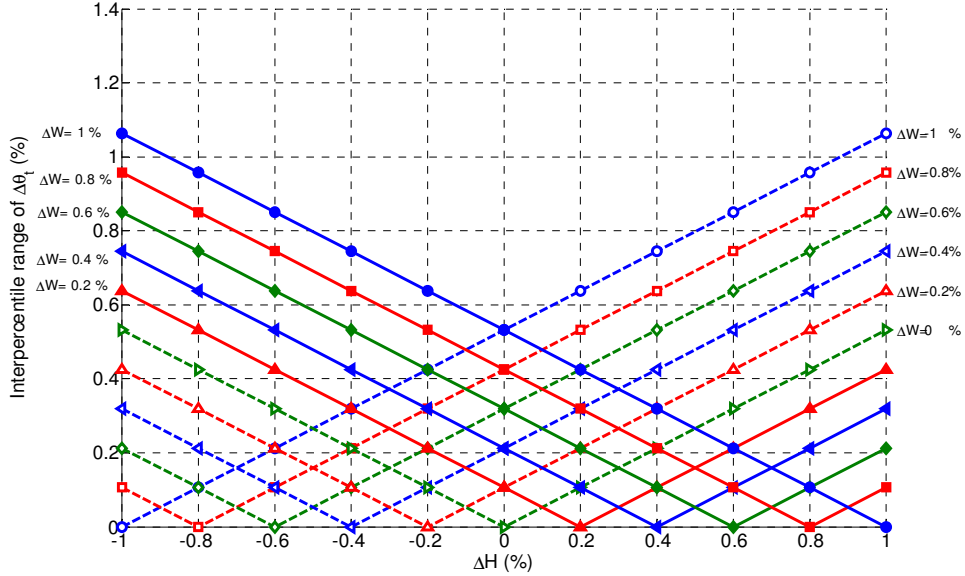
(b)

Figure 7.9. 5th-95th inter-percentile range of the rotational movement measurement error in percent due to inaccurate pattern dimensions: a) inter-percentile surface and b) inter-percentile ranges for fixed values of ΔW (solid lines are for $\Delta W > 0$).

As an example of how these results can be used to assess the accuracy of measurement results, a 20×60 mm (*H*×*W)* pattern printed using an ordinary 600 dpi printer is considered. The printing resolution, in this case, is approximately 0.042 mm per pixel. Thus, errors in the horizontal (*H*) and vertical (*W*) dimensions of the pattern are approximately ±0.2% and ±0.07%, respectively. As Figures 7.4-7.6 show, this error in the pattern dimensions results in ~±0.19% and ~±0.23% maximum median errors in the measurement results in the horizontal and vertical directions with 5th-95th inter-percentile ranges of up to ~0.2% and ~1%, respectively.

Overall, as the results confirm, for seismic structural displacement measurement applications, typical patterns (*H*>10 mm, *W*>10 mm) printed using standard printers with a resolution higher than 300 dpi induce very small amounts of error (<~±1%) in the measurement results. Therefore, errors due to imprecise printing process can be ignored in many seismic displacement measurement applications. However, when very high-resolution measurement is required, the errors caused by imprecise printing process may be high and should be evaluated using the results developed in this chapter.

7.5.   Summary

High-speed computer vision based methods for real-time structural displacement measurement are typically computationally-intensive and/or require costly processing hardware. They are thus not suitable for real-time applications. Using line-scan cameras significantly decreases the volume of acquired pixels and frames, and makes high-speed displacement measurement far more feasible using relatively low-cost cameras, hardware, and processing. Recently, Lim et al. proposed a method that uses only one line-scan camera with a specific printed pattern to capture structural displacement in multiple directions, as well as rotation. The method was extended and modified for

measuring seismic structural displacements in Chapter 6. However, the effect of inaccuracy in the pattern dimensions, resulting from imprecise printing, on the accuracy of measurement results was unknown. In particular, where precise motion measurement is required, this inaccuracy may significantly affect measurement quality, as the entire method is based around this pattern.

This chapter evaluated this effect through Monte Carlo simulation of 100k randomly selected possible measurement cases for a range of pattern dimensions varying between 10 and 200 mm in width with aspect ratios ranging from 0.2 to 5. Results for the simulated cases show that errors as large as ±1% in the pattern dimensions result in median errors around ±1.2% with 5th-95th inter-percentile ranges of up to 7.4% in horizontal and vertical measurements. Moreover, the same amount of inaccuracy in the pattern dimensions does not alter rotational movement measurements. Overall, as the results confirm, for seismic structural displacement measurement applications, typical pattern dimensions (>10 mm) and printing resolutions (>300 dpi) induce negligible amounts of error (<~±1%) in the measurement results. Thus, for the application focus of this thesis, error due to imprecise printing process can be ignored.

We build too many walls and not enough bridges.

Isaac Newton
English Mathematician, 1642-1727

CHAPTER 8

Conclusions

This thesis explored novel computationally-efficient algorithms and cost-effective sensors for RT-SHM of a broad range of realistic nonlinear hysteretic structures undergoing seismic excitation. The parametric SHM methods developed can directly identify changes in the key structural parameters including stiffness, damping, and the nonlinear baseline model parameters, in real time. These structural parameters are directly related to well-recognised damage metrics and provide useful information about the safety and serviceability of structures during and immediately after an event. Further, the algorithms developed provide the data required for many structural control methods for damage avoidance or mitigation purposes.

The SHM methods developed in this thesis directly identify changes (damage)

in stiffness, damping, and, importantly, the nonlinear baseline model parameters. Therefore, unlike modal or frequency metric based approaches, these methods are capable of locating damage and are highly sensitive to small yet important amounts of damage. Equally importantly, the methods developed provide SHM information in real time at a very low computational cost and complexity compared to their other competitive real-time approaches. This great advantage over many existing RT-SHM approaches makes the techniques developed more amenable to real-world applications.

The RT-SHM algorithms developed use a nonlinear Bouc-Wen hysteretic baseline model to capture more dynamics of the structure. These parametric methods are thus capable of uniquely identifying likely damage to the structure by identifying changes to the overall structural model parameters. In this sense, these methods are also superior to existing non-parametric RT-SHM methods, such as ANN-based approaches, that can capture the full dynamics of the structure and provide real-time health information, but are not capable of localizing or quantifying the damage that occurred. The nonlinear Bouc-Wen baseline model was chosen for simplicity, as well as its flexibility to model a wide range of nonlinear structural behaviour. More comprehensive models that offer more structural parameters to be monitored and consequently more information can be developed and implemented with similar approaches, as the methods presented are readily generalised.

In developing the specific RT-SHM methods presented in this thesis, careful attention was given to cases where only very limited *a priori* knowledge of the structure is available prior to the monitoring and identification process, such as in historical structures, and appropriate methods were developed accordingly. Cases where typically more design data is available before the SHM process were also considered and simpler methods were developed to better accommodate those cases. Further, the last algorithm

developed, in particular, does not rely on the availability of difficult to measure structural displacements and provides RT-SHM data using only measured accelerations and velocities, which is a significant simplification.

To enable these methods, a robust and high-rate displacement sensor is required. Hence, a line-scan based displacement measurement method, originally proposed by Lim et al. (2008) for foundation pile movement measurement, was empirically evaluated and significantly extended for seismic structural displacement measurement. The modified method offers a novel, low-cost and high-resolution means of measuring seismic structural displacements in multiple directions, as well as rotations, without extensive sensor networking, architectural interference, or necessary invasive implementation prerequisites.

Overall, the results presented showed significant promise and highlighted several key recommendations to optimise the SHM methods developed. These methods remain to be experimentally proven and further tested, particularly against noise and other operational problems prior to implementation by the profession. However, the overall methods and approach are readily generalisable and create a platform for further realistic development of SHM.

The following sections highlight the specific contributions from this research to the SHM field:

Chapter 2 developed a computationally-efficient LMS-based algorithm and a two-step structural identification method for RT-SHM of nonlinear hysteretic structures. The RT-SHM algorithm developed, utilising a baseline nonlinear Bouc-Wen structural model, can directly identify changes in stiffness and plastic deflections in real time. Proof-of-concept simulation results showed that for the simulated SDOF structure and suite of records considered, the algorithm identifies stiffness changes to within 10% of

true values in less than 2.0 seconds, in a realistic scenario with fixed filter tuning parameters. Further, median ratio of the norm of error signal in identifying plastic deformations to the norm of actual as-modelled plastic deflection signal was shown to be 7.1% for the suite of records used. Finally, permanent deformation was identified to within 7.46% of the actual value using noise-free simulation-derived structural responses for the 20 different ground motion records considered. The algorithm developed is thus robust to ground motion excitation.

The chapter thus showed that:

- Computationally simple adaptive filtering technique can be readily extended by utilising a nonlinear baseline model to accurately identify stiffness, as well as plastic and permanent deflections in real time. These identified values can provide the data required for structural control methods. Equally, they provide important post-event information on the future serviceability, safety, and repair cost, in particular, the two latter identified values.

- The two-step identification method presented thus offers significant potential benefit in assessing structural damage in a broad range of nonlinear Bouc-Wen hysteretic structures.

The results presented in Chapter 2 could be readily improved with a more optimized adaptive filter with a variable step size or tuning parameter, using higher sampling rates, and greater number of taps or prior time step values used in the identification.

Chapter 3 developed a real-time fault detection and diagnosis method for SHM of nonlinear Bouc-Wen hysteretic base-isolation systems using a simple comparison between the internal dynamics of the system with the healthy baseline model dynamics. The chapter assumed that the healthy baseline model dynamics are known prior to the

SHM process, which is the case for base-isolation systems, and thus developed a simpler approach to RT-SHM of such nonlinear hysteretic structures compared to Chapter 2. The designed residual signal was then used for determining the type and quantifying the severity of faults occurred using a PLLSQ fitting technique. Proof-of-concept simulation results showed that for the simulated base-isolation system and the four worst-case, abrupt fault scenarios considered, including stiffness, damping, and combined stiffness and damping faults, the SHM method developed is very capable of tracking sudden changes in stiffness and damping of the base-isolation system in real time (maximum delay ~0.8 s) using noise-free structural responses. The real-time diagnostic information provided thus offer significant potential benefit in assessing base-isolation systems' safety after a major event and can provide the information required for advanced structural control methods to compensate faults occurred and consequently maintain the overall structural system's integrity during large earthquakes.

Chapter 4 carefully examined the versatile classical Bouc-Wen model of hysteresis for the effect of each of its parameters on the overall hysteresis loop shape and consequently on the structural responses. Results for local and 'global' sensitivity analyses, considering the effect of different input excitations (20 records), different base values (3 sets), and different natural periods for the case-study structure (3 periods), were presented to assess the relative sensitivity of the overall performance of the structure to each of the parameters in the overall structural model. The results presented confirmed that some model parameters, such as the loop pinching factor (γ), have much less effect on the overall responses, and can thus be fixed at values determined by basic engineering judgements based on a limited *a priori* knowledge of the structure. This outcome enables simpler and more suitable hysteretic models with a lesser number of parameters to be identified in the RT-SHM process.

Overall, the local and 'global' sensitivity analysis results showed that the five parameters in the classical Bouc-Wen model can be ranked in order of the maximum RMS errors induced by their change on structural performance as $A \gg n > \beta > \alpha > \gamma$. These results are limited by hereditary problems using LSAs associated with the choice of base values, input excitations, and natural frequencies used, and a more thorough GSA is suggested as a future work to further study the mutual interactions of the parameters. However, the overall results provide a guideline for the use of these models in future studies.

Chapter 5 presented an on-line SHM method for nonlinear hysteretic structures using a fast and slow dynamics separation and robust PLLSQ fitting techniques. The SHM algorithm developed can directly identify changes in stiffness, damping, as well as the nonlinear hysteretic Bouc-Wen baseline model parameters, in real time, with much less *a priori* known knowledge of the structure compared to the similar RT-SHM methods developed in Chapters 2 and 3. In particular, the algorithm needs only mass (if the linear-in-parameter Bouc-Wen model is used), which is easy to estimate, to provide RT-SHM information. The method developed in this chapter is also superior to the previous SHM approaches presented in this thesis in the sense that it does not rely on difficult to measure structural displacements.

Proof-of-concept simulation results showed that for the simulated case-study structure and suite of records considered, the algorithm identifies stiffness and damping values, in real time, within 2.7% and 4.3% of the actual as-modelled values, respectively. The algorithm developed is thus robust to ground motion excitation. Moreover, simulation results for the four abrupt damage scenarios considered showed that the proposed SHM method is very capable of tracking sudden changes in the key structural parameters of hysteretic structures (stiffness, damping, and hysteretic baseline

model parameters) in real time.

Overall, the RT-SHM method presented offers significant potential benefit in assessing structural safety after a major event and is capable of providing the data required for modern structural control methods for damage mitigation purposes without any difficult to measure or identify structural dynamics. The algorithm is particularly useful for SHM of historical structures, where usually no design data is available *a priori*. The method remains to be experimentally proven and further tested, particularly against significant noise. However, it is a significant first step forward and can be readily generalized to other similar nonlinear models.

Chapter 6 empirically examined the efficacy of the line-scan displacement measurement method, originally proposed by Lim et al. (2008) for measuring foundation pile movements, for the purpose of seismic structural vibration measurement. Two significant extensions were made to this method, to enable an accurate and effective method:

- A new edge tracking algorithm was proposed for the line-scan based displacement measurement that makes the size of the camera's FOV independent from the size of the motions to be measured. This approach allows using low-cost, low-resolution line-scan cameras for high-speed, high-resolution large seismic displacement measurement. More importantly, it makes the method amenable to systems where displacements occur across a range of scales, while maintaining or improving resolution.

- A simple camera-pattern calibration procedure for the line-scan based displacement measurement was developed that guarantees fulfilment of all the basic assumptions made in the original work and thus significantly

increases the measurement results accuracy.

Comparison of input and measured motions for the case-study structure confirmed that the proposed vision-based structural displacement measurement offers a high-speed, high-resolution, and low-cost means of non-invasively measuring structural vibrations over a range of magnitudes. The line-scan displacement measurement method developed, as any other vision-based approach to structural displacement measurement, can only measure relative displacements to the camera. However, this capability is of high value in many realistic applications, such as inter-storey drift measurement.

Chapter 7 analysed the accuracy of measurement results for the line-scan based structural displacement and rotation measurement method developed in the previous chapter. Error due to imprecision in the pattern dimensions due to imprecise printing process was assessed through Monte Carlo simulation. A set of 100k randomly selected possible measurement cases for a range of pattern dimensions varying between 10 and 200 mm in width with aspect ratios ranging from 0.2 to 5 were considered in the simulation, and random values for each of the simulation parameters were uniformly distributed over the specified ranges. Simulation results showed that even errors as large as ±1% in the pattern dimensions induce only ~±1.2% error with a maximum 5th-95th inter-percentile range of ~7.4% for the linear movement measurement results. Further, results for rotation measurements remained almost unchanged with median errors close to zero with a maximum 5th-95th inter-percentile range of 1.06%.

Results of this chapter can be used to determine the acceptable range of displacement and rotation measurement results of the line-scan based method developed, particularly, where precise motion measurement is required. Thus, these results further quantify the capability of this overall approach and extend the range of its potential applications. Specifically, for the application focus of the present thesis,

seismic structural displacement measurement, the results presented confirm that typical pattern dimensions (>10 mm) and printing resolutions (>300 dpi) induce negligible amounts of error (<~±1%) in the measurement results.

CHAPTER 9

Future Work

Several areas of interest for future work have been identified as a result of this research. These areas are detailed for each chapter:

Chapter 2: LMS-based approach to RT-SHM

- The LMS-based RT-SHM method developed was predicated on the idea that noise on input responses to the algorithm can be filtered using readily-available, computationally-efficient noise-filtering methods (Ifeachor and Jervis 1993; Sayed 2003) prior to the identification and monitoring process. However, in some cases, there is no *a priori* knowledge of the noise for

noise cancellation. Hence, the effect of noise on the health monitoring results of the algorithm developed should be assessed, although, in general, LMS-based methods are robust to noise by design (Chase et al. 2005b).

- Performance of the LMS-based RT-SHM algorithm developed depends directly on the choice of the step size or filter tuning parameter (μ) used in the weight updating formula of Equation (2.29). The optimum step size value can be identified for a suite of records by minimising the error between identified and actual as-modelled health monitoring information. However, the step size identified in this way may not perform well in identifying structural parameters under different excitations than the ones tuned for. This problem can be resolved by implementing a variable step size or self-tuning LMS-based filtering algorithm initially tuned based on past earthquake records and capable of self-tuning to external load changes for the best identification results (Sayed 2003; Abadi and Far 2008; Costa and Bermudez 2008).

- A more thorough analysis of the sensitivity of the LMS-based RT-SHM approach developed to relatively small amounts of damage is required to determine the damage detection resolution of the algorithm. This analysis quantifies the level of confidence in the health monitoring information reported.

- More complex stochastic gradient estimation methods (Sayed 2003) could also be used at an additional computational cost in the LMS-based RT-SHM method developed. A detailed study of the effect of different gradient estimation techniques on the accuracy of the algorithm's results provides useful information on the optimum gradient estimation method required for a

desired level of accuracy of the output RT-SHM results.

- Evaluating the performance of the LMS-based RT-SHM algorithm developed in identification and health monitoring of non-Bouc-Wen type nonlinear hysteretic structures that initially assumed to be Bouc-Wen type is also recommended as a future avenue of research. Results of this study, if successful, would broaden the potential application space of the algorithm developed to other types of nonlinear hysteretic systems and structures.

- Finally, the overall LMS-based RT-SHM algorithm, including the two-step identification procedure, remains to be experimentally validated and further tested before implementation in the field for final performance evaluation against operational issues.

Chapter 3: RT-SHM using changes in internal dynamics

- Noise-contaminated input structural responses to the RT-SHM algorithm developed in Chapter 3 might affect sensitivity of the algorithm in both detection and diagnosis phases to small, yet important amounts of damage. Thus, further studies are required to assess how well the algorithm would perform under noisy conditions.

- Experimental validation of the fault detection and diagnosis developed is also a key step that should be taken before implementation of the algorithm in the field. To simulate sudden or gradual damping faults in a base-isolated model building with a MR damper, sudden and gradual changes in the input voltage to the damper is suggested. Stiffness faults can also be induced in the model by opening bracings or changing the thickness of columns in the model.

- Stiffness and damping faults may have equal effects on the base-isolation

174

system responses, but in opposite directions. In such situations, although there is a fault in the system, the residual signal designed remains zero. This result is expected given that the residual signal relies only on observing a change in the system responses. However, these changes may lead to larger damage and eventually failure in the system if not detected at early stages. Therefore, further research and development of the method is required to account for such exceptional cases.

Chapter 4: Parameter analysis of the Bouc-Wen model

- The results presented in this chapter provide only a sense of 'global' sensitivity of Bouc-Wen type hysteretic structures to the Bouc-Wen model parameters. A more thorough global sensitivity analysis using FAST method (Saltelli and Bolado 1998) or Sobol indices (Sobol' 1990; Sobol' 2001), considering different natural frequencies for the case-study structure and different input ground motions, would provide more reliable results, and could be followed as future research avenue.

Chapter 5: RT-SHM using a fast and slow dynamics separation technique

- Issues such as the effect of noise on input structural responses on sensitivity of the method developed to small amounts of damage, and algorithm's response speed to sudden damage to the structure should be assessed. The latter assessment would be particularly relevant if the algorithm's RT-SHM results are used as inputs to real-time structural control methods.

- Implementation of the liner-in-parameter Bouc-Wen model (Acho and Pozo 2009) in the RT-SHM method developed removes the need for estimation of the power factor prior to the SHM process and provides the opportunity of identifying all of the nonlinear hysteretic model parameters in real time. This

modification is particularly useful where there is no design data to accurately estimate the power factor, such as in historical structures.

Chapter 6 and 7: Line-scan based seismic displacement measurement

- In Figure 9.1, movements in the *XY* plane, as well as rotations about the *z* axis, can be captured using the modified line-scan displacement measurement method, described in Chapters 6 and 7, and only one line-scan camera positioned at *A*. An additional line-scan camera at position *B* could provide movements and rotations of the joint in the *YZ* plane and makes full 3D movements and rotations of the joint available. Modifying the line-scan based method developed to account for the effect of projection at an angle provides the opportunity of using only one line-scan camera for full 3D displacement and rotation measurement. As Figure 9.1 shows, only one line-scan camera could be placed at an angle to both sides of a joint (position *C*), and the camera's FOV could be divided into two parts to be processed individually based on an extended method. This novel modification makes the method even more cost-effective and enables non-invasively measuring 3D structural displacement and rotation measurement at high sampling rates and high resolutions using only one line-scan camera. However, it remains to be fully analysed and validated in future work.
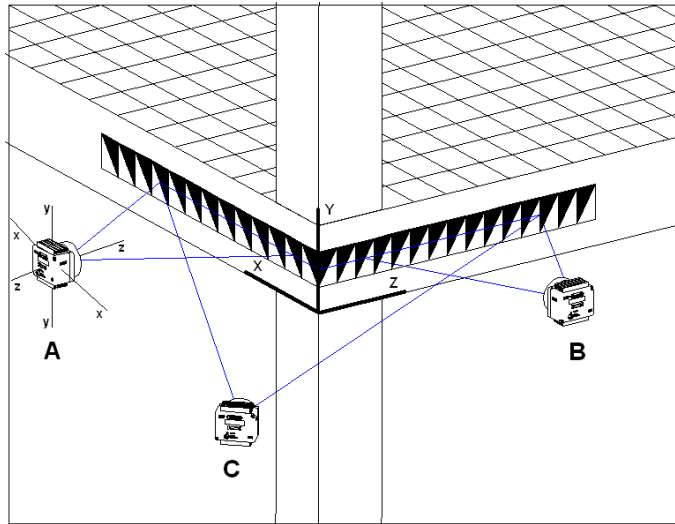
Figure 9.1. Extension of the line-scan displacement and rotation measurement method developed for full 3D displacement and rotation measurement (3D model of the camera from www.teledynedalsa.com)

REFERENCES

Abadi, M. S. E. and A. M. Far (2008). "A unified framework for adaptive filter algorithms with variable step-size." Computers & Electrical Engineering **34**(3): 232-249

Acho, L. and F. Pozo (2009). A linear-in-parameter modified Bouc-Wen model. IV ECCOMAS Thematic Conference on Smart Structures and Materials (SMART'09). Porto, Portugal**:** 8 pp.

Ahlborn, T. M., R. Shuchman, et al. (2010). The state-of-the-practice of modern structural health monitoring for bridges: a comprehensive review, Michigan Tech Research Institute.

Baber, T. and M. Noori (1986). "Modelling general hysteresis behaviour and random vibration application." Journal of Vibration, Acoustics, Stress, and Reliability in Design **108**: 411-420

Baber, T. and Y.-K. Wen (1981). "Random vibration of hysteretic, degrading systems." Journal of Engineering Mechanics Division, ASCE **107**(EM6): 1069-1087

Barroso, L. R. and R. Rodriguez (2004). "Damage detection utilizing the damage index method to a benchmark structure." Journal of Engineering Mechanics **130**(2): 142-151

Bernal, D. (2007). "Damage localization from the null space of changes in the transfer matrix." AIAA journal **45**(2): 374

Bernal, D. and B. Gunes (2000). Observer/Kalman and subspace identification of the UBC benchmark structural model. The 14th ASCE Engineering Mechanics Conference Austin, Texas.

Bernal, D. and B. Gunes (2004). "Flexibility based approach for damage characterization: Benchmark application." Journal of Engineering Mechanics **130**(Compendex): 61-70

Besançon, G. (2003). "High-gain observation with disturbance attenuation and application to robust fault detection." Automatica **39**(6): 1095-1102

Blome, C. F. (2004). LMS-based health monitoring of a non-linear rocking structure. Christchurch, University of Canterbury.

Bouc, R. (1967). Forced vibration of mechanical systems with hysteresis. The 14th Conference on Non-Linear Oscillation., Prague, Czechoslovakia.

Boyce, W. H. (1970). "Integration of accelerograms." <u>Bulletin of the Seismological Society of America</u> **60**(1): 261-263

Caicedo, J. M., S. J. Dyke, et al. (2000). <u>Health monitoring based on component transfer function.</u> The 2000 International Conference on Advances in Structural Dynamics, Hong Kong.

Caicedo, J. M., S. J. Dyke, et al. (2004). "Natural excitation technique and Eigensystem realization algorithm for phase I of the IASC-ASCE benchmark problem: Simulated data." <u>Journal of Engineering Mechanics</u> **130**(1): 49-60

Carden, E. P. and P. Fanning (2004). "Vibration Based Condition Monitoring: A Review." <u>Structural Health Monitoring</u> **3**(4): 355-377

Carr, A. J. (2004). <u>RUAUMOKO, program for inelastic dynamic analysis: user manual,</u> Department of Civil Engineering, University of Canterbury, Christchurch, New Zealand.

Chan, K., S. Tarantola, et al. (2000). Variance-Based Methods. <u>Sensitivity Analysis</u>. A. Saltelli, K. Chan and E. M. Scott. Chichester, New York, John Wiley and Sons**:** 167-197.

Chang, C. C. and Y. F. Ji (2007). "Flexible Videogrammetric Technique for Three-Dimensional Structural Vibration Measurement." <u>Journal of Engineering Mechanics</u> **133**(6): 656-664

Chase, J. G., V. Begoc, et al. (2005a). "Efficient structural health monitoring for a benchmark structure using adaptive RLS filters." <u>Computers & Structures</u> **83**(8-9): 639-647

Chase, J. G., K. L. Hwang, et al. (2005b). "A simple LMS-based approach to the structural health monitoring benchmark problem." <u>Earthquake Engineering & Structural Dynamics</u> **34**(6): 575-594

Chase, J. G., H. A. Spieth, et al. (2005c). "LMS-based structural health monitoring of a non-linear rocking structure." <u>Earthquake Engineering & Structural Dynamics</u> **34**(8): 909-930

Chassiakos, A. G., S. F. Masri, et al. (1998). "On-Line Identification of Hysteretic Systems." <u>Journal of Applied Mechanics</u> **65**(1): 194-203

Chen, C. K., R. M. Czarnecki, et al. (1977). Vibration test of a 4-story concrete structure. <u>Second ASCE Engineering Mechanics Speciality Conference</u>. Raleigh, NC**:** 2753-2758.

Choi, S. B., S. K. Lee, et al. (2001). "A hysteresis model for the field-dependent damping force of a magnetorheological damper." <u>Journal of Sound and Vibration</u> **245**(2): 375-383

Christopoulos, C., A. Filiatrault, et al. (2002). "Seismic response of self-centring hysteretic SDOF systems." <u>Earthquake Engineering & Structural Dynamics</u> **31**(5): 1131-1150

Constantinou, M. and I. Tadjbakhsh (1985). "Hysteretic dampers in base isolation: random approach." <u>Journal of Structural Engineering, ASCE</u> **111**(4): 705-721

Costa, M. H. and J. C. M. Bermudez (2008). "A noise resilient variable step-size LMS algorithm." Signal Processing **88**(3): 733-748

Demetriades, G. F., M. C. Constantinou, et al. (1993). "Study of wire rope systems for seismic protection of equipment in buildings." Engineering Structures **15**(5): 321-334

Dharap, P. V. (2006). Real-Time Structural Damage Detection Using Interaction Matrix Formulation And Observers. Department of Civil and Mechanical Engineering. Houston, Texas, Rice University. **PhD**.

Doebling, S. W., C. R. Farrar, et al. (1998). "A Summary Review of Vibration-Based Damage Identification Methods." Shock and Vibration Digest **30**(2): 91-105

Doebling, S. W., C. R. Farrar, et al. (1996). Damage identification and health monitoring of structural and mechanical systems from changes in their vibration characteristics: a literature review., Los Alamos National Laboratory **Report LA-13070-MS**.

Doherty, J. E. (1993). Non-destructive evaluation. Handbook on Experimental Mechanics. A. S. Kobayashi. New York, NY and Weinheim, Germany, VCH Publishers, Inc. and VCH Verlagsgesellschaft mbH**:** 527-555.

Dowling, N. E. (2007). Mechanical Behavior of Materials: Engineering Methods for Deformation, Fracture, and Fatigue New Jersey, Pearson Prentice Hall.

Duan, G. R. and R. J. Patton (1998). Robust fault detection in linear systems using Luenberger observers. Control '98. UKACC International Conference on (Conf. Publ. No. 455).

Dyke, S. J., J. M. Caicedo, et al. (2000). Monitoring of a benchmark structure for damage identification. The 14th ASCE Engineering Mechanics Conference, Austin, Texas.

Edwards, C., S. K. Spurgeon, et al. (2000). "Sliding mode observers for fault detection and isolation." Automatica **36**(4): 541-553

Erberik, A. and H. Sucuoglu (2004). "Seismic energy dissipation in deteriorating systems through low-cycle fatigue." Earthquake Engineering & Structural Dynamics **33**(1): 49-67

Farrar, C. R., W. E. Baker, et al. (1994). Dynamic Characterization and Damage Detection in the I-40 Bridge Over the Rio Grande, Los Alamos National Laboratory Report (LA-12767-MS).

Fishman, G. S. (1996). Monte Carlo: concepts, algorithms, and applications, Springer.

Fu, G. and A. G. Moosa (2002). "An Optical Approach to Structural Displacement Measurement and Its Application." Journal of Engineering Mechanics **128**(5): 511-520

GNS. (2011). "6.3 magnitude earthquake part of aftershock sequence - 25/02/2011." Retrieved May 24, 2011, from http://www.gns.cri.nz/Home/News-and-Events/Media-Releases/earthquake-part-of-aftershock-sequence.

Hamby, D. M. (1994). "A review of techniques for parameter sensitivity analysis of environmental models." Environmental Monitoring and Assessment **32**(2): 135-154

Hann, C. E., I. Singh-Levett, et al. (2009). "Real-Time System Identification of a Nonlinear Four-Story Steel Frame Structure-Application to Structural Health Monitoring." Sensors Journal, IEEE **9**(11): 1339-1346

Hera, A. and Z. Hou (2004). "Application of wavelet approach for ASCE structural health monitoring benchmark studies." Journal of Engineering Mechanics **130**(1): 96-104

Homma, T. and A. Saltelli (1996). "Importance measures in global sensitivity analysis of nonlinear models." Reliability Engineering & System Safety **52**(1): 1-17

Hou, Z., M. Noori, et al. (2000). "Wavelet-Based Approach for Structural Damage Detection." Journal of Engineering Mechanics **126**(7): 677-683

Hutchinson, T. C., S. R. Chaudhuri, et al. (2005). "Light-Based Motion Tracking of Equipment Subjected to Earthquake Motions." Journal of Computing in Civil Engineering **19**(3): 292-303

Hutchinson, T. C., F. Kuester, et al. (2006). "Optimal hardware and software design of an image-based system for capturing dynamic movements." Instrumentation and Measurement, IEEE Transactions on **55**(1): 164-175

Ifeachor, E. C. and B. W. Jervis (1993). Digital signal processing: A practical approach, Addison-Wesley.

Ikhouane, F., V. Mañosa, et al. (2005). "Adaptive control of a hysteretic structural system." Automatica **41**(2): 225-231

Ikhouane, F. and J. Rodellar (2007). Systems with Hysteresis: Analysis, Identification and Control using the Bouc-Wen Model, John Wiley & Sons, Ltd.

Iman, R. L. and S. C. Hora (1990). "A Robust Measure of Uncertainty Importance for Use in Fault Tree System Analysis." Risk Analysis **10**(3): 401-406

Ismail, M., F. Ikhouane, et al. (2009). "The hysteresis Bouc-Wen model, a survey." Archives of Computational Methods in Engineering **16**(2): 161-188

Ji, Y. F. and C. C. Chang (2008). "Nontarget Stereo Vision Technique for Spatiotemporal Response Measurement of Line-Like Structures." Journal of Engineering Mechanics **134**(6): 466-474

Juang, J.-N. (1985). "Eigensystem realization algorithm for modal parameter identification and model reduction." Journal of guidance, control, and dynamics **8**(5): 620-627

Kaiser, S., J. Melcher, et al. (1999). Structural dynamic health monitoring of adaptive CFRP-structures. Smart Structures and Materials 1999: Industrial and Commercial Applications of Smart Structures Technologies, 2-4 March 1999, USA, SPIE-Int. Soc.

Opt. Eng.

Kanda, K., Y. Miyamoto, et al. (2004). "Vision-based measurement for seismic damage monitoring." Journal of Japan Association for Earthquake Engineering **4**(1): 10

Kijewski-Correa, T., A. Kareem, et al. (2006). "Experimental Verification and Full-Scale Deployment of Global Positioning Systems to Monitor the Dynamic Response of Tall Buildings." Journal of Structural Engineering **132**(8): 1242-1253

Kim, H. and H. Melhem (2004). "Damage detection of structures by wavelet analysis." Engineering Structures **26**(3): 347-362

Kinnaert, M. (1999). "Robust fault detection based on observers for bilinear systems." Automatica **35**(11): 1829-1842

Lam, H. F., L. S. Katafygiotis, et al. (2004). "Application of a statistical model updating approach on phase I of the IASC-ASCE structural health monitoring benchmark study." Journal of Engineering Mechanics **130**(1): 34-48

Lee, B. (2003). "Review of the present status of optical fiber sensors." Optical Fiber Technology **9**(2): 57-79

Lee, J. J., Y. Fukuda, et al. (2007). "Development and application of a vision-based displacement measurement system for structural health monitoring of civil structures." Smart Structures and Systems **3**(3): 373-384

Li, S. J., Y. Suzuki, et al. (2004a). "Improvement of parameter estimation for non-linear hysteretic systems with slip by a fast Bayesian bootstrap filter." International Journal of Non-Linear Mechanics **39**(9): 1435-1445

Li, X., G. D. Peng, et al. (2004b). Integration of GPS, accelerometer and optical fibre sensors for structural deformation monitoring. 17th International Technical Meeting of the Satellite Division of the Institute of Navigation ION GNSS, 21-24 Sep. Long Beach, California 211-224.

Liberatore, S., J. L. Speyer, et al. (2006). "Application of a fault detection filter to structural health monitoring." Automatica **42**(7): 1199-1209

Lim, M.-S. and J. Lim (2008). "Visual measurement of pile movements for the foundation work using a high-speed line-scan camera." Pattern Recognition **41**(6): 2025-2033

Lin, C. S. (1990). "Location of modeling errors using modal test data." AIAA journal **28**(9): 1650-1654

Lin, J.-W., R. Betti, et al. (2001). "On-line identification of non-linear hysteretic structural systems using a variable trace approach." Earthquake Engineering & Structural Dynamics **30**(9): 1279-1303

Loh, C.-H., C.-Y. Lin, et al. (2000). "Time Domain Identification of Frames under Earthquake

182

Loadings." Journal of Engineering Mechanics **126**(7): 693-703

Lus, H. and R. Betti (2000). Damage identification in linear structural systems. The 14th ASCE Engineering Mechanics Conference, Austin, Texas

Lus, H., R. Betti, et al. (2004). "Investigation of a system identification methodology in the context of the ASCE benchmark problem." Journal of Engineering Mechanics **130**(1): 71-84

Lus, H., M. De Angelis, et al. (2003a). "Constructing second-order models of mechanical systems from identified state space realizations. Part I: Theoretical discussions." Journal of Engineering Mechanics **129**(5): 477-488

Lus, H., M. De Angelis, et al. (2003b). "Constructing second-order models of mechanical systems from identified state space realizations. Part II: Numerical investigations." Journal of Engineering Mechanics **129**(5): 489-501

Ma, F., C. H. Ng, et al. (2006). "On system identification and response prediction of degrading structures." Structural Control and Health Monitoring **13**(1): 347-364

Ma, F., H. Zhang, et al. (2004). "Parameter Analysis of the Differential Model of Hysteresis." Journal of Applied Mechanics **71**(3): 342-349

Martelli, A. (2009). Progress of the application of passive anti-seismic systems. Earthquake Resistant Engineering Structures VII (Proceedings of the Seventh World Conference on Earthquake Resistant Engineering Structures, Volume 104 of WIT transactions on the built environment). M. Phocas, C. A. Brebbia and P. Komodromos, Wessex Institute of Technology, UK**:** 281-293.

Masri, S. F., A. G. Chassiakos, et al. (1992). "Structure-unknown non-linear dynamic systems. Identification through neural networks." Smart Materials and Structures **1**(1): 45-45

Masri, S. F., A. W. Smyth, et al. (2000). "Application of Neural Networks for Detection of Changes in Nonlinear Systems." Journal of Engineering Mechanics **126**(7): 666-676

Mhaskar, P., C. McFall, et al. (2008). "Isolation and handling of actuator faults in nonlinear systems." Automatica **44**(1): 53-62

Michael, A. J., S. L. Ross, et al. (1999). Major Quake Likely to Strike Between 2000 and 2030, U.S. Geological Survey (USGS Fact Sheet 152-99).

Montalvao, D., N. M. M. Maia, et al. (2006). "A Review of Vibration-based Structural Health Monitoring with Special Emphasis on Composite Materials." The Shock and Vibration Digest **38**(4): 1-30

Narasimhan, S., S. Nagarajaiah, et al. (2006). "Smart base-isolated benchmark building. Part I: problem definition." Structural Control and Health Monitoring **13**(2-3): 573-588

Nastar, N., J. C. Anderson, et al. (2010). "Effects of low-cycle fatigue on a 10-storey steel

building." <u>The Structural Design of Tall and Special Buildings</u> **19**(1-2): 95-113

National Instruments Corp. (2006). NI Vision, NI PCIe-1430 User Manual: Dual-Channel, Base Configuration Camera Link Image Acquisition Device. National Instruments Corp.

Nayyerloo, M., J. G. Chase, et al. (2011). "LMS-based approach to structural health monitoring of nonlinear hysteretic structures " <u>Structural Health Monitoring</u> **10**(4): 429-444

Nayyerloo, M., A. Malherbe, et al. (2010). <u>Seismic structural displacement measurement using a high-speed line-scan camera: experimental validation</u>. The 2010 New Zealand Society of Earthquake Engineering Conference and AGM, Wellington, New Zealand.

Ni, Y. Q., J. M. Ko, et al. (1998). "Identification of non-linear hysteretic isolators from periodic vibration tests." <u>Journal of Sound and Vibration</u> **217**(4): 737-756

NZ Government. (2011). "Briefing on Costs: Earthquake Recovery " Retrieved May 24, 2011, from http://beehive.govt.nz/feature/briefing-costs-earthquake-recovery.

NZ Parliament. (2011). "Earthquake, Canterbury—Cost of Damage." Retrieved Jan 7, 2011, from http://www.parliament.nz/en-NZ/PB/Business/QOA/f/5/2/49HansQ_20100909_00000002-2-Earthquake-Canterbury-Cost-of-Damage.htm.

NZ Police. (2011). "List of deceased (as a result of the Christchurch earthquake)." Retrieved May 24, 2011, from http://www.police.govt.nz/list-deceased.

NZS 3101 (2006). "NZS 3101, Concrete Structures Standard, New Zealand."

Orteu, J.-J. (2009). "3-D computer vision in experimental mechanics." <u>Optics and Lasers in Engineering</u> **47**(3-4): 282-291

Page, R. A., P. H. Stauffer, et al. (1999). Progress Toward a Safer Future Since the 1989 Loma Prieta Earthquake, U.S. Geological Survey (USGS Fact Sheet 151-99).

Patton, R. J. (1997). "Robustness in model-based fault diagnosis: The 1995 situation." <u>Annual Reviews in Control</u> **21**: 103-123

Philips Corp. (2011). MASTERLine 111 60W G53 12V 8D 1CT: Low-voltage halogen reflector lamp with double-ended burner and high-purity aluminium reflector. Koninklijke Philips Electronics N.V.

Rodríguez, A., N. Iwata, et al. (2009). "Model identification of a large-scale magnetorheological fluid damper." <u>Smart Materials and Structures</u> **18**(1): 015010

Saif, M. (2002). <u>Fault diagnosis based on equivalent control concept</u>. Automation Congress, 2002 Proceedings of the 5th Biannual World.

Saito, T. (2007). "Basic concept of base isolation system for buildings." <u>Lectures on Seismic</u>

Isolation Systems in Japan at the headquarters of the IStructE (The Institution of Structural Engineers) in London Retrieved August 1, 2011, from http://www.cibw114.net/report/Japan02.pdf.

Saltelli, A. and R. Bolado (1998). "An alternative way to compute Fourier amplitude sensitivity test (FAST)." Computational Statistics & Data Analysis **26**(4): 445-460

Sato, T. and K. Qi (1998). "Adaptive H_∞ Filter: Its Application to Structural Identification." Journal of Engineering Mechanics **124**(11): 1233-1240

Sato, T. and K. Takei (1997). Real time robust identification algorithm for structural systems with time-varying dynamic characteristics. Proceedings of SPIE: Smart Structures and Materials, Mathematics and Control in Smart Structures San Diego, CA, USA.

Sayed, A. H. (2003). Fundamentals of Adaptive Filtering, John Wiley & Sons, Inc.

Schneider Kreuznach Corp. (2010). Macro system. Jos. Schneider Optische Werke GmbH.

Sedgewick, R. (1997). Algorithms in C: Parts 1-4. Fundamentals, data structures, sorting, searching, Addison-Wesley.

Shen, Y., M. F. Golnaraghi, et al. (2005). "Analytical and Experimental Study of the Response of a Suspension System with a Magnetorheological Damper." Journal of Intelligent Material Systems and Structures **16**(2): 135-147

Smyth, A. W., S. F. Masri, et al. (1999). "On-Line Parametric Identification of MDOF Nonlinear Hysteretic Systems." Journal of Engineering Mechanics **125**(2): 133-142

Sobol', I. M. (1990). "Sensitivity estimates for nonlinear mathematical models." Matematicheskoe Modelirovanie **2** (1): 112-118 (in Russian).English translation in: Sobol' I. M. (1993), Mathematical Modeling and Computational Experiment: 1(4), 407-414.

Sobol', I. M. (2001). "Global sensitivity indices for nonlinear mathematical models and their Monte Carlo estimates." Mathematics and Computers in Simulation **55**(1-3): 271-280

Sohn, H., C. R. Farrar, et al. (2004). A Review of Structural Health Monitoring Literature: 1996-2001, Los Alamos National Laboratory.

Spencer, J. B. F., S. J. Dyke, et al. (1997). "Phenomenological Model for Magnetorheological Dampers." Journal of Engineering Mechanics **123**(3): 230-238

Spencer, J. B. F. and S. Nagarajaiah (2003). "State of the Art of Structural Control." Journal of Structural Engineering **129**(7): 845-856

Stiros, S. C. (2008). "Errors in velocities and displacements deduced from accelerographs: An approach based on the theory of error propagation." Soil Dynamics and Earthquake Engineering **28**(5): 415-420

Sucuoglu, H. and A. Erberik (2004). "Energy-based hysteresis and damage models for deteriorating systems." Earthquake Engineering & Structural Dynamics **33**(1): 69-88

Sun, Z. and C. C. Chang (2004). "Statistical Wavelet-Based Method for Structural Health Monitoring." Journal of Structural Engineering **130**(7): 1055-1062

Teledyne DALSA Corp. (2008a). Piranha 2 P2-2x-xxx40 Camera User's Manual. T. DALSA, Teledyne DALSA.

Teledyne DALSA Corp. (2008b). Piranha 2 P2-2X-XXX40 Line Scan Cameras-Datasheet, Teledyne DALSA Corporation.

Teledyne DALSA Corp. (2011). Piranha 3 P3-8X-XXX40 Line Scan Cameras-Datasheet, Teledyne DALSA Corporation.

Teran-Gilmore, A. and J. O. Jirsa (2007). "Energy demands for seismic design against low-cycle fatigue." Earthquake Engineering & Structural Dynamics **36**(3): 383-404

The World Bank (2011). Developing Trends: March 2011, Focus: Effects of the 2011 Japan earthquake, The World Bank**:** 13-16.

Trifunac, M. D. (1971). "Zero baseline correction of strong-motion accelerograms." Bulletin of the Seismological Society of America **61**(5): 1201-1211

Trujillo, D. M. and A. L. Carter (1982). "A new approach to the integration of accelerometer data." Earthquake Engineering & Structural Dynamics **10**: 529-535

Tsouroukdissian, A. R., F. Ikhouane, et al. (2009). "Modeling and Identification of a Small-scale Magnetorheological Damper." Journal of Intelligent Material Systems and Structures **20**(7): 825-835

USGS. (2011). "Largest and Deadliest Earthquakes by Year." Retrieved Jan 07, 2011, from http://earthquake.usgs.gov/earthquakes/eqarchives/year/byyear.php.

Vayas, I., A. Sophocleous, et al. (2003). "Fatigue analysis of moment resisting steel frames." Journal of Earthquake Engineering **7**(4): 635 - 654

Vidal, Y., L. Acho, et al. (2010). Fault detection in base-isolation systems via a restoring force observer. 2010 Conference on Control and Fault Tolerant Systems. Nice, France, IEEE**:** 777-782.

Villamor, P. and the Science Response teams (2010). The M 7.1, 4 September Darfield (Canterbury) Earthquake and Impacts: A Research Overview, GNS Science.

Wen, Y.-K. (1976). "Method for random vibration of hysteretic systems." Journal of Engineering Mechanics Division, ASCE **102**(2): 249-263

Worden, K. and W. Becker (2011). On the Identification of Hysteretic Systems, Part II:

Bayesian Sensitivity Analysis. <u>Nonlinear Modeling and Applications, Volume 2</u>. T. Proulx, Springer New York. **11:** 77-91.

Xiaomin, X., S. Qing, et al. (2009). "Parameter Estimation and its Sensitivity Analysis of the MR Damper Hysteresis Model Using a Modified Genetic Algorithm." <u>Journal of Intelligent Material Systems and Structures</u> **20**(17): 2089-2100

Yang, J., J. B. Li, et al. (2006). "A simple approach to integration of acceleration data for dynamic soil-structure interaction analysis." <u>Soil Dynamics and Earthquake Engineering</u> **26**(8): 725-734

Yang, J. N., Y. Lei, et al. (2004). "Hilbert-Huang based approach for structural damage detection." <u>Journal of Engineering Mechanics</u> **130**(1): 85-95

Yang, J. N. and S. Lin (2004). "On-line identification of non-linear hysteretic structures using an adaptive tracking technique." <u>International Journal of Non-Linear Mechanics</u> **39**(9): 1481-1491

Yoshida, I. (2001). Damage detection using Monte Carlo filter based on non-Gaussian noise. <u>The 8th International Conference on Structural Safety and Reliability: ICOSSAR '01</u>. Newport Beach, CA, USA, A. A. Balkema a member of Swets & Zeitlinger Publishers, Lisse, The Netherlands**:** 324 -331.

Yuen, K.-V., S. K. Au, et al. (2004). "Two-stage structural health monitoring approach for phase I benchmark studies." <u>Journal of Engineering Mechanics</u> **130**(1): 16-33

Zang, C., M. I. Friswell, et al. (2004). "Structural Damage Detection using Independent Component Analysis." <u>Structural Health Monitoring</u> **3**(1): 69-83

Zapico, J. L. and et al. (2001). "Vibration-based damage assessment in steel frames using neural networks." <u>Smart Materials and Structures</u> **10**(3): 553

Zhang, H., G. C. Foliente, et al. (2002). "Parameter identification of inelastic structures under dynamic loads." <u>Earthquake Engineering & Structural Dynamics</u> **31**(5): 1113-1130